JAMES | Journal of Advances in Modeling Earth Systems

RESEARCH ARTICLE
10.1029/2023MS003701

How Can We Improve the Seamless Representation of Climatological Statistics and Weather Toward Reliable Global K-Scale Climate Simulations?

Daisuke Takasuka[1,2], Chihiro Kodama[2], Tamaki Suematsu[3], Tomoki Ohno[1], Yohei Yamada[2], Tatsuya Seiki[2], Hisashi Yashiro[4], Masuo Nakano[2], Hiroaki Miura[5], Akira T. Noda[2], Tomoe Nasuno[2], Tomoki Miyakawa[1], and Ryusuke Masunaga[2]

[1]Atmosphere and Ocean Research Institute, The University of Tokyo, Kashiwa, Japan, [2]Japan Agency for Marine-Earth Science and Technology, Yokohama, Japan, [3]RIKEN Center for Computational Science, Kobe, Japan, [4]National Institute for Environmental Studies, Tsukuba, Japan, [5]Department of Earth and Planetary Science, The University of Tokyo, Tokyo, Japan

Abstract Toward the achievement of reliable global kilometer-scale (k-scale) climate simulations, we improve the Nonhydrostatic ICosahedral Atmospheric Model (NICAM) by focusing on moist physical processes. A goal of the model improvement is to establish a configuration that can simulate realistic fields seamlessly from the daily-scale variability to the climatological statistics. Referring to the two representative configurations of the present NICAM, each of which has been used for climate-scale and sub-seasonal-scale experiments, we try to find the appropriate partitioning of fast/local and slow/global-scale circulations. In a series of sensitivity experiments at 14-km horizontal resolution, we test (a) the tuning of terminal velocities of rain, snow, and cloud ice, (b) the implementation of turbulent diffusion by the Leonard term, and (c) enhanced vertical resolution. These tests yield reasonable convection triggering and convection-induced tropospheric moistening, and result in better performance than in previous NICAM climate simulations. In the mean state, double Intertropical Convergence Zone bias disappears, and the zonal contrast of equatorial precipitation, top-of-atmosphere radiation balance, vertical temperature profile, and position/strength of subtropical jet are reproduced dramatically better. Variability such as equatorial waves and the Madden–Julian oscillation (MJO) is spontaneously realized with appropriate spectral power balance, and the Asian summer monsoon, boreal-summer MJO, and tropical cyclone (TC) activities are more realistically simulated especially around the western Pacific. Meanwhile, biases still exist in the representation of low-cloud fraction, TC intensity, and precipitation diurnal cycle, suggesting that both higher spatial resolutions and further model development are warranted.

Plain Language Summary In the near future, increasing computational power will make it possible to perform a global kilometer-scale "cloud-resolving" model (GCRM) simulation on the climate time scale, which is expected to reduce the uncertainty of cloud-related processes in the climate system. In this sense, it is important to make GCRMs more reliable tools in the evaluation and prediction of the variabilities over a wide range of spatio-temporal scales. With this perspective, we improve a Japanese GCRM, the Nonhydrostatic Atmospheric Icosahedral Model (NICAM), to achieve the realistic representation of both weather phenomena and climatological features in long-term simulations. We revise the NICAM by the reconsideration of cloud microphysics properties, the implementation of diffusion processes around strong convection cores, and increased vertical layers. These revisions lead to the substantial improvements in the climatological mean precipitation distributions, radiative energy balance at the top of the atmosphere, westerly jets in the mid-latitude, and temperature fields. We also find that weather phenomena such as the Asian summer monsoon and tropical cyclone (TC) genesis are simulated more realistically. We expect that, in addition to the above model improvements, kilometer-scale horizontal resolutions can resolve a part of remaining issues of the representation of TC intensity and precipitation diurnal cycle.

Key Points:

- We improve a global nonhydrostatic atmospheric model focusing on resolution-independent errors that can exist even in k-scale climate runs
- Key improvements are retuning of cloud microphysics properties, consideration of grid-scale turbulent mixing, and increased vertical layers
- Biases in mean rainfall, radiation balance, and circulation as well as weather (monsoon, Madden–Julian oscillation, equatorial wave, tropical cyclone) are reduced

Correspondence to:
D. Takasuka,
takasuka@aori.u-tokyo.ac.jp

Citation:
Takasuka, D., Kodama, C., Suematsu, T., Ohno, T., Yamada, Y., Seiki, T., et al. (2024). How can we improve the seamless representation of climatological statistics and weather toward reliable global K-scale climate simulations? *Journal of Advances in Modeling Earth Systems*, *16*, e2023MS003701. https://doi.org/10.1029/2023MS003701

Received 5 MAR 2023
Accepted 22 DEC 2023

1. Introduction

In Earth's atmosphere, deep convection is a fundamental element of phenomena over a wide range of spatio-temporal scales. While individual deep convective clouds have a $O(1)$-km spatial scale and a short lifetime (within a few hours), they play a significant role in redistributing heat, water, and momentum and in exciting atmospheric waves. They are thus tightly coupled with the global atmospheric circulation driven by latent and

radiative heating and by momentum transportation. Also, deep convection is often organized at $O(10^2 - 10^3)$-km scales, as observed as mesoscale convective systems (MCSs) (Houze, 1993), tropical cyclones (TCs), convectively coupled equatorial waves (Kiladis et al., 2009; Takayabu, 1994), and the Madden–Julian oscillation (MJO) (Madden & Julian, 1971), all of which greatly modulate both local and global weather patterns. Hence, better treatment of deep convection in climate models is expected to achieve the seamless representation of both the climatological mean states and variabilities.

Simulating deep convection globally and explicitly without any convective parameterizations is one of the strategies for improving the accuracy of global climate models (GCMs) (Bony et al., 2015; Satoh et al., 2019; Slingo et al., 2022; Tomita et al., 2005). Such "global convection-resolving model (GCRM) simulations" have become possible at kilometer-scale (k-scale) resolutions thanks to the recent increase in computing power, and they have succeeded in reproducing weather variability especially at the sub-seasonal to seasonal (S2S) scale (e.g., Miura, Satoh, Nasuno, et al., 2007; Miyakawa et al., 2014; Stevens et al., 2019). In pioneering work, Miura, Satoh, Nasuno, et al. (2007) used the Nonhydrostatic Icosahedral Atmospheric Model (NICAM) (Satoh et al., 2008; Tomita & Satoh, 2004) with 3.5-km and 7-km resolutions to realistically simulate the eastward migration of MJO convection for about a month and the MJO-related TC genesis. In addition, Stevens et al. (2019) recently compared 40-day simulations by nine global models at less than 5-km grid spacing and showed that k-scale models can reasonably represent the large-scale circulation and TC activities at least at the sub-seasonal scale.

Beyond the *S2S* scale, a $O(10)$-year global *climate* simulation with explicit treatment of deep convection (i.e., GCRM-mode climate simulation) is an important milestone in climate modeling (e.g., Kinter et al., 2013). It has already been performed by Kodama et al. (2015, 2021), although they adopted 14-km grid spacing, at which individual cumulus systems cannot be fully resolved. In CMIP6 HighResMIP simulations by NICAM (Kodama et al., 2021), the mean radiation distributions, which are important to the climate, can be optimized especially by refining the cloud microphysics and radiation schemes. This success is attributed to the better representation of the amount of cloud ice and high clouds originating from explicit deep convection. In addition, GCRM-mode climate simulations may help reduce the uncertainties in the statistics of TCs (Yamada et al., 2017) and cloud amounts (Chen et al., 2022) in various climate regimes.

Although GCRM-mode climate simulations are expected to be able to reproduce both realistic climatological statistics and individual weather disturbances (e.g., MJO, TCs) seamlessly, this has not yet been achieved, at least in 14-km mesh NICAM climate simulations. For example, the amplitude of the simulated MJO is much weaker than the observations (Kikuchi et al., 2017; Suematsu et al., 2022), and the simulated MJO tends to fail to propagate into the western Pacific (Kodama et al., 2015), which is an exaggerated "barrier effect" of the Maritime Continent as seen in many other conventional GCMs (e.g., Ling et al., 2019). In addition, some TC tracks are unrealistically represented, in that TCs generated over the eastern Pacific tend to cross the dateline (Kodama et al., 2015). The climatological mean states also have some long-standing biases, such as the double intertropical convergence zone (ITCZ) and smaller low-cloud amount, especially in NICAM HighResMIP simulations (Kodama et al., 2021).

One may expect that k-scale resolutions can solve the aforementioned issues in coarser-resolution climate simulations, and several studies have shown aspects of this to be partly true: a tendency for deep convective characteristics to converge at 870-m resolution (Miyamoto et al., 2013), a realistic large-scale circulation in a 4-month 1.4-km resolution simulation (Wedi et al., 2020), and the subtropical low-cloud amount close to the observation at 2.5-km resolution (Hohenegger et al., 2020). Wedi et al. (2020) also reported, however, that the model biases in the MJO or tropical precipitation are not reduced even at 1.4-km resolution. This situation holds true for NICAM, as indicated by the 40-day (from 1 June 2004) mean precipitation for the observation (Figure 1a) and 14- and 3.5-km simulations under the HighResMIP configuration (Figures 1b and 1c). The biases of the excess of precipitation are common at both resolutions over the ITCZ and Indian Ocean. In addition, meridional splitting of the precipitation band around the dateline (i.e., double ITCZ structure reported in Kodama et al. (2021)) and the shortage of precipitation over the western Pacific remain or are emphasized in the 3.5-km simulation.

Such resolution-independent errors (at least within $O(1–10)$-km resolutions) in the representation of large-scale weather disturbances and climate patterns suggest the importance of better understanding and improving mesoscale (∼100 km) and corresponding temporal-scale moist physics even in, or rather because of, the GCRM framework at k-scale resolutions. GCRMs aim to directly solve local responses (e.g., precipitation, mesoscale

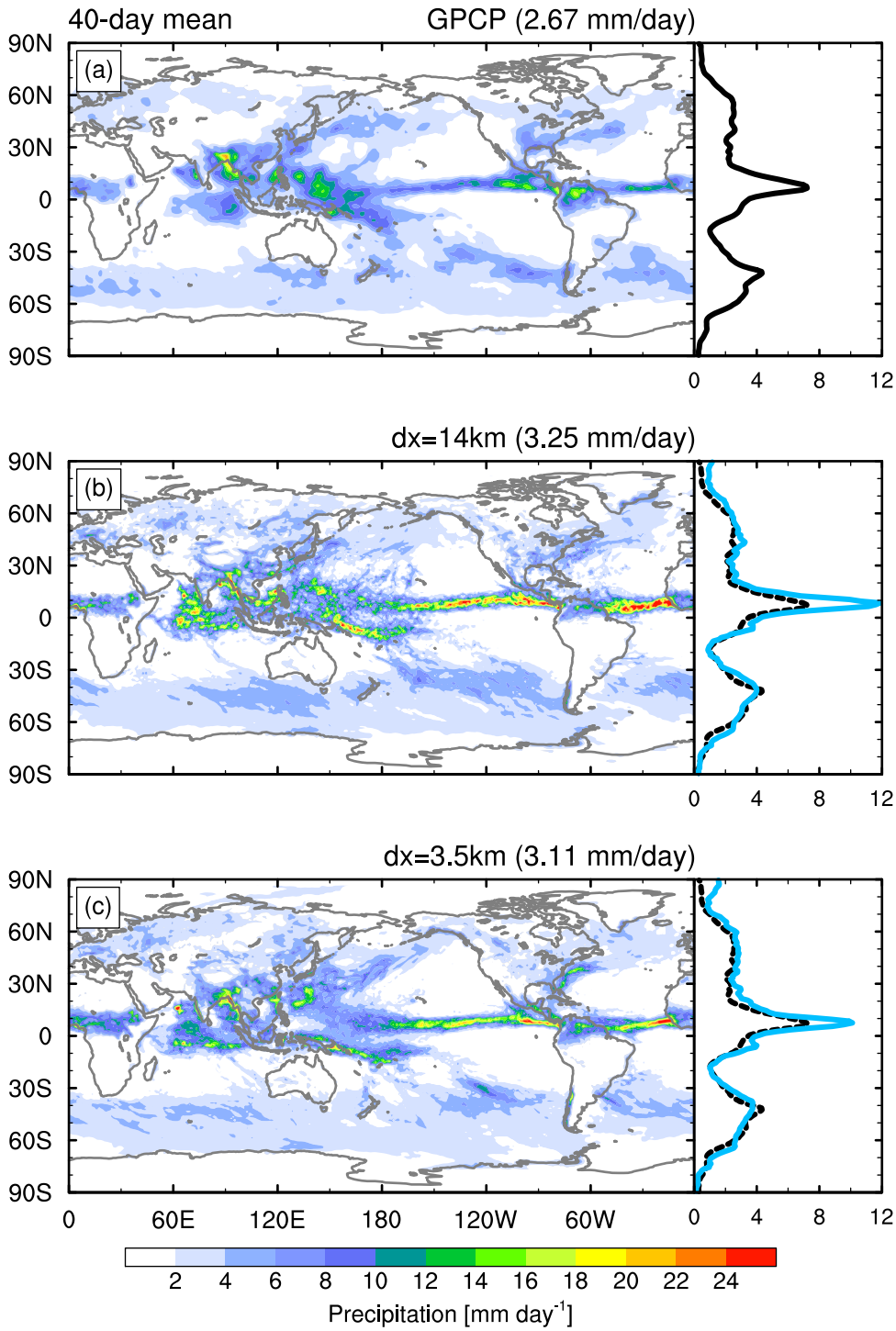

Figure 1. (a–c) Horizontal maps of the 40-day (from 1 June 2004) mean precipitation for the (a) Global Precipitation Climatology Project (GPCP) product and (b) 14-km and (c) 3.5-km mesh simulations under the HighResMIP setting. Zonal mean distributions are also plotted in right panels, and in (b and c), the simulations (blue) and GPCP (black dashed) are compared. Global mean values are denoted at the upper-right corner of figures.

circulations) to the moisture and cloud evolution and to obtain larger-scale patterns by accumulating those local responses. However, a model at O(1–10)-km resolutions still has scale-independent uncertainties in physics–dynamics coupling. In that sense, large-scale fields simulated by GCRMs at k-scale resolutions can depend

heavily on local model physics, as implied by Miura (2019), although this problem might be resolved if resolutions were fine enough to capture cloud eddies. In this situation, it is non-trivial whether the accumulation of local responses leads to the accurate simulation of equilibrium states such as the climate, because a model physics may not have enough degrees of freedom to satisfy two key aspects: (a) better representation of individual large-scale convective variations for realistic weather, and (b) better energy balance for realistic equilibrium states. In fact, one NICAM configuration that works well for *S2S*-scale simulations (e.g., good MJO hindcasts) does not provide a realistic equilibrium of the radiative energy budget at *climate* scales, so another configuration that improves climatological mean radiative fields has been established (Kodama et al., 2021). Note that the S2S-scale-mean state trade-off has also been reported and discussed in the context of tuning of the local convective sensitivity to tropospheric moisture in conventional GCMs (e.g., Hannah & Maloney, 2011, 2014; Kim et al., 2009, 2011).

In convection-resolving simulations, where cloud formation is directly coupled to local dynamics, the moisture–convection–radiation relationship and its impact on the large-scale circulations are controlled by explicit cloud microphysics and turbulent diffusion, as well as by model resolutions. In fact, Miura (2019) showed that the MJO reproducibility in GCRMs is sensitive to cloud microphysics parameters, such as the velocity of falling rain and snow, that can affect the vertical profile of moisture and clouds. The impacts of microphysics are also confirmed in the TC development (Nasuno et al., 2016) and diurnal convection over the Maritime Continent (Nasuno, 2021). In addition, the choice and parameter settings of turbulent schemes can influence the favored spatio-temporal scale of convective organization by changing the efficiency of the subgrid-scale horizontal/upward moisture transport (Holloway et al., 2013; Miura, Satoh, Tomita, et al., 2007). Furthermore, vertical resolutions have a large impact on the amount of tropical high clouds (Ohno et al., 2019; Seiki et al., 2015), which truly governs the mean radiation balance.

Given that parameter tuning and better treatment of unresolvable physics in GCRMs can determine model performance over various temporal scales and that mesoscales seem to have significant impacts on synoptic-to-large-scale behaviors, it is essential to consider the model physics required for reproducing both realistic climatological statistics and weather before entering the k-scale world. Thus, in the present study, using a series of 1-year sensitivity experiments with a 14-km horizontal mesh, which effectively resolves structures at scales of more than 100 km, we aim to obtain a model that can seamlessly and realistically reproduce atmospheric variabilities and equilibrium states ranging from the precipitation diurnal cycle to the global circulation. Specifically, we reconsider the cloud microphysics, turbulent diffusion, and vertical resolution, and examine their impacts on the moisture–convection relationship. Then, we provide a model configuration that can achieve the best possible representation of wide spatio-temporal-scale fields, in anticipation of a reliable k-scale climate simulation.

This paper is organized as follows. Section 2 describes the model, the experimental design of sensitivity experiments toward model improvement, and the observational data sets for model evaluation. Section 3 provides a comparison of the moisture transport via deep convection, the 1-year mean states, and the disturbances in two representative settings, one of which emphasizes the better radiation distributions in *climate*-scale simulations and the other the better MJO representation in *S2S*-scale simulations. Based on this comparison, we introduce the major model updates and their impacts on the moisture–convection relationship and convective organization in Section 4. Section 5 presents a comprehensive examination of the impacts of the model updates on the mean precipitation, radiation, and large-scale circulations and disturbances such as the MJO, equatorial waves, TCs, and precipitation diurnal cycle. In Section 6, we discuss a possible reason for the mitigation of double ITCZ and weak MJO biases, which are representatives of long-standing problems in NICAM climate simulations. A summary and concluding remarks are given in Section 7.

2. Model, Experimental Design, and Observational Data Sets

2.1. Model

NICAM is based on a fully compressible nonhydrostatic dynamical core (Satoh et al., 2008; Tomita & Satoh, 2004) and is horizontally discretized by an icosahedral Arakawa A-grid system modified with spring dynamics on the sphere (Tomita et al., 2002). Notably, the conservation of the total energy, which is important in climate simulations, is guaranteed by the conservative scheme with moist processes (Satoh, 2002, 2003). In this scheme, the total energy is predicted in its flux form to conserve it strictly, and the internal moist energy is

obtained by subtracting the known kinetic energy and potential energy. Thus, the atmospheric energy leakage other than the top-of-atmosphere radiative imbalance is not an issue in NICAM.

The version of NICAM used in this study is similar to that used in Kodama et al. (2021), but with some modifications. We adopted a globally quasi-uniform 14-km horizontal mesh despite the fact that this resolution is far from a convection-resolving scale. This is based on the idea that, as mentioned in the Introduction, some biases found in previous 14-km mesh NICAM climate simulations (Kodama et al., 2015, 2021) can be resolution-independent (cf., Figure 1), and addressed by the model physics improvement that is commonly effective at $O(1-10)$-km grid spacing. From a practical perspective, the computational costs are still too high to conduct many sensitivity experiments at k-scale resolutions in order to test the impacts of changes in the model physics. As for vertical resolution, two different numbers of vertical layers are used: 38 (Kodama et al., 2015) and 78 (Ohno & Satoh, 2018) with a model top height of about 40 and 50 km, respectively. The model time step is basically set to 60 and 30 s for the experiments with 38 and 78 vertical layers, respectively. Note that this time step is sometimes temporarily shortened to avoid numerical instability.

The physics schemes are almost the same as in Kodama et al. (2021), except for the turbulent diffusion effect that is newly implemented in the present study (see the next subsection). Subgrid-scale turbulent mixing is represented by the Mellor-Yamada-Nakanishi-Niino level 2 (MYNN2) scheme (Nakanishi & Niino, 2006; Noda et al., 2010). As suggested by Ohno et al. (2020), the saturation adjustment treatment of subgrid-scale ice clouds in MYNN2 is turned off. The radiative transfer is calculated by Model Simulation radiation TRaNsfer code (MSTRN) X (Sekiguchi & Nakajima, 2008) with 29 radiation bands. The land surface processes are treated with the Minimal Advanced Treatments of Surface Interaction and RunOff (MATSIRO) model (Takata et al., 2003). Ocean surface heat and momentum fluxes are computed by the Louis (1979)'s bulk formula with a modified roughness length for strong wind conditions (Fairall et al., 2003; Moon et al., 2007). The orographic gravity wave drag scheme (McFarlane, 1987) is used to represent momentum transport carried by vertically propagating subgrid-scale orographic gravity waves.

Instead of cumulus parameterization and large-scale condensation schemes, two types of single-moment bulk cloud microphysics schemes are used; which type we use depends on the sensitivity experiments. One is an original version of NICAM Single-Moment Water 6 (NSW6) developed by Tomita (2008) (denoted as the T08 version), and the other is an updated version of T08 based on comparisons with satellite observations (Roh et al., 2017; Roh & Satoh, 2014) (denoted as the RS14 version). Compared to the T08 version, the RS14 version assumes lighter precipitation from graupel and snow, and it forms more cloud ice via the explicit ice nucleation and vapor deposition processes replacing saturation adjustment (see Table 5 in Kodama et al. (2021) for the key differences). Both cloud microphysics schemes are consistently coupled with the radiation scheme that considers the nonsphericity of ice particles (Seiki et al., 2014).

2.2. Design of Sensitivity Experiments

To achieve the seamless representation of both climatological mean states and weather disturbances, we take two representative settings in NICAM as a starting point in designing the sensitivity experiments. One is the HighResMIP-tuned setting (Kodama et al., 2021), which prioritizes the improved radiation distributions in the *climate* simulations; and the other is the MJO-tuned setting (e.g., Miura et al., 2015; Miyakawa et al., 2014; Suematsu et al., 2021), which prioritizes the realistic MJO reproduction in the *S2S*-scale simulations. Because these two settings are specialized for the reproducibility of climate- or weather-scale fields, they are expected to be helpful references for obtaining a model that is a good mix of both. The experiments that adopt the HighResMIP- and MJO-tuned settings are hereafter referred to as the HRMIP and MJO runs, respectively.

The difference between the HRMIP and MJO runs is in cloud microphysics. The two settings adopt different versions of the microphysics scheme: the HRMIP run uses RS14, while the MJO run uses T08. In addition, a decisive difference is that the terminal velocities of rain and snow are set to much smaller values in the MJO run than in the HRMIP run. As shown in Table 1, the MJO run applies the smaller coefficients $c_{[r,s]}$ in the terminal velocities $v_{t[r,s]}$,

$$v_{t[r,s]} = c_{[r,s]} D^{d_{[r,s]}} \times f(\rho, \rho_0) \tag{1}$$

Table 1
List of Sensitivity Experiments and Their Settings for Cloud Microphysics (Second to Fourth Columns), Turbulent Diffusion by Leonard/Cross Terms (Fifth Column), and Vertical Layers (Sixth Column)

	Microphysics				
Run name	(Version)	(c_r, c_s)	(Cloud ice falling speeds)	Leonard term	Vertical layers
HRMIP	RS14	(130.0, 4.84)	N/A	N/A	38
MJO	T08	(55.0, 0.80)	N/A	N/A	38
MP	RS14	(90.0, 2.00)	10 cm s^{-1}	N/A	38
LEO1	RS14	(130.0, 4.84)	N/A	$K_f = 1.0$	38
LEO2	RS14	(130.0, 4.84)	N/A	$K_f = 2.0$	38
MP-LEO1	RS14	(90.0, 2.00)	10 cm s^{-1}	$K_f = 1.0$	38
MP-LEO2	RS14	(90.0, 2.00)	10 cm s^{-1}	$K_f = 2.0$	38
MP-LEO2-L78	RS14	(90.0, 2.00)	10 cm s^{-1}	$K_f = 2.0$	78

where subscripts r and s denote rain and snow, respectively; D is the particle diameter; d is the empirical coefficient depending on the particle shape (here $d_r = 0.5$, $d_s = 0.25$); and $f(\rho, \rho_0)$ represents a function of the density and the density at ground level. This difference has a large influence on how moisture is accumulated and consumed before and after deep convection triggering, as discussed in Section 3.1.

How reasonable is a tuned $c_{[r,s]}$ in terms of actual cloud microphysics properties? This question is validated by the relationship between $c_{[r,s]}$ and the diameters of rain and snow that are weighted in their growth and falling (e.g., Gunn & Kinzer, 1949; Rogers et al., 1993). For example, the HRMIP run ($c_r = 130.0$, $c_s = 4.84$) assumes fitting suitable for $D_r \sim 1$ mm and $D_s \sim 500$ μm. Considering that D_r is typically 0.5–2 mm in deep convection (Huang & Chen, 2019) and that D_s is estimated as 100–200 μm (Seiki & Ohno, 2023), the HRMIP run expects reasonable raindrop size and much larger snow than the realistic estimation. Meanwhile, the MJO run focuses on $D_r \sim 200$ μm and $D_s \sim 60$ μm in $v_{t[r,s]}$ fitting, indicating that slow terminal velocities of rain and snow are realized by underestimating their assumed sizes.

A comparison of the HRMIP and MJO runs motivates us to revise the microphysics settings, and we conduct an experiment with this revision (MP run; see Table 1). In the RS14 version of the MP run, the terminal velocities of rain and snow are retuned (i.e., retuning of $c_{[r,s]}$), and cloud ice falling at 10 cm s^{-1} (typical value for cloud ice of particle diameter less than 100 μm; see Figure 1 in Seiki and Ohno (2023)) is introduced. The basis of the microphysics retuning in terms of the moisture–convection relationship and its impacts are described in Section 4.1. Note that retuned $c_{[r,s]}$ correspond to $v_{t[r,s]}$ fitting around $D_r \sim 500$ μm and $D_s \sim 120$ μm, so that they are reasonable even from the perspective of actual microphysics properties.

In another series of sensitivity experiments, we examine the impacts of the turbulent diffusion by eddies with model-grid scales. This effect is newly implemented into NICAM in the present study, because Moeng et al. (2010) suggests that the conventional subgrid-scale turbulence schemes alone cannot represent all the turbulent fluxes in simulations at grid spacings that are typical of GCRMs (about 10 km and less). Following Germano (1986), we consider the scalar turbulent fluxes at model unresolvable scales (τ_{vc}):

$$\begin{aligned}\tau_{vc} &= \widetilde{vc} - \tilde{v}\tilde{c} \\ &= \left(\widetilde{\tilde{v}\tilde{c}} - \tilde{\tilde{v}}\tilde{\tilde{c}}\right) + \left(\widetilde{\tilde{v}c'} + \widetilde{v'\tilde{c}} - \widetilde{\tilde{v}c'} - \widetilde{v'\tilde{c}}\right) + \left(\widetilde{v'c'} - \widetilde{v'}\widetilde{c'}\right)\end{aligned} \tag{2}$$

where v is horizontal or vertical wind velocity; c is any scalars; and $\tilde{x}$ and x' denote any quantities x filtered for model-grid scales and the deviations from them (i.e., $x - \tilde{x}$), respectively. In Equation 2, the turbulent diffusion that we additionally treat corresponds to the first and second terms, called the Leonard term (Germano, 1986; Leonard, 1975) and cross term, respectively. Regarding physics, the Leonard term represents turbulent mixing by grid-scale to effectively resolvable-scale eddies, and the cross term represents the interactive mixing between grid-scale and subgrid-scale eddies. Referring to the derivation in Moeng et al. (2010), we implement the scalar vertical and horizontal turbulent fluxes from these two terms as follows:

$$\tau^*_{wc} = K_f\left(\frac{\Delta^2}{12}\right)\nabla_h\tilde{w}\cdot\nabla_h\tilde{c} \tag{3}$$

$$\tau^*_{v_hc} = K_f\left(\frac{\Delta^2}{12}\right)\nabla_h\tilde{v_h}\cdot\nabla_h\tilde{c} \tag{4}$$

where Δ is the horizontal grid spacing; w is vertical velocity; v_h is any components of the horizontal wind vector; ∇_h is the horizontal gradient operator; and K_f is the tuning parameter that control the rate of contribution from the cross term, which cannot be represented by the model grid variables. The Leonard term strictly corresponds to the case where $K_f = 1.0$. Because the contribution of the cross term is estimated to be at most equal to that of the Leonard term by large-eddy simulations (Moeng et al., 2010), $K_f = 2.0$ is also possible in cases where both the Leonard and cross terms are considered.

Taking into account the aforementioned background information and the large impacts of moist turbulent diffusion processes on precipitation-related fields, we treat τ^*_{wc} and $\tau^*_{v_hc}$ for some water tracers (moisture, cloud water, and cloud ice) in cases where $K_f = 1.0$ and $K_f = 2.0$ under the settings for the HRMIP run (LEO1 and LEO2 runs, respectively) and the MP run (MP-LEO1 and MP-LEO2 runs, respectively). The impacts of this treatment are described in Section 4.2. Note that we do not consider the diffusion for snow, graupel, and rain because of relatively fast-falling droplets, and the horizontal gradient in Equations 3 and 4 is evaluated on the terrain-following coordinate. As for the latter, it would be better to change this evaluation to the local cartesian coordinate in future model development. Also, in designing the full formulation, we plan to expand the implementation of the Leonard term into temperature and momentum without degrading numerical stability, one of the difficulties in terms of the computational aspects.

While the 38 vertical layers are basically adopted in the present study, we also test the impacts of the vertical resolution enhancement by using 78 layers. The 78-layer vertical coordinate has 400-m thickness in the upper troposphere, which can improve the radiation and circulation fields and TC activities through better representation of cirrus clouds (Seiki et al., 2015) and dynamical processes near cloud tops (Ohno & Satoh, 2015). In addition, the lowest layer in the 78-layer coordinate is thinner than that in the 38-layer coordinate (33 vs. 80 m), so we expect more precise diagnostics of near-surface variables and planetary boundary layer (PBL) physics. An experiment with this vertical resolution enhancement is conducted under the settings for the MP-LEO2 run (MP-LEO2-L78 run).

The settings of the sensitivity experiments in this study are summarized in Table 1. All the simulations are started on 1 June 2004 and integrated for 1 year, and the whole periods of those simulations were used for analyses. This initial date has been used in many previous NICAM studies (Kodama et al., 2012, 2021; Noda et al., 2016; Seiki et al., 2015) and the subsequent 1-year period includes robust activities of representative weather phenomena such as TCs and MJO, so this design is suitable for the evaluation of NICAM. In addition, we expect that integration of 1 year or less is enough to evaluate the sensitivities of model improvement to climatological mean states in precipitation, radiation, and temperature (e.g., Kodama et al., 2021; Noda et al., 2010; Noda et al., 2021; Williams et al., 2013) and to very frequent phenomena such as the precipitation diurnal cycle. Meanwhile, because the robustness of our model improvement for S2S-scale phenomena (e.g., seasonal migration of precipitation bands, MJO, and TCs) should be more carefully discussed in consideration of internal fluctuations, we discuss it appropriately for each topic described later.

The initial atmospheric condition is obtained from the ERA-20C reanalysis (Poli et al., 2016), and the oceanic state is initialized by HadISST 2.2.0.0 (Kennedy et al., 2017). The sea surface temperature is predicted by a mixed-layer slab ocean model with a depth of 15 m, and simultaneously nudged to the observation (HadISST 2.2.0.0) with a relaxation time of 7 days. The initial land condition is the monthly mean climatology of the NICAM simulation at 220-km resolution, as was used for the HighResMIP simulations (Kodama et al., 2021).

2.3. Observational Data Sets

For the model validation in the sensitivity experiments, we use the following data sets:

1. Daily and monthly mean winds and temperature from the Japanese 55-year Reanalysis Project (JRA-55) (Kobayashi et al., 2015) are used to evaluate the atmospheric circulations. Their horizontal resolution is 1.25° × 1.25°, and they cover 29 vertical layers from 1,000 to 50 hPa.
2. Monthly mean radiation fields at the top-of-atmosphere (TOA) and surface from the Clouds and Earth's Radiant Energy Systems (CERES) Energy Balanced and Filled TOA/SFC Edition 4.2 product (Kato et al., 2018; Loeb et al., 2018) are used to evaluate the mean radiation balance and energy transportation. The horizontal resolution of this product is 1.0° × 1.0°.
3. Interpolated daily outgoing longwave radiation from the National Oceanic and Atmospheric Administration polar-orbiting satellite (Liebmann & Smith, 1996) is used to evaluate power spectra of tropical convective activities. The horizontal resolution is 2.5° × 2.5°.
4. Daily and monthly mean rainfall from the Global Precipitation Climatology Project (GPCP) version 1.3 (Adler et al., 2003; Huffman et al., 2001) is used to evaluate the global precipitation fields. The horizontal resolution of this data set is 1.0° × 1.0°.
5. Daily and monthly mean rainfall from the Tropical Rainfall Measuring Mission 3B42 version 7 (Huffman et al., 2007, 2012) is used to analyze the tropical precipitation fields. For direct comparison, the data is interpolated from its original horizontal resolution (0.25° × 0.25°) into the GPCP 1.0° × 1.0° grids using conservative remapping.
6. The hourly climatology of the TRMM-3G68 data set is used to evaluate the precipitation diurnal cycle in the tropics. This climatology is provided by Minobe et al. (2020), who explained the method of producing it. An advantage of using the TRMM-3G68 product is that the artificial phase delay found in TRMM-3B42 can be avoided by no infrared-based estimation (e.g., Kikuchi & Wang, 2008). This data is interpolated into the 0.25° × 0.25° grids using conservative remapping.
7. Best-track data sets compiled by the International BestTrack Archive for Climate Stewardship (IBTrACS) (Knapp et al., 2011) are used to evaluate simulated TC intensity, genesis, and tracks. The limitations of these data sets are briefly described in Yamada et al. (2017).

All the data except for the TRMM-3G68 hourly climatology directly cover the simulation period. Because the raw data in TRMM-3G68 is not available online, we use its hourly climatology, which is openly accessible to the observed statistics of tropical precipitation diurnal cycle (Minobe et al., 2020). Upon comparison of the observations and the results of the sensitivity experiments, the model data are interpolated into the same spatio-temporal resolutions as for the targeted observational data.

3. Comparison of the Two Representative Simulations: HighResMIP-Tuned Versus MJO-Tuned Settings

In this section, we compare the HRMIP and MJO runs, which are designed specifically to better represent the climatological mean radiation distributions and S2S-scale MJO behavior, respectively. We examine the difference in deep convection characteristics and their relationship to the moisture evolution, and then compare several simulated 1-year mean fields and disturbances to set an approach toward model improvement.

3.1. Deep Convection Characteristics

We first detect deep convective cores in the tropics for the HRMIP and MJO runs using 6-hourly and 1.25°-grid (area-mean) snapshots. For the detection of deep convective cores, two simple criteria are imposed over 20°S–20°N: (a) vertical velocities at 700 hPa (w_{700}) have local maximum with greater than 0.2 m/s, and (b) both cloud water and cloud ice contents integrated over the 1,000–100 hPa layer are non-zero. The spatial scale of convective cores is chosen to have effective resolution (around 8 times grid spacing in Arakawa A-grid), which is expected to be a minimum scale that can intrinsically affect the model performance. In the real atmosphere, these cores correspond to MCSs or cloud clusters (Houze, 1993).

Figures 2a and 2b show an example of deep convective cores that are detected in the HRMIP and MJO runs, respectively. In both runs, pairs of upward and downward motions are realized in large-scale convective envelopes, and as indicated by green circles, convective cores are reasonably well detected within the envelopes. A comparison of the frequency of w_{700} over 20°S–20°N in both runs (Figure 2c) suggests that a threshold of 0.2 m/s for w_{700} captures sufficiently strong convection in both runs, although the MJO run has a slightly lower frequency of w_{700} greater than 0.2 m/s.

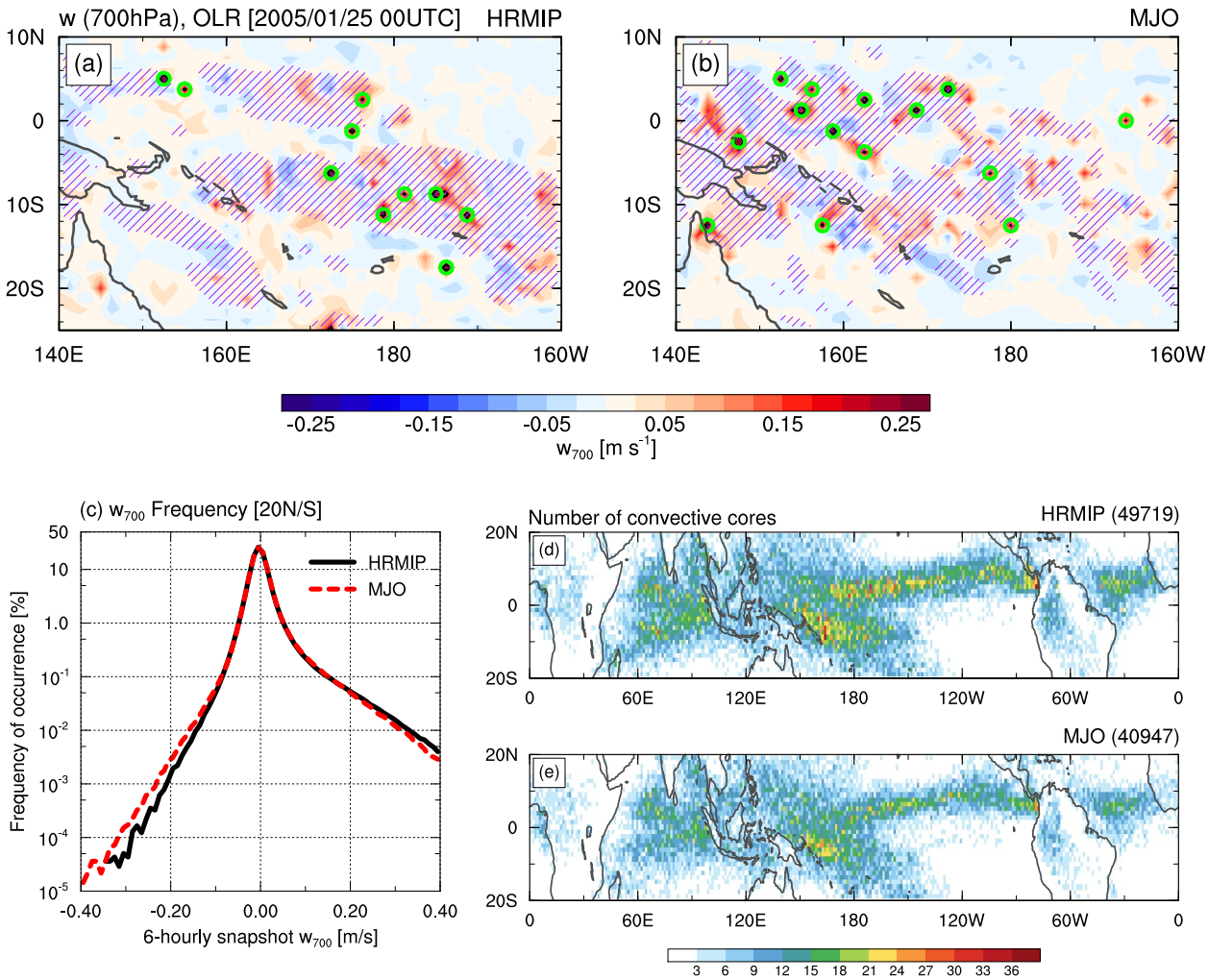

Figure 2. (a and b) Snapshots of vertical wind velocities at 700 hPa (shading and contours for 0.2 m s^{-1}) and OLR less than 200 W m^{-2} (hatching) at 00:00 UTC, 25 January 2005 for the (a) HRMIP and (b) MJO runs. Green open circles represent detected deep convective cores. (c) Frequency distributions of 6-hourly vertical wind velocities at 700 hPa in 20°S–20°N for the HRMIP (black) and MJO (red) runs. (d and e) Horizontal maps of the number of detected deep convective cores for the (d) HRMIP and (e) MJO runs. Total number of deep convective cores are denoted at the upper-right corner of the figures.

In Figures 2d and 2e, the spatial distributions of the number of convective cores in the 1-year simulations are significantly different from each other. For the HRMIP run, more deep convection is activated especially in the ITCZ and the South Pacific convergence zone, which results in the meridional splitting of active convective areas over the equatorial Pacific (Figure 2d). For the MJO run, this feature is not confirmed, and the total number of convective cores is ∼20% smaller (Figure 2e). These results, as well as those shown in Figure 2c, confirm that the HighResMIP-tuned setting favors strong deep convection more than the MJO-tuned setting, as implied by Nasuno (2021).

The above differences in the two runs are related to the different relationship between individual deep convection and moisture accumulation and detrainment. To understand this, we next compare the moisture evolution associated with deep convection triggering. In Figures 3a and 3b, we examine the lagged-composite time-height evolution of specific humidity anomalies for the HRMIP and MJO runs, respectively. To focus on variations during the life cycle of convection, we define the anomalies as deviations from the 96-hr mean before and after deep convection triggering ($t = 0$ hr). While the shallow-to-deep convection transition is found in both runs, the moisture–convection relationship is clearly different between the two. For the MJO run (Figure 3b), the contrast of moist/dry anomalies in the PBL/free troposphere is more obvious until deep convection triggering, and free-tropospheric preconditioning takes slightly longer, as inferred from the fact that zero contours in the MJO run

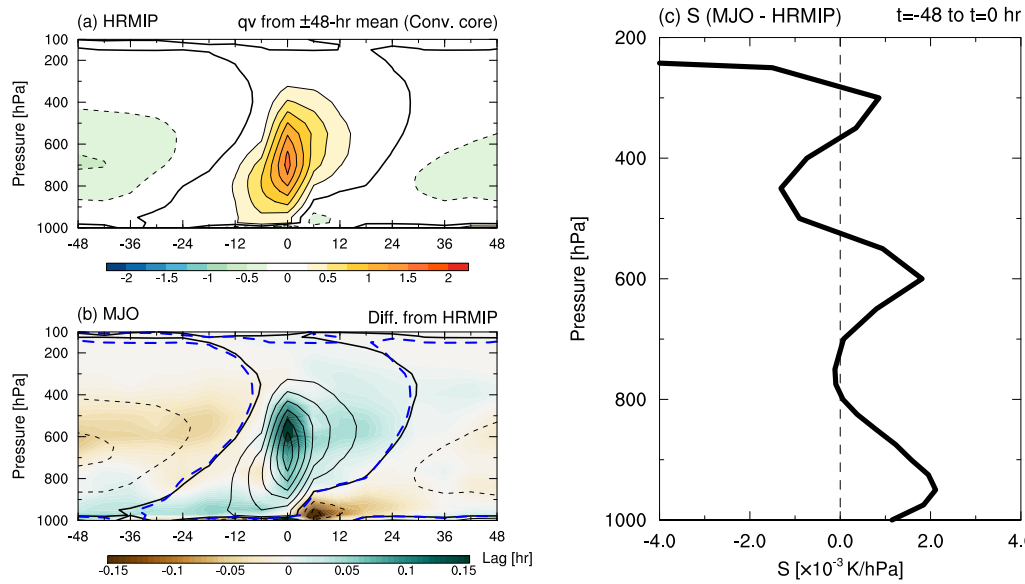

Figure 3. (a) Time-height section of lagged-composite specific humidity anomalies (g kg^{-1}) during the 96-hr evolution of deep convective cores for the HRMIP run. The reference time for composite (t = 0 hr) is when deep convective cores are detected, and the anomalies are defined as deviations from the ±48-hr mean. Thick contours denote zero values. (b) The same as (a), but for the MJO run (black contours) and its difference from that for the HRMIP run (shading). Contour interval is 0.25 g kg^{-1}, with negative (zero) contours dashed (thickened). Blue dashed contours denote zero values for the HRMIP run. (c) Vertical profile of the difference in the composite static stability (S) from −48 to 0 hr for the MJO run from that for the HRMIP run.

(black) appear about 6 hr before those in the HRMIP run (blue) and have slightly smaller slopes. This indicates that deep convection is less prone to trigger in the MJO run. Also, the MJO run allows stronger and continuous mid-to-upper tropospheric moistening maximized in 600–500 hPa after t = 0 hr, in conjunction with stronger PBL drying, which is partly due to active moisture transport to the free troposphere. These behaviors are certainly favorable for good MJO simulations (e.g., Hannah & Maloney, 2011; Hirons et al., 2013; Klingaman & Woolnough, 2014; Nasuno, 2021).

The modified moisture–convection relationship in the MJO run results from the change in the vertical profile of the atmospheric static stability. Figure 3c shows the difference in the static stability (S) before t = 0 hr from that in the HRMIP run. Note that the static stability in pressure coordinate is given by

$$S = -\frac{T}{\theta}\frac{\partial \theta}{\partial p} \tag{5}$$

where T is temperature; and θ is potential temperature. For the MJO run, the slower shallow-to-deep convection transition is associated with the increased static stability in the PBL, and maximized mid-tropospheric moistening after t = 0 hr corresponds to the more stable layer in 600–500 hPa. Also, a pair of a decrease and increase in static stability in 500–300 hPa can support moist anomalies there after t = 12 hr via modest vertical transport and detrainment.

The cloud microphysics-related change in static stability, which can alter the moisture–convection relationship, is interpreted from the difference in the heating profile affected by vertical distributions of the water substances. Figures 4a and 4b show the vertical profile of tropical-mean diabatic heating from microphysics and radiation processes for the HRMIP and MJO runs, respectively. Figure 4c shows its difference as the MJO run minus the HRMIP run. First, microphysics processes for the MJO run induce more cooling in the PBL, consistent with the increased static stability there. As inferred from vertical profiles of tropical-mean water substances (Figures 4d–4f), this change is caused by more rain evaporation in the PBL (indicated by the loss of rain near the surface). Second, despite more mid-tropospheric heating in the MJO run, the vertical gradient of heating around the freezing level (600–500 hPa) is slightly larger than in the HRMIP run (Figure 4c). This reflects more frequent ice

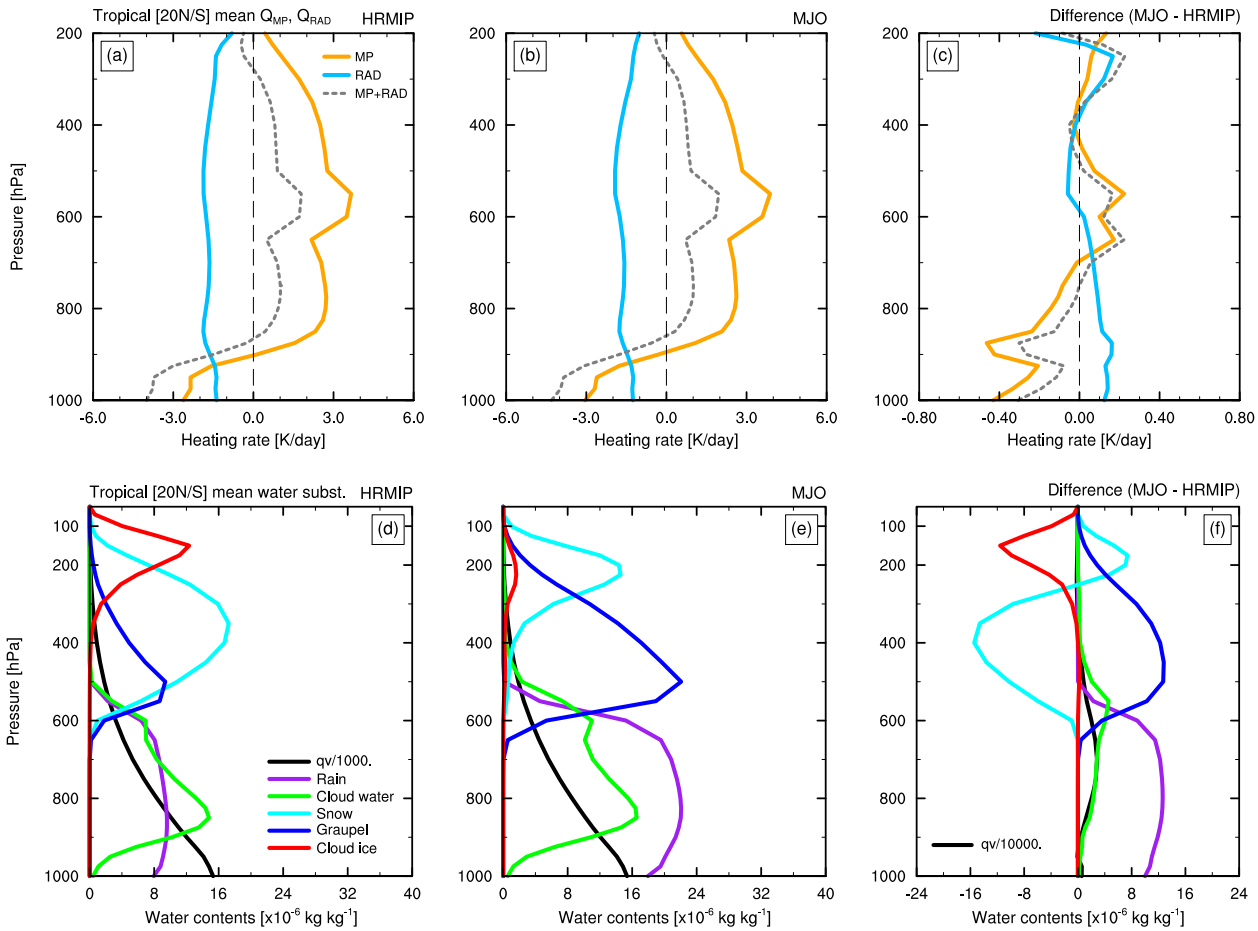

Figure 4. (a and b) Vertical profiles of the annual-mean tropical mean (20°S–20°N) diabatic heating from cloud microphysics (orange) and radiation processes (blue) and their sum (gray dashed) for the (a) HRMIP and (b) MJO runs. (c) As in (a and b), but for the differences between HRMIP and MJO runs (MJO minus HRMIP). (d–f) Vertical profiles of the annual-mean tropical mean mass concentration of water substances for the (d) HRMIP and (e) MJO runs and (f) the difference between the two (MJO minus HRMIP): water vapor (divided by 10^3 for (d and e) and 10^4 for (f); black), rain (purple), cloud water (green), snow (cyan), graupel (blue), and cloud ice (red).

(mainly graupel) condensation and melting above and below the freezing level, respectively (Figure 4f), which are a source of the robust stable layer. These features are rooted in both the use of T08-version microphysics and the slower terminal velocity of rain in the MJO run; the T08 version tends to produce more graupel and rain melting from graupel, and the resulting a greater number of raindrops are evaporated more easily by slower rain falling. Although drier anomalies near the surface after deep convection triggering in the MJO run (Figure 3b) appear to contradict the rain evaporation, they can be the result of active moisture transport and/or convective downdraft.

In addition, the MJO run has more radiative heating around 250 hPa probably because the amount of snow peaks at a higher altitude, at 200 hPa rather than 350 hPa (Figures 4d and 4e). This heating profile presumably makes the stratification around 300 hPa more stable (Figure 3c). This is realized by the T08-version microphysics, which produce snow at a higher altitude in the MJO run than in the HRMIP run, and by the enhanced snow production due to tuning that sets the terminal velocity of snow to be slower.

To summarize, the differences in cloud microphysics properties can introduce diversity in the moisture–convection relationship through changes in the heating profile that affect the static stability. Specifically, in the MJO run, slower rain and snow falling makes deep convection less prone to trigger, and it contributes to more moisture storage in the mid-troposphere. This makes the tropical troposphere moister for the MJO run on average (Figure 4f).

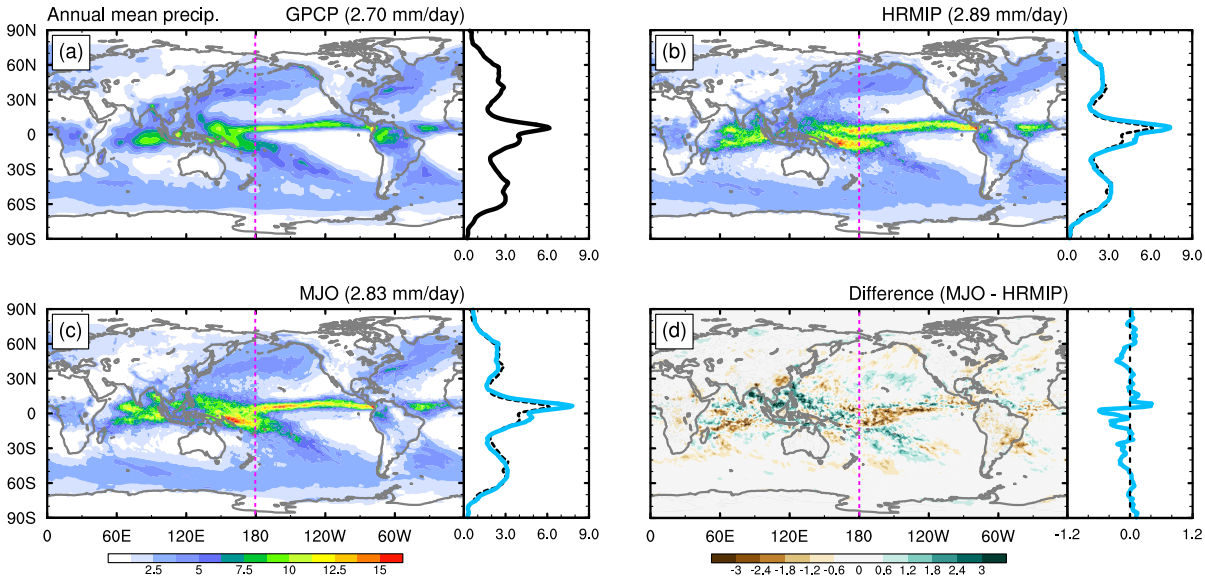

Figure 5. Horizontal maps of the annual-mean precipitation (mm day^{-1}) for the (a) Global Precipitation Climatology Project (GPCP) product, (b) HRMIP and (c) MJO runs, and (d) its difference between the two runs (MJO minus HRMIP). Zonal mean distributions are plotted in right panels with solid lines, where the GPCP distribution is also replotted with black dashed lines in (b) and (c). Global mean values are denoted at the upper-right corner of figures. Dotted pink lines indicate the dateline.

3.2. Simulated Climatological Mean States and Weather Disturbances

In consideration of deep convection characteristics for the HRMIP and MJO runs, we interpret the climatological mean states and weather disturbances simulated in those runs. First, the annual-mean precipitation for the GPCP and the HRMIP and MJO runs are compared (Figures 5a–5c). Both simulations have much stronger precipitation than the GPCP, especially over the western Pacific and ITCZ. There are two notable differences in precipitation distributions between the HRMIP and MJO runs (see also Figure 5d). One is that the precipitation band around the dateline in the Southern Hemisphere extends farther eastward in the HRMIP run, which corresponds to the double ITCZ-like bias in the NICAM HighResMIP simulation (Kodama et al., 2021). The other is that tropical precipitation in the MJO run is more abundant around the Maritime Continent than in the HRMIP run, as in the GPCP. The absence of a double ITCZ and the enhancement of precipitation over the Maritime Continent in the MJO run can be partly explained by the fact that more PBL cooling increases the sensitivity of convection to low-level moisture and hence makes convection less prone to trigger (cf., Figure 3b). In fact, the relationship between rain evaporative cooling and the ITCZ structure is consistent with Bacmeister et al. (2006). The zonal contrast of equatorial precipitation is directly linked to the representation of the Walker circulation and monsoon, which seamlessly affect S2S-scale phenomena. Thus, its control by model physics is one of the important aspects in k-scale climate simulations.

Whereas the mean precipitation fields are reproduced more realistically in the MJO run, the representation of the mean outgoing longwave and shortwave radiation (OLR and OSR) distributions at the TOA is better in the HRMIP run. Figures 6b and 6c display the annual-mean OLR bias in the HRMIP and MJO runs, respectively, and the difference between the two is shown in Figure 6d. Compared to the HRMIP run, in which OLR distributions are relatively well simulated globally except for over the deep convective areas and lands in the tropics, the MJO run has significant negative OLR biases, especially in the mid-to-high latitudes. This pronounced OLR bias in the MJO run is caused by more snow production at the upper troposphere, which stems from the cloud microphysics tuning (Figure 4e). As for OSR, both runs suffer from negative biases (i.e., too much shortwave input) off Peru and California and over the Southern Ocean due to the small low-cloud fraction (Figures 6f and 6g). Otherwise, the MJO run tends to have larger OSR globally compared to the HRMIP run because of increased cloud water (Figures 6h and 4f), leading to positive OSR biases especially in areas with negative OLR biases (Figures 6c and 6g).

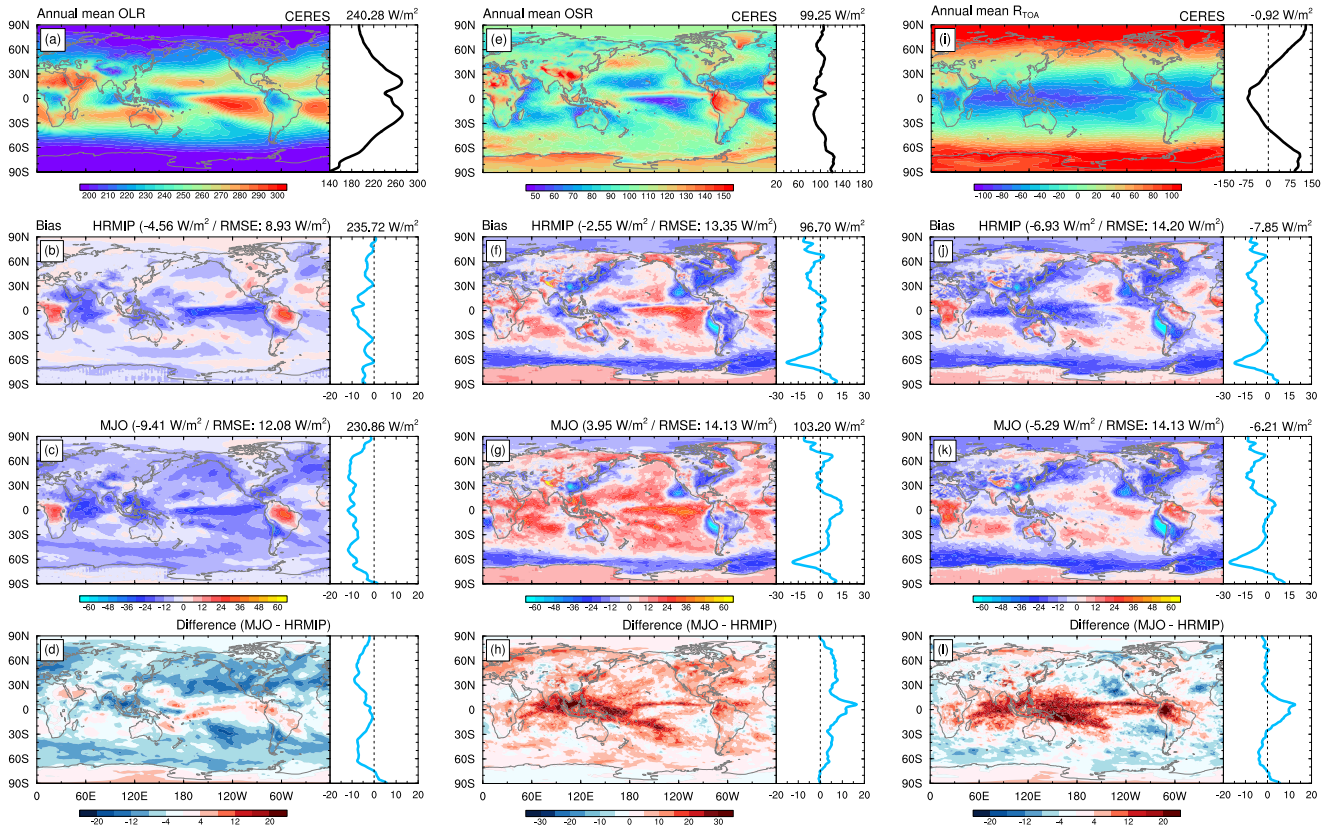

Figure 6. (a) As in Figure 5a, but for OLR (W m^{-2}) at the TOA obtained from the CERES. (b–d) As in (a), but for the OLR bias at the TOA against the CERES for the (f) HRMIP and (g) MJO runs, and (d) its difference between the two runs (MJO minus HRMIP). Positive (negative) values indicate upward (downward) radiative fluxes. Global mean raw values are denoted at the upper side of figures, and global mean bias and area-weighted root-mean-squared error are provided for (b–d). (e–h) As in (a–d), but for OSR at the TOA. (i–l) As in (a–d), but for net radiation at the TOA.

Figures 6i–6l provide information about net radiation at the TOA to sum up the aforementioned OLR and OSR fields. In the MJO run (Figure 6k), the net radiation bias is smaller, especially in the tropics, and the global-mean radiation balance is better than in the HRMIP run (Figure 6j): −5.29 W m^{-2} in the MJO run, −6.93 W m^{-2} in the HRMIP run, each compared against the observation. However, this better balance is the result of error compensation between largely negative OLR and positive OSR biases in the MJO run, while both biases are negative in the HRMIP run. The similar compensation in the MJO run is also found in the root-mean-squared error (RMSE) values. Of course, it would be better to improve the mean radiation balance with reduced biases in both the OLR and OSR distributions.

Comparisons of the above climatological mean states support the notion that it is desirable to obtain a setting incorporating the merits unique to the HRMIP and MJO runs, and this notion is also reinforced by the analysis of the weather disturbances such as equatorial waves and the MJO. Figure 7 presents normalized wavenumber-frequency power spectra in the equatorially symmetric and antisymmetric components of daily (6-hourly) OLR in 15°S–15°N for the observation (HRMIP and MJO runs), following Wheeler and Kiladis (1999) or Takasuka et al. (2018). In the symmetric component (Figures 7a–7c), gravity-wave modes such as Kelvin and westward inertia-gravity waves are amplified more in the HRMIP run, whereas more rotational type modes such as equatorial Rossby waves and tropical depression (TD)-type disturbances are amplified more in the MJO run (Figures 7b and 7c). Also, in both runs, the weaker wave modes (relative to other modes) tend to be weaker than the observation (Figure 7a). These results can be explained by the idea that the slower shallow-to-deep convection transition (i.e., longer moisture convective adjustment time scale) and the moister environment in the MJO run is favorable for the realization of moisture-coupled rotational modes rather than gravity-wave modes (e.g., Adames et al., 2019; Yasunaga & Mapes, 2012). Interestingly, the strength of MJO signals does not differ between the runs, possibly because the MJO can be a mixture of gravity-wave and moisture-coupled rotational modes (e.g.,

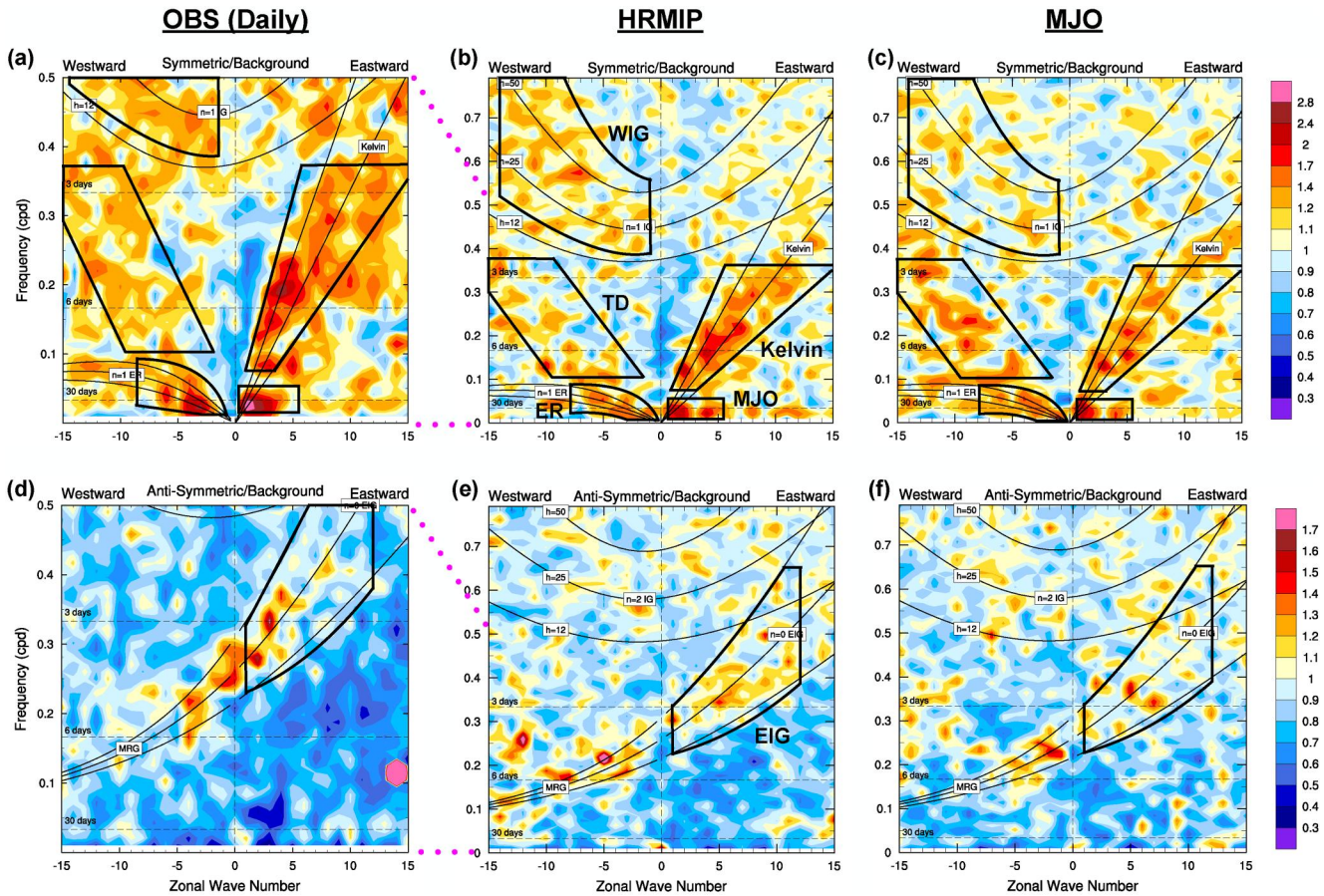

Figure 7. (a–c) Wavenumber-frequency power spectra for the equatorially symmetric component of OLR over the simulation period for (a) the daily observation, and 6-hourly outputs from the (b) HRMIP and (c) MJO runs. Power spectra are summed from 15°S to 15°N, and plotted as the ratio of raw to background power. (d–f) The same as (a–c) but for the equatorially antisymmetric component. Abbreviations of WIG, TD, ER, MRG, and EIG indicate westward inertia-gravity waves, tropical depressions, equatorial Rossby waves, mixed Rossby-gravity waves, and eastward inertia-gravity waves, respectively. Dispersion curves for corresponding equatorial waves are plotted for equivalent depths (h) of 12, 25, and 50 m. n means the number of meridional modes.

Masunaga et al., 2006; Straub & Kiladis, 2003; Takasuka & Satoh, 2020; Yasunaga & Mapes, 2012). For the antisymmetric component (Figures 7d–7f), the HRMIP run favors eastward inertia-gravity waves in more cohesive wavenumber-frequency bands, although their amplitudes are still underestimated compared to the observation. This feature is consistent with the results for the symmetric component.

The analyses in this subsection reveal that taking the intermediate characteristics of the HRMIP and MJO runs is the best option for model improvement. The specific revisions of the model setting necessary for achieving this goal are described next.

4. Major Model Updates and Their Impacts on the Moisture–Convection Relationship

In Section 3, we find the moisture–convection relationship and cloud microphysics characteristics should be altered to incorporate good performances of the HRMIP and MJO runs in terms of both the climatological statistics and weather. Specifically, deep convection triggering should be more sensitive to environmental moisture and the troposphere should be moister than in the HRMIP run, although not as much as in the MJO run. Also, the representation of upper-tropospheric ice condensation should be improved for better mean radiation balance, which can be achieved by reconsidering cloud microphysics and vertical resolutions. Based on these strategies, three major model updates are introduced: (a) retuning of the cloud microphysics parameters; (b) implementation of turbulent diffusion by the Leonard and cross terms; and (c) vertical resolution enhancement. Lastly, we briefly describe the impacts of these model updates on convective organization, one of the important aspects related to the moisture–convection relationship.

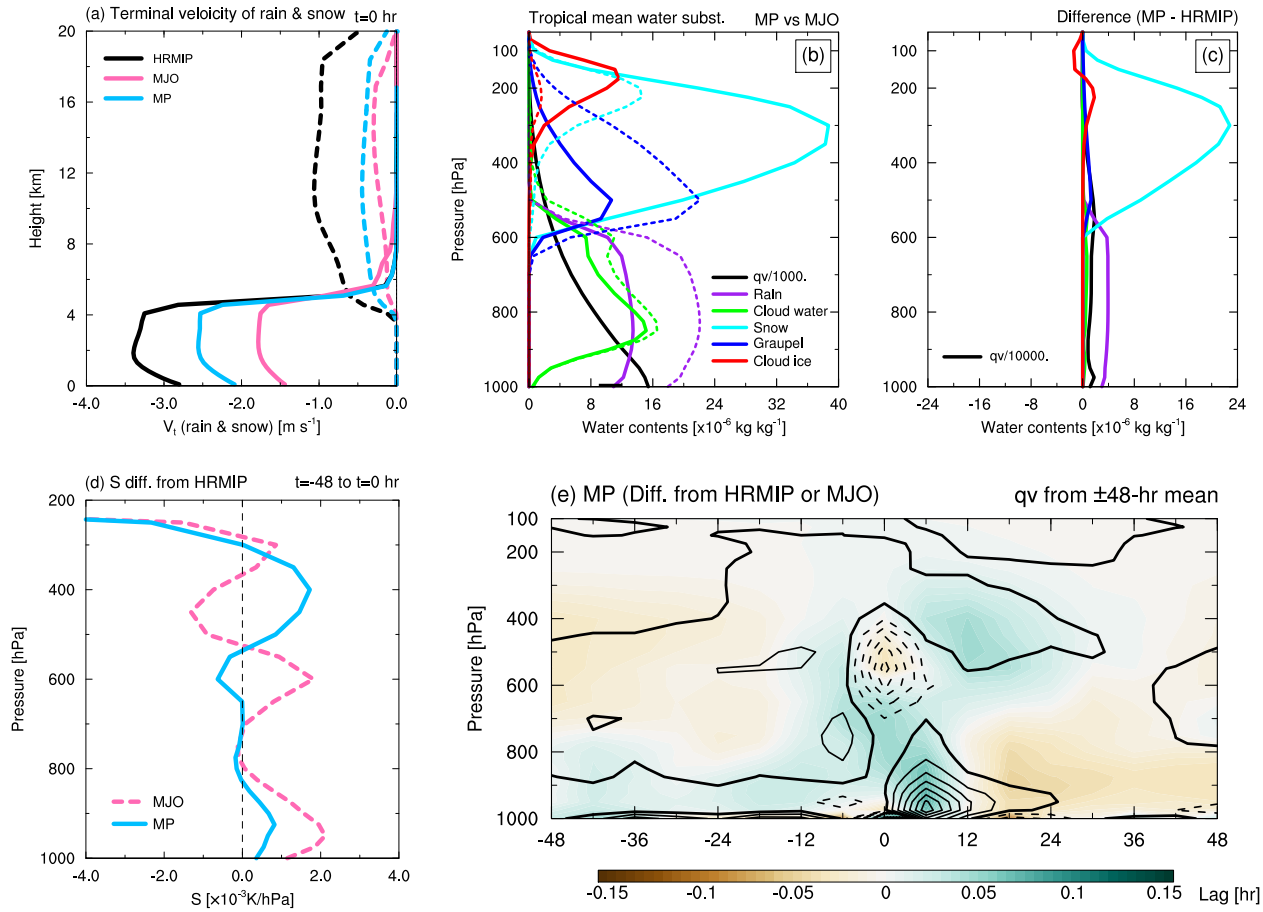

Figure 8. (a) Vertical profiles of composite terminal velocities of rain (solid) and snow (dashed) when deep convective cores are detected (t = 0 hr) for the HRMIP (black), MJO (pink), and MP runs (blue). (b) The same as Figure 4c, but for the MP (solid) and MJO runs (dashed). (c) The same as Figure 4e, but for the difference between the MP and HRMIP runs. (d) The same as Figure 3c, but for the MJO (pink) and MP runs (blue). (e) The same as Figure 3b, but for the difference in the MP run from the HRMIP (shading) and MJO runs (contours). Contour interval is 0.04 g kg^{-1}, with negative (zero) contours dashed (thickened).

4.1. Retuning of the Cloud Microphysics Parameters

To determine the intermediate moisture–convection relationship between the HRMIP and MJO runs, we first retune the vertical profiles of the terminal velocity of snow and rain in the MP run to take their intermediate values from the HRMIP and MJO runs (Figure 8a). Here, the RS14-version microphysics is used instead of the T08-version microphysics adopted in the MJO run, because we intend to revise the height and amount of ice, snow, and graupel production based on the RS14 version's updates of ice processes.

As shown in Figures 8b and 8c, this retuning of the MP run alters the vertical structure of the tropical-mean water substances from that in the MJO or HRMIP run. The terminal velocity of rain and snow is slower in the MP run than in the HRMIP run, which produces more rain and snow (Figure 8c). Also, the intermediate terminal velocity of rain between the HRMIP and MJO runs makes rain evaporation in the PBL stronger (weaker) than in the HRMIP (MJO) run (Figures 4d, 4e, and 8b). Furthermore, compared to the MJO run, the change in the microphysics scheme in the MP run leads to less graupel and rain, more cloud ice, and particularly at lower levels, more snow (Figure 8b).

As a result, the vertical profile of the static stability S is different from that in the HRMIP and MJO runs. Figure 8d shows the differences in the vertical profiles of S (from the HRMIP run) before deep convection triggering for the MJO and MP runs. In the MP run, the static stability in the PBL increases because of stronger evaporative cooling than in the HRMIP run, just like in the MJO run, but the degree of increase is reduced compared to that in the MJO run. The mid-to-upper tropospheric (500–300 hPa) static stability is also increased because of enhanced radiative heating associated with more snow production than in the HRMIP run. Meanwhile, the melting-layer stabilization

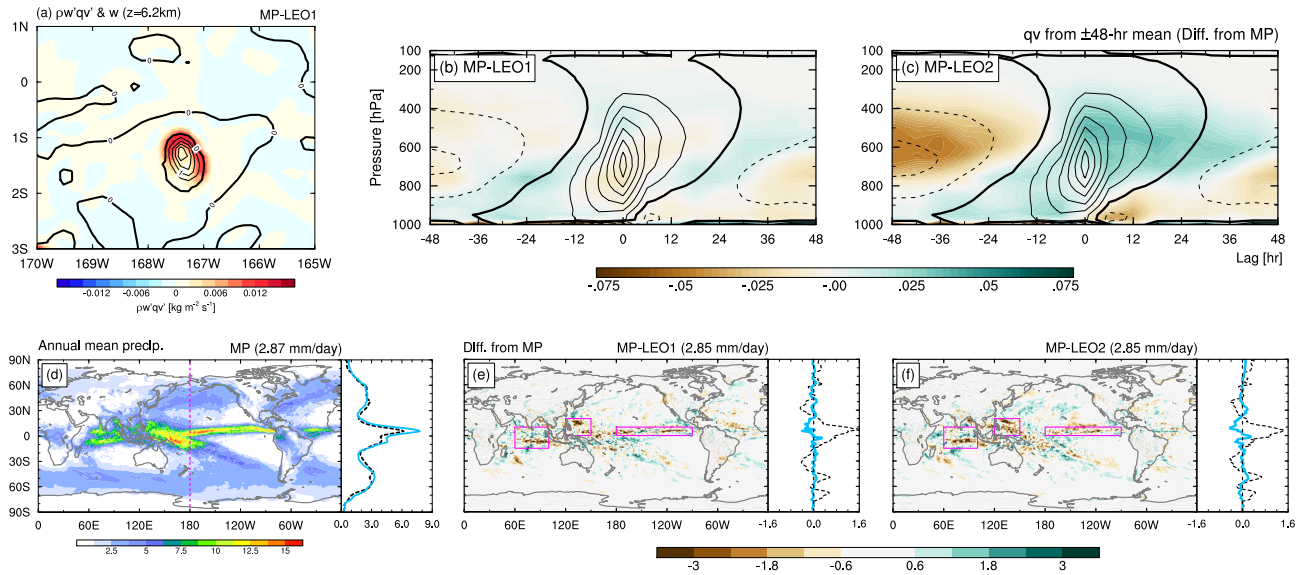

Figure 9. (a) Snapshot of vertical moisture flux by the Leonard term (shading) and positive vertical wind velocities (contours) at a height of 6.2 km for the MP-LEO1 run. Contour interval is 0.5 m s^{-1}, with zero values thickened. (b and c) The same as Figure 3b, but for the (b) MP-LEO1 and (c) MP-LEO2 runs and shading represent their differences from the MP run. (d) The same as Figure 5b, but for the MP run. (e and f) The same as Figure 5d, but for the differences in the (e) MP-LEO1 and (f) MP-LEO2 runs from the MP run. Black dashed lines for the zonal mean plots indicate the differences from Global Precipitation Climatology Project observation. Global-mean raw values are denoted at the upper-right corner of the figures. Pink squares enclose the three representative areas used for the computation of domain-mean precipitation: the Indian Ocean (15°S–10°N, 60°–100°E), western North Pacific (0°–20°N, 120°–150°E), and intertropical convergence zone (0°–10°N, 180°–90°W).

effect found in the MJO run is not significant, possibly because the magnitude of conversion from graupel to rain is smaller than in the MJO run in accordance with less graupel.

The above changes in static stability result in a quantitatively retuned moisture–convection relationship that retains the qualitative features of the MJO run. Figure 8e shows the same moisture evolution as in Figure 3b but for the MP run. In the MP run, similar to the MJO run, more moisture is accumulated in the PBL before deep convection triggering (t = 0 hr) and subsequently detrained in the mid-troposphere than in the HRMIP run. In addition, the amplitudes of this evolution are reduced in comparison with the MJO run. These aspects are certainly intermediate between the HRMIP and MJO runs.

Another important revision in the cloud microphysics scheme is to introduce the cloud ice falling process. Because cloud ice falling decreases (increases) ice clouds above (below) about 200 hPa (Figure 8c), it contributes to an increase in the climatological mean OLR at the TOA and in turn affects the temperature field. In fact, this new treatment can mitigate negative OLR and high upper-tropospheric temperature biases partly caused by ice and snow production in the MP run (not shown).

4.2. Implementation of Turbulent Diffusion by the Leonard and Cross Terms

As described in Section 2.2, we newly consider turbulent diffusion from CRM-grid scale eddies, which are represented by the Leonard and cross terms in Equation 2, for moisture and cloud water and ice. Because the contributions from these terms become large where the horizontal gradients of both horizontal/vertical wind velocities and tracers are large (see Equations 3 and 4), they are expected to be effective around individual storms. Figure 9a displays a snapshot of vertical moisture fluxes by the Leonard term (computed with Equation 3 for $K_f = 1.0$) and vertical winds at $z = 6.2$ km in the MP-LEO1 run. This map clearly shows that turbulent transport by the Leonard term is enhanced only in the vicinity of a convective core. That is, the implementation of the Leonard- and cross-term contributions enables us to incorporate a part of lateral mixing associated with deep convection.

The lateral mixing by the Leonard and cross terms has an impact on how much moisture is diffused in accordance with the evolution of individual deep convection. Figures 9b and 9c show the same as Figure 8e but for the difference from the MP run (i.e., without Leonard- and cross-term contributions) for the MP-LEO1 and MP-LEO2 runs, respectively. In both runs, more moisture remains from the lower to mid-troposphere even after

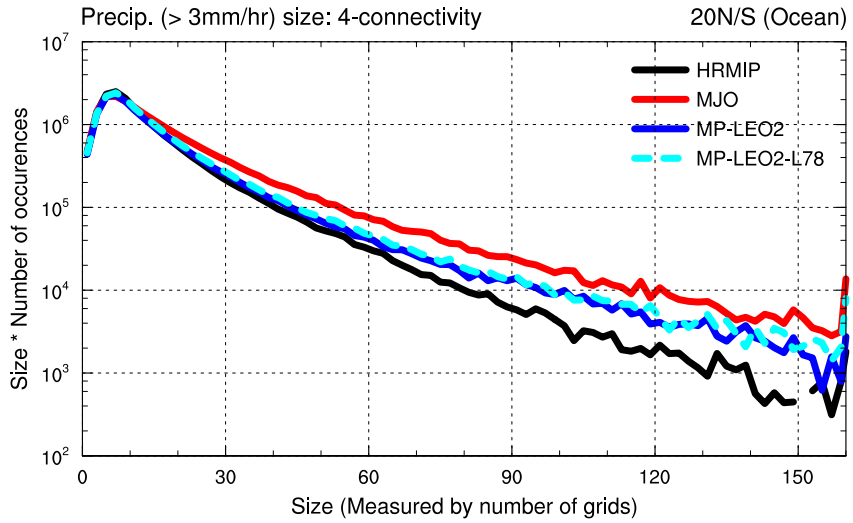

Figure 10. Number of occurrences multiplied by the size of precipitation systems for each binned size for the HRMIP (black), MJO (red), MP-LEO2 (blue), and MP-LEO2-L78 runs (cyan dashed). The size of precipitation systems is measured by the number of 4-connectivity tropical (20°S–20°N) oceanic 0.25° × 0.25° grids with instantaneous precipitation more than 3 mm hr^{-1}. The data are binned by the interval of two grid sizes.

$t = 24$ hr, which seems to be a result of detrainment-like processes. This evolution is more prominent in the MP-LEO2 run ($K_f = 2.0$), indicating that the consideration of both the Leonard and cross terms leads to more moisture diffusion in deep convective areas.

This turbulent diffusion effect also modulates mean precipitation fields. Figure 9d shows the annual-mean precipitation in the MP run, and Figures 9e and 9f show the difference from the MP run for the MP-LEO1 and MP-LEO2 runs, respectively. Compared to the MP run, which has precipitation distributions similar to those in the MJO run in terms of no double ITCZ and enhanced precipitation over the western Pacific, the precipitation amount tends to decrease around active precipitation areas in both runs. For example, domain-mean precipitation in the MP-LEO1 run is reduced over the Indian Ocean (−0.12 mm day^{-1}), western North Pacific (−0.91 mm day^{-1}), and ITCZ (−0.45 mm day^{-1}). The decrease in precipitation is more significant in the MP-LEO2 run; the precipitation changes from the MP run over the above three areas are −0.29, −1.08, and −0.60 mm day^{-1}, respectively. The inclusion of the Leonard term mitigates the bias of too much precipitation in the tropics, although the bias remains (see black dashed lines in Figures 9e and 9f). Hence, turbulent diffusion in the vicinity of deep convection plays an important role in suppressing excessively strong precipitation.

4.3. Vertical Resolution Enhancement

As described in Section 2.2, higher vertical resolutions in the upper-troposphere help to represent cirrus clouds and dynamical processes near the tropopause, leading to better reproducibility of radiation distributions (Seiki et al., 2015) and TC intensity (Ohno & Satoh, 2015). Also, a thinner layer near the surface enables more precise diagnostics for near-surface variables, which can affect convection triggering. Thus, the effects of increasing the number of vertical layers from 38 to 78, which satisfies these aspects, is tested in the MP-LEO2-L78 run. This enhancement of vertical resolution alters the moisture–convection relationship, as well as the climatological mean radiation, temperature, and circulation fields shown in Section 5.1; the PBL-to-mid-level moistening observed in the deep convective evolution, which is reinforced by the revisions of the cloud microphysics and turbulent processes that are described in the previous two subsections, is slightly reduced (not shown). This is consistent with Ohno et al. (2019), who showed that higher vertical resolutions weaken the subgrid-scale turbulent mixing near convective cores and reduce the relative humidity.

4.4. Changes in Convective Organization as a Result of the Model Updates

This subsection briefly discusses how our model updates alter convective organization, one of the important features in deep convection. Here we focus on changes in the size of organized rainfall systems. Figure 10

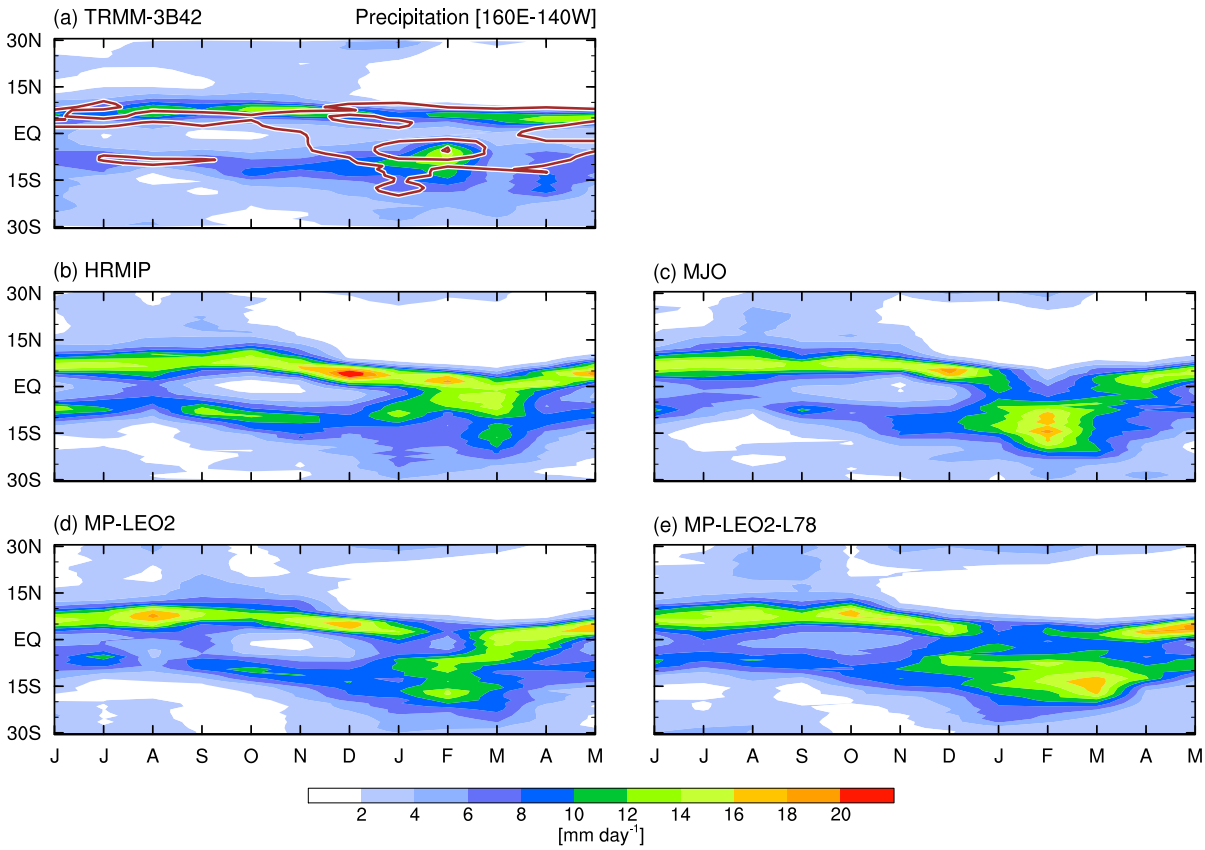

Figure 11. Time-latitude diagrams of the monthly-mean precipitation averaged over 160°E−140°W (shading) for the (a) TRMM-3B42 product, (b) HRMIP, (c) MJO, (d) MP-LEO2, and (e) MP-LEO2-L78 runs. In (a), the standard deviation for 1998–2012 is also plotted with contours, whose interval is 1.8 mm day^{-1}. The *x*-axis denotes every month from June 2004 to May 2005.

compares the size distributions of precipitation systems over the tropical ocean, which are detected by 4-connectivity grids (0.25° × 0.25°), between the HRMIP, MJO, MP-LEO2 (adopting the updates in Sections 4.1 and 4.2), and MP-LEO2-L78 (adopting all the updates) runs. While the HRMIP run fails to simulate rainfall systems with a larger size, this tendency is largely mitigated in the other three experiments. Notably, the MP-LEO2 and MP-LEO2-L78 runs have size distributions that are intermediate between those of the HRMIP and MJO runs, consistent with the modification of the moisture–convection relationship. This suggests two possibilities: (a) more inhibition of local convection triggering due to microphysics tuning favors more organized systems being balanced with large-scale subsidence; and (b) mid-tropospheric moistening due to detrainment and to turbulent diffusion around deep convection aids convective organization by widening the moisture spatial scale.

5. Impacts of the Model Updates on the Simulated Fields

In this section, we evaluate the simulated fields in the sensitivity experiments over a wide range of temporal scales to show that the model updates described in Section 4 realistically represent both the climatological mean states and weather disturbances. Here we mainly compare the results of the HRMIP, MJO, MP-LEO2, and MP-LEO2-L78 runs, because the moisture–convection relationship obtained in the MP-LEO2-based physics (i.e., $K_f = 2.0$ as in Moeng et al. (2010)) is closest to our goal.

5.1. Climatological Mean States

We first examine the impacts of the model updates on the representation of the ITCZ. Figure 11 shows the time-latitude diagrams of monthly-mean precipitation averaged over the central Pacific (160°E−140°W) for the

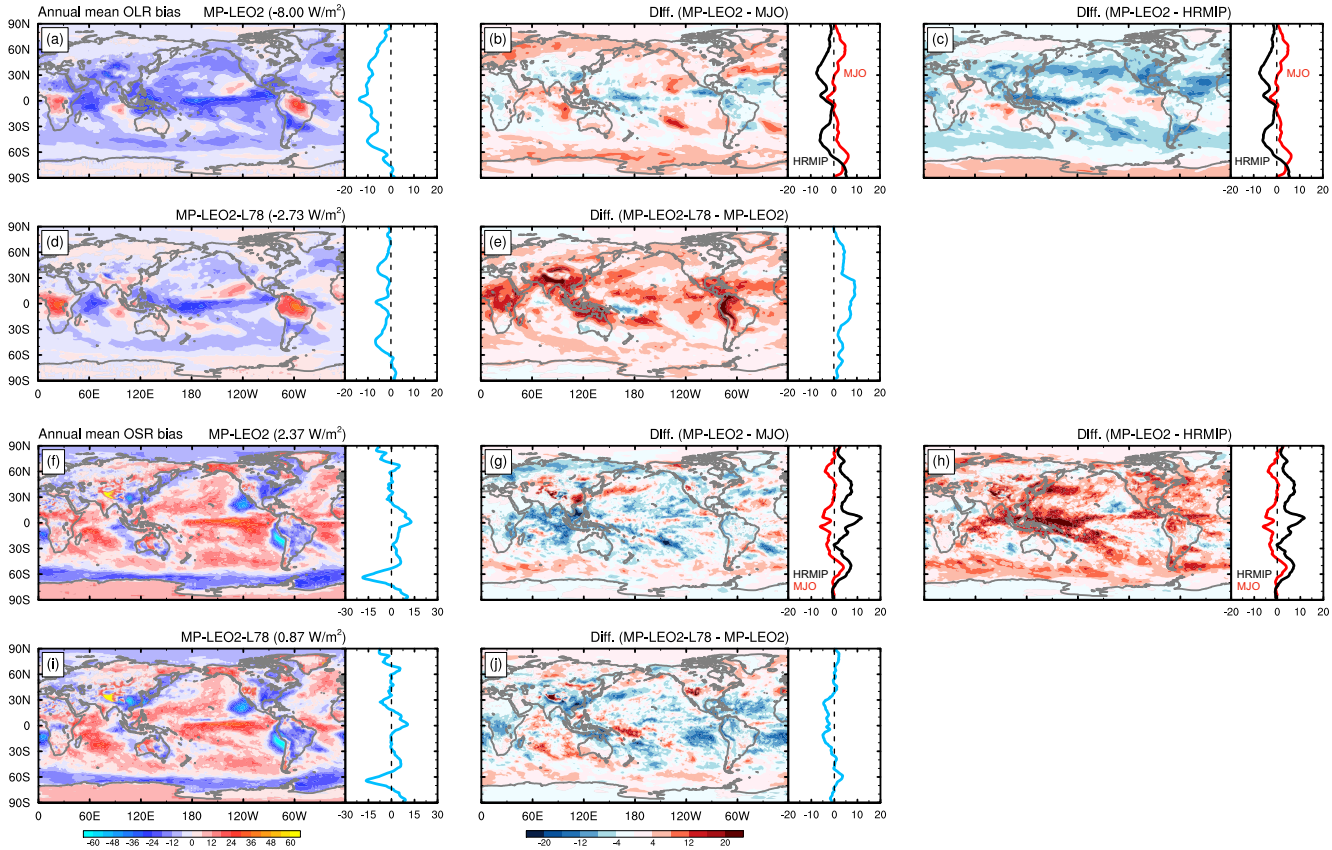

Figure 12. (a–c) Horizontal maps of (a) the annual-mean OLR bias (W m^{-2}) for the MP-LEO2 run and (b, c) its difference from the (b) MJO and (c) HRMIP runs. Zonal mean distributions are also plotted in the right panels, in which in (b, c), black and red lines correspond to the HRMIP and MJO runs, respectively. Global-mean values are denoted at the upper-right corner of (a). (d and e) The same as (a and b), but for (d) the MP-LEO2-L78 run and (e) its difference from the MP-LEO2 run. (f–j) As in (a–e), but for the annual-mean OSR bias.

observation and sensitivity experiments. For the observation, its standard deviations during the period of 1998–2012 (i.e., 15 years around 2004/05) are also plotted to show the interannual fluctuations. While the observed precipitation has a single ITCZ around 5°N, except in boreal winter (Figure 11a), the HRMIP run simulates the double ITCZ structure especially in boreal autumn (September–November) and early summer (June–July) (Figure 11b). In particular, the southern band precipitation in boreal autumn is so active that its amount exceeds two standard deviations for the observation, indicating that the double ITCZ bias is robust in the HRMIP run. This bias is clearly reduced in the MP-LEO2 and MP-LEO2-L78 runs, as much as in the MJO run, and the difference in their precipitation amount from the observation is within one or two standard deviations (Figures 11c–11e). In addition, unlike in the HRMIP run, the abrupt enhancement of precipitation in 15°S–0° during austral summer is captured in the MP-LEO2 and MP-LEO2-L78 runs, although it is overemphasized in the MP-LEO2-L78 run as indicated by significantly active precipitation over the Southern Hemisphere until March (but not associated with a double ITCZ).

The mean radiation flux at the TOA lies between the values in the HRMIP and MJO runs as a result of the revisions to the cloud microphysics and turbulent diffusion. Figure 12a shows the annual-mean OLR bias in the MP-LEO2 run, and Figures 12b and 12c display its difference from that in the MJO and HRMIP run, respectively. Although negative OLR biases are more significant almost globally in the MP-LEO2 run than in the HRMIP run, they are mitigated more than in the MJO run especially in the extratropics, which mainly results from the retuning in the microphysics scheme. In addition, the remaining negative OLR biases are largely reduced by the vertical resolution enhancement. The annual-mean OLR bias in the MP-LEO2-L78 run (Figure 12d) and its comparison with that in the MP-LEO2 run (Figure 12e) suggest that higher vertical resolutions increase OLR values globally

and reduce the large biases over the deep tropics and storm-track regions, where ice frequently condensates. This result is consistent with Seiki et al. (2015). As revealed by analyses of OSR fields (shown later), the increased number of vertical layers have a larger impact on OLR fields than OSR fields.

Figures 12f–12j are the same as Figures 12a–12e but for the annual-mean OSR. The mean OSR values in the MP-LEO2 run decrease (increase) mainly in the tropics compared to the MJO (HRMIP) run, which realizes an OSR distribution that is intermediate between those in the HRMIP and MJO runs (Figures 12f–12h). The positive biases in the tropics due to shortwave reflection by deep clouds are reduced in the MP-LEO2-L78 run (Figures 12i and 12j), corresponding to a decrease in cloud water and ice (not shown). Interestingly, negative OSR biases over the Southern Ocean are slightly mitigated in the MP-LEO2 run, and this improvement is further enhanced by the vertical resolution enhancement. This energetic change can contribute to the disappearance of the double ITCZ structure, which is discussed in Section 6.1.

In Figure 13, the climatological temperature and circulation fields are compared between JRA-55 reanalysis and the sensitivity experiments. Figures 13a and 13b show biases of the annual-mean zonal mean temperature, and zonal mean zonal wind and Eulerian mean meridional mass stream function for the HRMIP run, respectively. In the tropics, warm bias exists in the upper troposphere, which is especially significant around the tropopause (more than +6 K). A reason for this is strong radiative heating associated with the excess of cloud ice that is explicitly generated by RS14-version microphysics and remains present. Related to this warm bias, the simulated tropospheric westerly jets have stronger and/or poleward shift bias (Figure 13b). In addition, the simulated annual-mean Hadley circulation (black contours) has more upward motions in the Southern Hemisphere than in JRA-55, consistent with the zonal mean precipitation and the double ITCZ structure. Furthermore, the cold/warm dipole pattern bias in the extratropical tropopause/lower stratosphere also stands out, which is likely contributed by unrealistic radiative cooling and meridional stratospheric circulations (e.g., Shepherd et al., 2018). Most of these features in the HRMIP run follow the fields in NICAM AMIP-type and/or HighResMIP simulations (Kodama et al., 2015, 2021).

In the MJO run (Figures 13c and 13d), the aforementioned biases in the HRMIP run are reduced, except for the temperature bias at and above the extratropical tropopause. Meanwhile, the smaller warm bias in the tropics compared to that in the HRMIP run is probably rooted in another severe bias; cloud ice is much scarcer when generated by T08-version microphysics (Figures 4d–4f) than by RS14-version microphysics in the HRMIP run and is underestimated in comparison with the observation (Kodama et al., 2021).

This trade-off problem is partly resolved in the MP-LEO2 run: the introduction of cloud ice falling in the RS14-version microphysics scheme can reduce the tropical warm bias, as in the MJO run (Figure 13e), while preserving abundant cloud ice (cf., Figure 8c). In this context, the strong and/or poleward shift bias of the mid-latitude westerly jets is also mitigated in the MP-LEO2 run (Figure 13f). In addition, the anomalous upward motions in the Southern Hemisphere that are associated with the Hadley circulation are weakened, corresponding to the mitigation of the double ITCZ.

The MP-LEO2-L78 run (Figures 13g and 13h) suggests that the vertical resolution enhancement, in addition to the MP-LEO2-run setting, significantly mitigates the biases found in both the upper-troposphere and lowermost-stratosphere temperature fields and mid-latitude westerly jets. A plausible reason for the bias reduction in temperature can be explained as follows: higher vertical resolutions suppress the excessive formation of high clouds (Seiki et al., 2015) and water vapor leakage into the lowermost stratosphere (Shepherd et al., 2018), reducing overestimation of radiative heating (cooling) by tropical cirrus (stratospheric water vapor) and bringing the vertical profile of temperature closer to reality. Furthermore, momentum transport by gravity waves is also expected to be simulated better, which may help the improved representation of the mid-latitude tropospheric jets. This causal relationship should be quantitatively evaluated in future work by examining the dependency of vertical resolutions on momentum budgets.

Note that a strong warm bias and near-surface (1,000–975-hPa) colder layer exist in the Antarctic region for all the experiments (Figures 13a, 13c, 13e, and 13g). This is due mainly to overestimated turbulent mixing by the MYNN2 scheme, which is associated with large vertical wind shear near the surface with steep slopes (not shown). This issue can be related to a limitation of the vertical discretization by the terrain-following coordinate system, which implies that improvement of the dynamical core is also required.

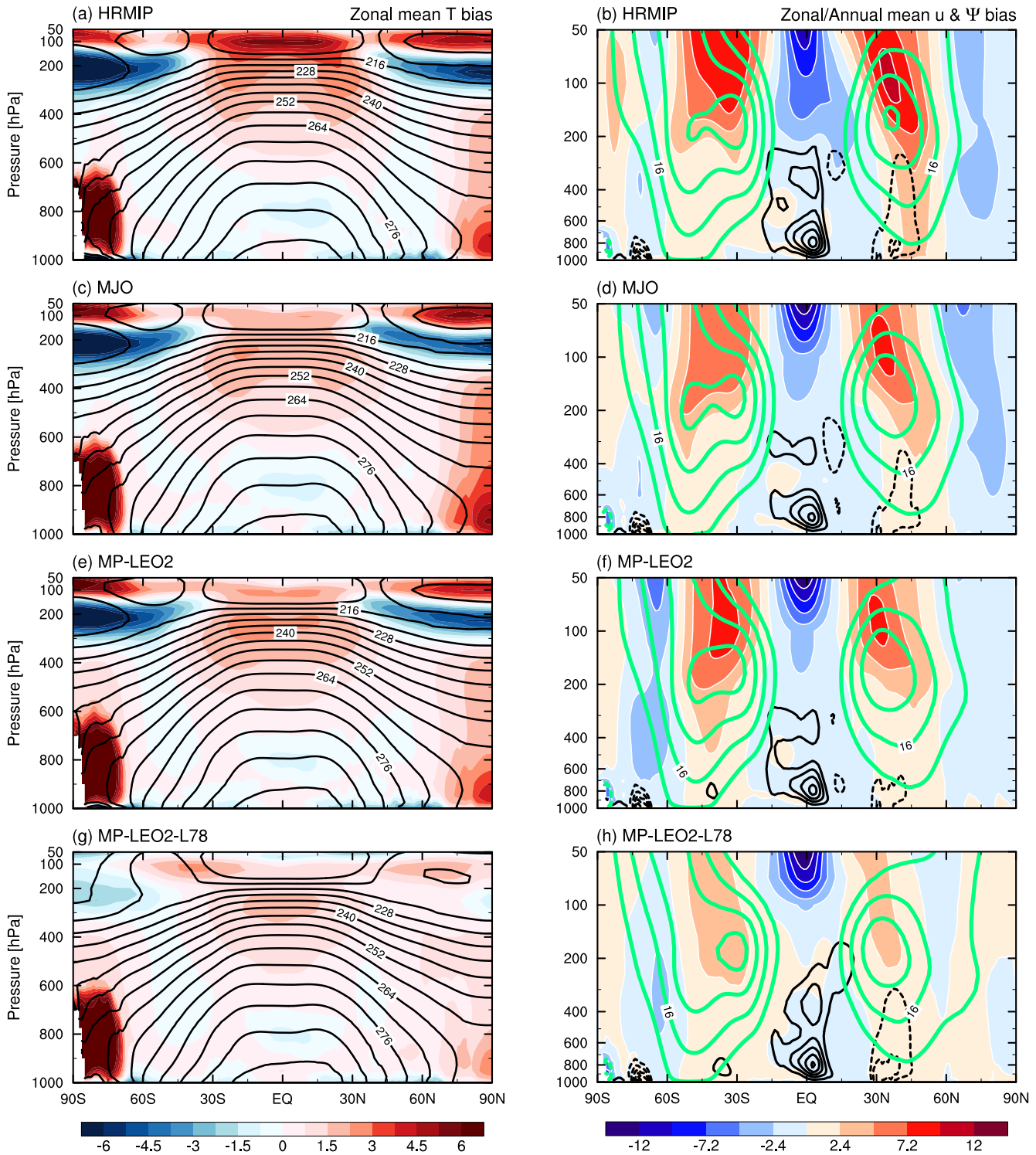

Figure 13. (a) Latitude-height section of the annual-mean zonal mean temperature (contours) and its bias against JRA-55 reanalysis (shading; K) for the HRMIP run. Contour interval is 6 K. (b) As in (a), but for the annual-mean zonal mean zonal wind (green contours), its bias (shading; m s^{-1}), and Eulerian mean mass stream function bias (black contours). Green and black contour interval is 8 m s^{-1} and 1.0×10^{-12} kg s^{-1}, respectively, with negative (zero) contours dashed (omitted). Positive contours indicate the clockwise circulations. (c–h) The same as (a and b), but for the (c and d) MJO, (e and f) MP-LEO2, and (g and h) MP-LEO2-L78 runs.

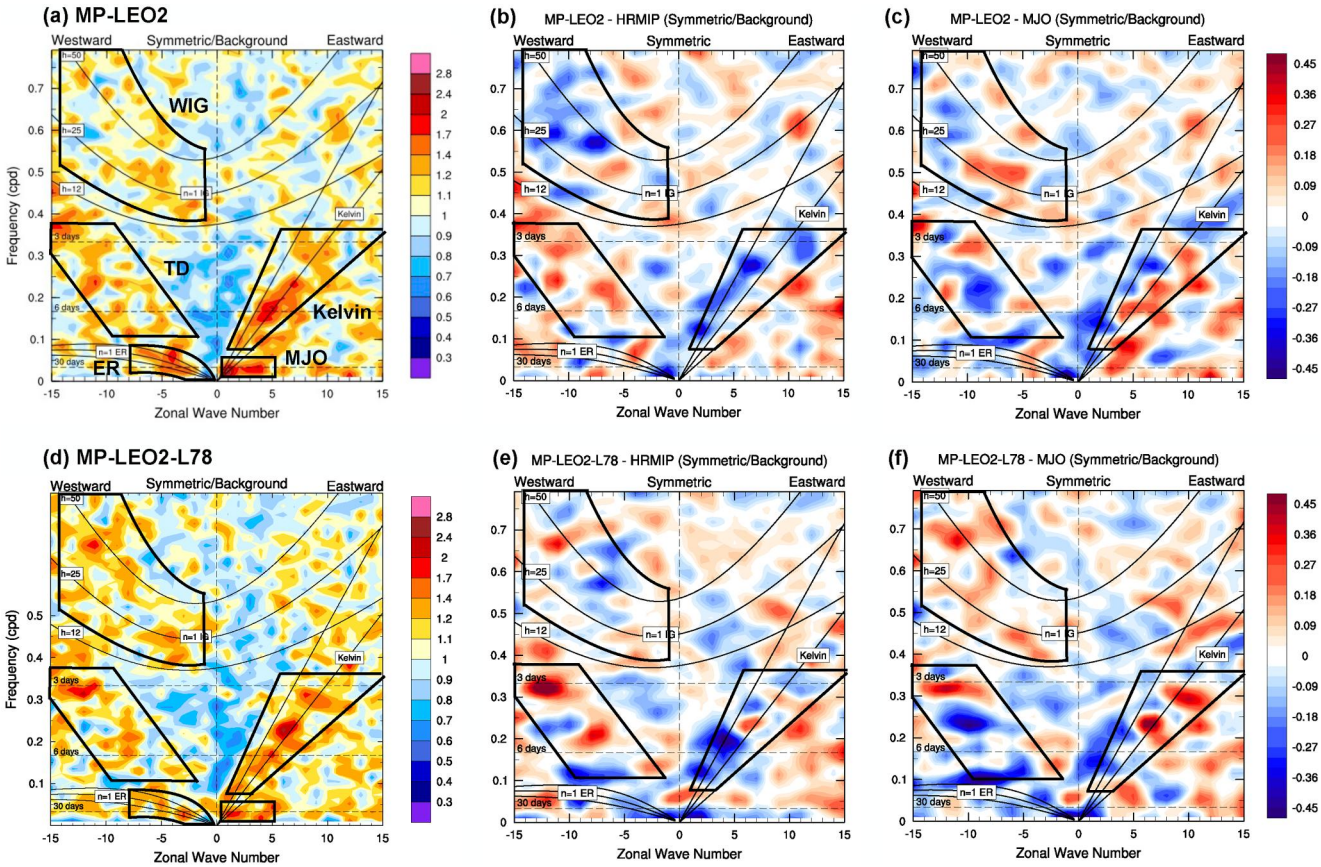

Figure 14. (a) The same as Figures 7b and 7c, but for the MP-LEO2 run. (b and c) As in (a), but for its difference from the (b) HRMIP and (c) MJO runs. (d–f) The same as (a–c), but for the MP-LEO2-L78 run.

5.2. Weather Disturbances

In this subsection, we focus on various kinds of daily-to-seasonal-scale phenomena. First, to grasp the behaviors of typical modes in tropical deep convection, we compare the representation of convectively coupled equatorial waves and the MJO. We then examine several large- and S2S-scale variabilities such as the Asian summer monsoon and boreal-summer MJO. TC activities (e.g., genesis, intensity), which are affected by S2S-scale environmental factors, are also evaluated. Lastly, we analyze the precipitation diurnal cycle as a fundamental convective mode in the tropics.

5.2.1. Convectively Coupled Equatorial Waves and the Boreal-Winter MJO

Figure 14a shows normalized wavenumber-frequency power spectra in the equatorially symmetric component of OLR (15°S–15°N) in the MP-LEO2 run, and Figures 14b and 14c present its difference from the HRMIP and MJO runs, respectively. For the equatorial OLR simulated in the MP-LEO2 run, there are prominent peaks in the representative wave modes including the MJO, and the spectral peaks for Kelvin waves and the MJO are well separated from each other, as in the observation (Wheeler & Kiladis, 1999) (Figure 14a). These spectral characteristics are a good mixture of those in the HRMIP and MJO runs; the Kelvin and inertia-gravity waves tend to decay (be amplified) compared to those in the HRMIP (MJO) run, and vice versa for the TD-type disturbances and equatorial Rossby waves (Figures 14b and 14c). This is probably a result of the moisture–convection relationship being intermediate between the HRMIP and MJO runs. Hence, the MP-LEO2 run can simulate both the gravity-wave and rotational type modes reasonably well.

Figures 14d–14f are the same as Figures 14a–14c but for the MP-LEO2-L78 run. They indicate that the vertical resolution enhancement not only achieves the improvement found in the MP-LEO2 run but also enhances the

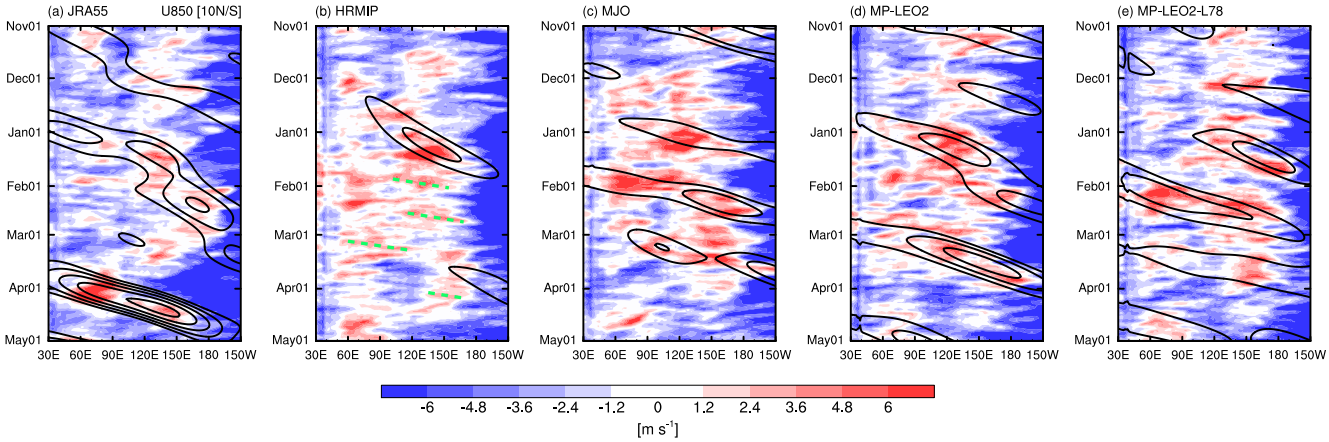

Figure 15. Time-longitude diagrams of 850-hPa zonal winds (shading) and MJO-filtered westerly anomalies (contours) averaged in 10°S–10°N for the (a) JRA-55 reanalysis and (b) HRMIP, (c) MJO, (d) MP-LEO2, and (e) MP-LEO2-L78 runs. Contours start with 0.5 and 1.0 m s^{-1} for (a and e) and (b–d), respectively, and contour interval is 1 m s^{-1}. Green dashed lines in (b) indicate Kelvin-wave signals.

activity of inertia-gravity waves (Figures 14a and 14d), which is closer to the observation. Thus, a higher number of vertical layers contributes to the realistic representation of high-frequency gravity waves while keeping positive results obtained from the MP-LEO2 physics.

In Figure 15, we compare the time-longitude diagrams of equatorial 850-hPa zonal winds during boreal winter, when the mean MJO activities are enhanced (Zhang & Dong, 2004), between the JRA-55 reanalysis and the HRMIP, MJO, MP-LEO2, and MP-LEO2-L78 runs. For clarity, MJO-filtered westerly anomalies (eastward wavenumbers 1–5 and periods of 30–120 days) are also plotted with black contours. Note that because the boreal winter in these simulations is far from the initial date (1 June 2004), the simulated MJO in this period is not a result of initial value problems but an internal mode of the model. For the reanalysis, MJO-scale westerlies propagate eastward quasi-periodically during this period (Figure 15a). This MJO propagation cannot be captured well in the HRMIP run (Figure 15b), in which high-frequency eastward-propagating signals like Kelvin waves are more evident (green lines). This may be related to faster moisture convective adjustment in the HRMIP run and the resulting unfavorableness of the rotational moisture-coupled modes that are an important element of the MJO (Adames et al., 2019; Yasunaga & Mapes, 2012), as briefly discussed in the interpretation of Figure 7. In contrast, the MJO run shows robust eastward propagation of organized westerly areas into the dateline, although the simulated westerlies are more conspicuous than in the reanalysis (Figure 15c). In the MP-LEO2 run, the overestimation of westerlies found in the MJO run is somewhat mitigated, and the quasi-periodic westerly/easterly phase changes associated with the MJO propagation are spontaneously reproduced (Figure 15d), which also holds true in the MP-LEO2-L78 run (Figure 15e). This result suggests that the MP-LEO2-based model physics can simulate a realistic MJO mode in climate simulations at a comparable level to S2S-scale simulations, unlike most conventional GCMs that struggle with spontaneous and frequent MJO realization (Ling et al., 2017).

5.2.2. Asian Summer Monsoon and the Boreal-Summer MJO

In boreal summer, the ocean-land contrast largely drives the large-scale circulations over the Indo-Pacific warm pool, the Asian summer monsoon. Reproducibility of the Asian summer monsoon is an important aspect in seamless modeling, because it has a significant impact on the representation of smaller-scale phenomena such as TCs (e.g., Ritchie & Holland, 1997; Yamada et al., 2019; Yoshida & Ishikawa, 2013), which are expected to be captured well in k-scale simulations. Here we compare how the simulated Asian summer monsoon changes depending on the model settings.

Figures 16a and 16b show the precipitation and 850-hPa wind distributions averaged from June to September (JJAS) for the JRA-55/TRMM-3B42 and the HRMIP run, respectively. As inferred from the annual-mean precipitation (Figure 5b), the HRMIP run suffers from excess precipitation over the Indian Ocean and the resultant

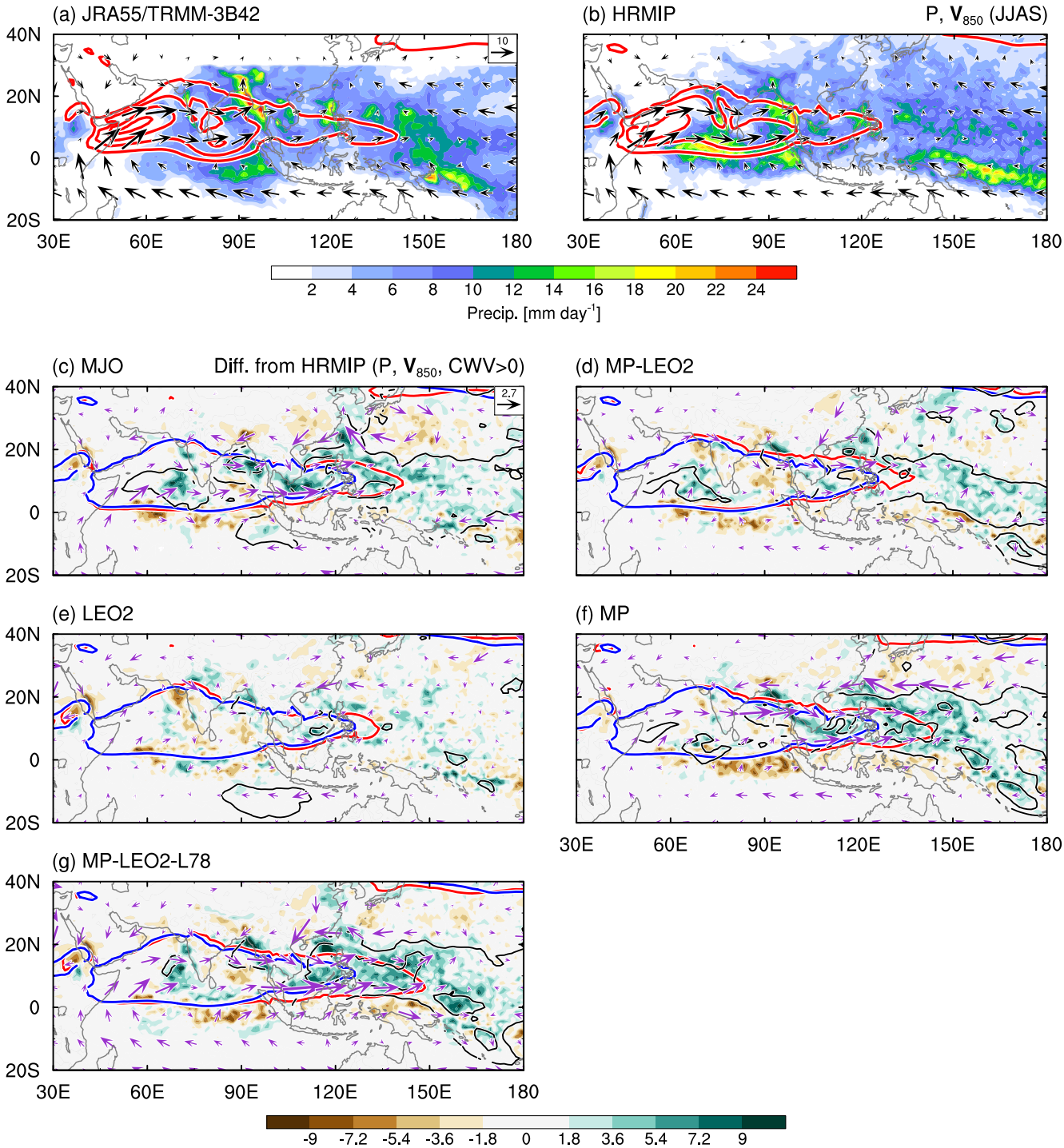

Figure 16. (a and b) Horizontal maps of precipitation (shading) and 850-hPa horizontal and zonal winds (vectors and contours; m s^{-1}) averaged from June to September (JJAS) for the (a) JRA-55 reanalysis and TRMM-3B42 rainfall product and (b) HRMIP run. Contour interval is 4 m s^{-1}, with negative and zero contours omitted. (c–g) As in (a and b), but for the difference of precipitation (shading), 850-hPa horizontal winds (vectors), and column-integrated water vapor (black contours) from the HRMIP run for the (c) MJO, (d) MP-LEO2, (e) LEO2, (f) MP, and (g) MP-LEO2-L78 runs. Contours for zonal wind velocities of 4 m s^{-1} are also plotted for the HRMIP (blue) and each run (red). Black contour interval is 2.5 kg m^{-2}, with negative and zero contours omitted.

misrepresentation of the zonal contrast of precipitation in the Indo-Pacific region. Related to this, the simulated monsoonal westerlies stemming from the Somali jet barely extend beyond the Philippines into the western Pacific.

The bias in the HRMIP run is reduced in several sensitivity experiments. Figures 16c–16g present the difference in precipitation, 850-hPa winds, and column-integrated water vapor during JJAS between the HRMIP run and other runs. In both the MJO and MP-LEO2 runs (Figures 16c and 16d), the western Pacific region has more water vapor and precipitation, and the monsoonal flows including the Somali jet become stronger and blow into the western Pacific, although the extent of this improvement is smaller for the MP-LEO2 run. By decomposing the updates of turbulent diffusion and cloud microphysics in the LEO2 and MP runs (Figures 16e and 16f), we find that microphysics retuning dominates the better representation of the Asian summer monsoon. Interestingly, a comparison of the MP-LEO2 and MP runs suggests that turbulent diffusion in the MP-LEO2 run weakens the extension of the monsoon, contrary to the result in the LEO2 run. Although such local differences might be related to the chaotic nature of weather, because our analysis covers only a single season, this nonlinear behavior likely comes from the difference in precipitation depending on microphysics settings. One possible interpretation is that because the lack of precipitation over the western Pacific in the HRMIP run is resolved in the MP run, turbulent diffusion added in the MP run works to mitigate abundant precipitation in this region (as described in Section 4.2). In Figure 16g, the results of the MP-LEO2-L78 run suggest that the vertical resolution enhancement can further promote the bias reduction associated with the two model updates in the MP-LEO2 run, leading to the most realistic features.

In addition to the Asian summer monsoon, the boreal-summer MJO (or Boreal Summer Intraseasonal Oscillation; BSISO) (Kikuchi, 2021; Yasunari, 1979), which is characterized by the north-eastward propagation of large-scale convection in the Indo-Pacific region, is important to the weather change. To evaluate our skill in simulating it, we present the time-latitude diagrams of OLR averaged over the western Pacific (130°–150°E) for the observation (Figure 17a) and sensitivity experiments (Figures 17b–17d). In Figure 17a, there are two major northward-propagating convective envelopes observed in June and in mid-July to August, corresponding to the BSISO activity. In accordance with this large-scale convective evolution, many TCs are generated over the western North Pacific (denoted by red crosses), consistent with the fact that the active phase of the BSISO strongly promotes TC genesis (e.g., Liebmann et al., 1994; Nakazawa, 1986; Yoshida et al., 2014). In the HRMIP run, these features of the observation are not reproduced well, especially for the second BSISO event (Figure 17b): large-scale convective organization is weaker, and the convective systems appear to stagnate around 10°N rather than propagate northward in July and August. The weak amplitudes and/or stalling of the BSISO in previous NICAM simulations have been pointed out in the several studies (Kikuchi et al., 2017; Nakano & Kikuchi, 2019; Shibuya et al., 2021).

This pre-existing bias is largely mitigated in the MP-LEO2 run (Figure 17d): the northward-propagating, well-organized convective envelopes of the two BSISO events and associated TC genesis are reasonably well simulated, despite some overestimation of convective activities in early July. This result is as good as in the MJO run (Figure 17c) tuned for S2S-scale MJO simulations, which means that the MP-LEO2-based physics are applicable to initial value problems as well as to climate simulations.

As expected, the MP-LEO2-L78 (Figure 17e) run shares the positive aspects of the MP-LEO2 run such as active TC genesis at the northern edge of BSISO convective envelopes. Also, it captures a more realistic time scale of the northward propagation of the second BSISO event mainly in August. Such improvement of BSISO simulations is robustly confirmed by other ensemble simulations using this updated NICAM (not shown), and it may be related to the better representation of the background Asian summer monsoon. This topic should be scrutinized in the future.

5.2.3. Tropical Cyclone Activities

Here we evaluate the TC activities simulated in the sensitivity experiments by comparing them with the observational best-track data sets. TCs are detected following the method by Nakano et al. (2015); after detecting local minima of sea-level pressure (SLP) as TC candidates, we track them by imposing some criteria for 10-m, 850-hPa and 200-hPa wind speeds, the sum of 700-, 500-, and 300-hPa temperature anomalies, and the 850-hPa maximum relative vorticity. If a TC candidate satisfies all the criteria over a period of at least 36 hr, it is formally assigned as a TC.

First, the simulated TC genesis and tracks are evaluated. Figure 18 shows the TC genesis points and distributions of the number of TCs passing through each 2.5° × 2.5° grid box for the observation and sensitivity experiments. In

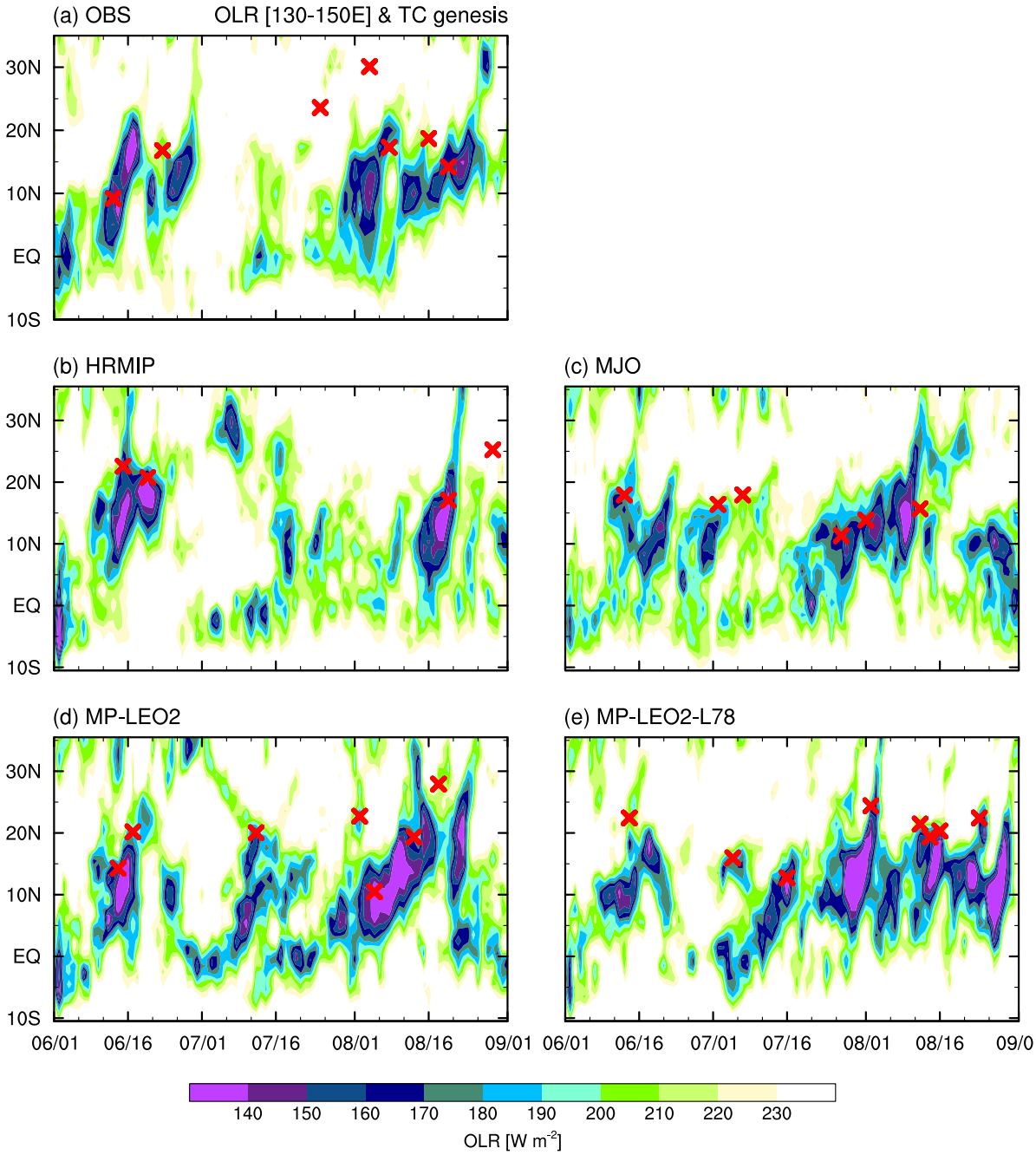

Figure 17. Time-latitude diagrams of OLR averaged in 130°–150°E (shading) and tropical cyclone genesis points within that longitudinal band (red cross) for the (a) observation and (b) HRMIP, (c) MJO, (d) MP-LEO2, and (e) MP-LEO2-L78 runs.

Table 2, the total number of TCs generated in each basin is also presented. In the HRMIP run, the number of TCs generated over the eastern Pacific and Indian Ocean is relatively well simulated, whereas TC genesis activities have several biases especially over the western and central Pacific region (Figures 18a and 18b). Over the western North Pacific, the TC genesis and the subsequent passage of TCs occur much less frequently, and TCs generated over the eastern Pacific tend to move more westward across the dateline. These biases are removed in the MJO run (Figure 18c); however, the total number of TCs greatly increases and TC activities are overemphasized compared to the observation, especially over the South Pacific (see also Table 2).

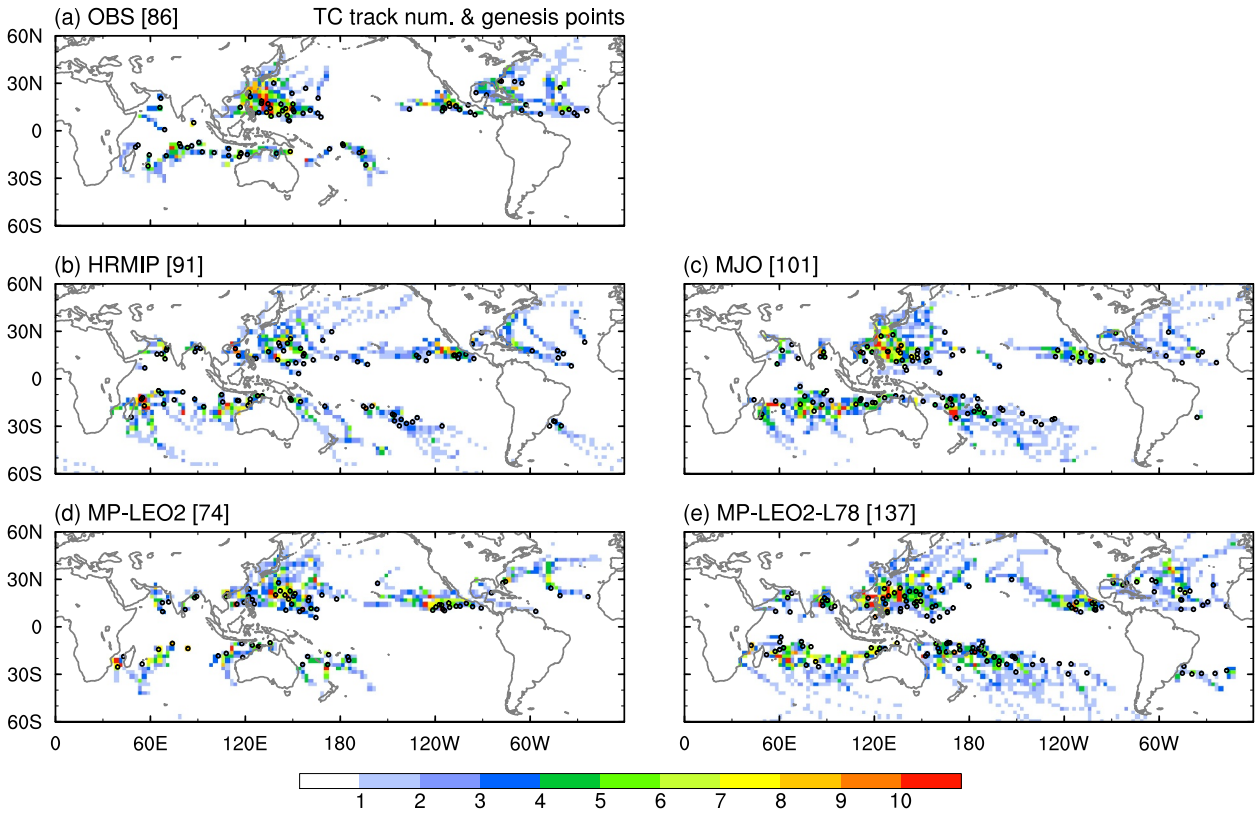

Figure 18. Horizontal distributions of tropical cyclone genesis points (open circle) and the number of TCs passing through each 2.5° × 2.5° grid box (shading) for the (a) observation and (b) HRMIP, (c) MJO, (d) MP-LEO2, and (e) MP-LEO2-L78 runs. The total number of TCs simulated in each 1-year simulation is denoted at the upper-left corner of figures.

The MP-LEO2 run also follows the bias reduction found in the MJO run (Figure 18d). Looking at the western North Pacific, TC genesis and tracks are well organized around 150°E, although they are slightly to the east of the observed and MJO-run genesis points and tracks. Also, the number of TCs is comparable to the observation (Table 2). These improvements are consistent with the eastward extension of the Asian summer monsoon into the western Pacific (Figure 16d) and enhanced BSISO activities (Figure 17d). This is because TC genesis over the western North Pacific is supported by the monsoon trough with large-scale wind confluence and convergence and plentiful moisture (e.g., Ritchie & Holland, 1997; Yamada et al., 2019; Yoshida & Ishikawa, 2013), and it is facilitated by positive relative vorticity and water vapor anomalies during the BSISO-active phase (Kikuchi, 2021, and references therein). Furthermore, the overestimation of TC genesis in the South Pacific in the HRMIP and MJO runs is largely removed. However, there appears to be another bias: more and fewer TCs are simulated in the eastern Pacific and Atlantic, respectively.

Table 2
Total Number of Tropical Cyclones Generated in Each Basin for the Observation (IBTrACS) and HRMIP, MJO, MP-LEO2, and MP-LEO2-L78 Runs

Run name	NI	WP	EP	NA	SI	SP	SA
IBTrACS	4	29	12	15	18	8	0
HRMIP	9	22	12	8	20	16	4
MJO	7	28	10	8	23	24	1
MP-LEO2	6	27	14	7	13	7	0
MP-LEO2-L78	11	33	13	18	19	37	6

Note. The targeted basins are the North Indian Ocean (NI), western North Pacific (WP), eastern North Pacific (EP), North Atlantic (NA), South Indian Ocean (SI), South Pacific (SP), and South Atlantic (SA).

In Figure 18e, the vertical resolution enhancement in the MP-LEO2-L78 run appears to mitigate biases found in the MP-LEO2 run, except for much more TC genesis over the South Pacific, which can be associated with enhanced convective activities there during boreal winter (cf., Figure 11e). The eastward displacement of TC genesis over the western North Pacific in the MP-LEO2 run is modified, leading to the realistic maximum number of TC tracks just to the east of the Philippines and south of Japan. In addition, TC track density over the eastern Pacific and Atlantic is reduced and increased, respectively, which becomes closer to the observation even despite the overestimation in the eastern Pacific. These responses over the western and eastern Pacific are also confirmed

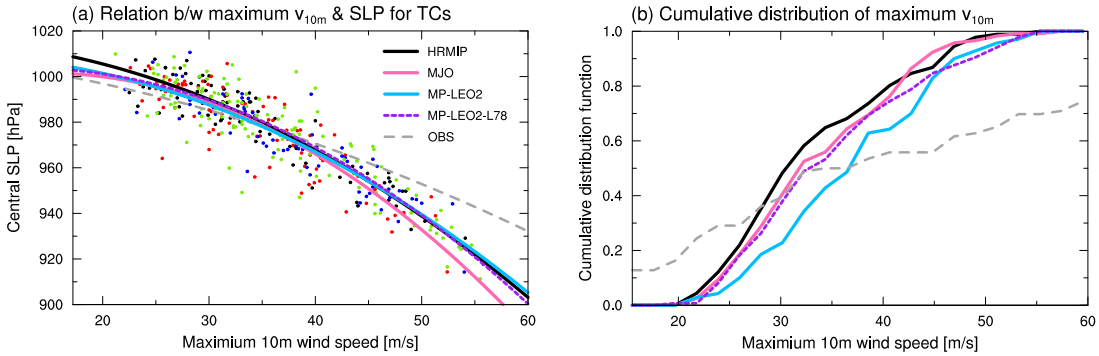

Figure 19. (a) Scatter diagram of the central sea-level pressure versus the lifetime maximum 10-m wind speed for tropical cyclones simulated by the HRMIP (black dots and lines), MJO (red dots and pink lines), MP-LEO2 (blue dots and sky-blue lines), and MP-LEO2-L78 runs (green dots and dashed purple lines). Lines are the second-order polynomial fit to the data points, and the gray dashed line is for the observation. (b) Cumulative distribution of the lifetime maximum 10-m wind speed for the observation (gray dashed) and HRMIP (black), MJO (pink), MP-LEO2 (sky-blue), and MP-LEO2-L78 runs (dashed purple). The data are binned by the interval of 2 m s^{-1}.

in other NICAM simulations with a configuration like that used in the MP-LEO2-L78 run (not using the Leonard term) for multi-year JJAS seasons (not shown), thereby supporting the robustness of our model improvement.

One caveat is that the MP-LEO2-L78 run generates many more TCs globally than all the other experiments, which is possibly related to the decreased static stability associated with a reduction of high temperature bias in the upper troposphere (see Figure 13g). Note that the absolute number of TCs is tunable by changing the parameters used to detect TCs. This means that there is room for trying another parameter set for TC detection in the MP-LEO2-L78 run, in which the environmental temperature field is significantly different from that in the other runs.

The simulated TC intensity is also analyzed, with the caveat that the sample sizes are insufficient. Figure 19a shows a scatter plot of the central SLP and maximum sustained 10-m wind speeds. Note that the central SLP and 10-m wind speeds are instantaneous (6-hourly) values and are specified on the native grid. As already confirmed by Yamada et al. (2017), the maximum wind speed for intense (weak) TCs is underestimated (overestimated) in all the sensitivity experiments compared to the observation. Interestingly, the underestimation of wind speeds except for weak TCs is more prominent in the MJO run, consistent with the case study of TC genesis in the 3.5-km mesh simulation (Nasuno et al., 2016). This is possibly because a tight vortex structure with a large pressure gradient may not be preferred by the weaker lower-tropospheric latent heating (see Figure 8c), which can hinder the intense convective development that contributes to concentrated vortex stretching. Although the model improvement in the MP-LEO2 and MP-LEO2-L78 runs has few impacts on the pressure–wind relationship, at least in this study, the vertical resolution enhancement seems to be able to simulate more intense TCs, as indicated by more TCs with maximum wind speeds exceeding 45 m s^{-1} (see also Figure 19b). This change can be attributed to the improvement in the diagnosis of surface winds and resultant surface heat fluxes, which are important to TC development, as a result of the lowest vertical level being closer to the ground in the MP-LEO2-L78 run. In fact, similar results are obtained in another NICAM simulation with a thinner lowest layer (not shown).

Figure 19b shows the cumulative distribution of the lifetime maximum 10-m wind speeds. A common bias in the simulations is that the numbers of both weak and intense TCs are much smaller, and instead, TCs with moderate intensity are actively generated. Among the sensitivity experiments, the MP-LEO2 run tends to generate TCs that can develop to stronger intensity than those generated in the HRMIP and MJO runs, which emphasizes the bias of few weak TCs more. The vertical resolution enhancement (the MP-LEO2-L78 run) can suppress this tendency, as well as preserving the feature in the MP-LEO2 run of more TCs with strong intensity (e.g., more than 45 m s^{-1}), which tends to become slightly closer to the observation. Although determining the physical reasons for the dependency of the GCRM settings on TC intensity is beyond the scope of this study, it is an interesting topic that should be addressed in future.

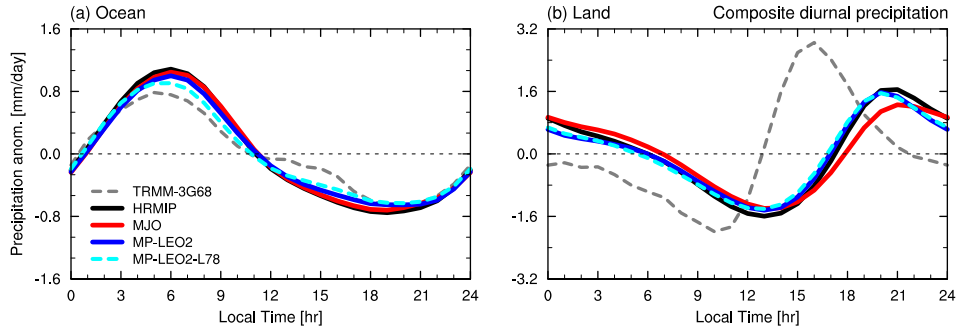

Figure 20. Composite diurnal cycle of 1-hourly precipitation intensity anomaly averaged in 15°S–15°N over (a) ocean and (b) land for the TRMM-3G68 climatology (gray dashed), and HRMIP (black), MJO (red), MP-LEO2 (blue), and MP-LEO2-L78 runs (cyan dashed).

5.2.4. Tropical Precipitation Diurnal Cycle

First, the mean phase and amplitude of the simulated diurnal cycle of precipitation in the tropics are analyzed. Figures 20a and 20b show the composite diurnal cycle of observed and simulated precipitation in 15°S–15°N over ocean and land, respectively. Over ocean, the peak time of simulated precipitation is 06:00 local time (LT) for all the experiments, which is slightly later than the peak time in the TRMM-3G68 climatology (05:00 LT). The differences in amplitude among the sensitivity experiments are small, but the model updates for the MP-LEO2 run and vertical resolution enhancement appear to weaken the diurnal variations. This change corresponds to slight bias reduction, considering that NICAM tends to overestimate amplitude of diurnal precipitation over open ocean (Noda et al., 2012; Sato et al., 2009).

Over land areas, a systematic bias of the phase of the diurnal cycle is evident regardless of model settings in the 14-km mesh simulations (Figure 20b), consistent with Sato et al. (2009). While the TRMM-3G68 climatology indicates afternoon peak at 16:00 LT, the peak for the simulations occurs around 20:00–21:00 LT; that is, about 5 hr later than the observation. In addition, the timing of the precipitation minimum for the simulations (13:00–14:00 LT) lags behind that for the observation (10:00 LT). The larger phase difference over land than over ocean suggests that the daytime convection over land, which is characterized by the sub-daily-scale and O(1–10)-km-scale shallow-to-deep transition, cannot be captured accurately at 14-km resolution because of the unsatisfactory representation of shallow moistening mainly at those scales. This notion is supported by the findings that the phase delay is slightly pronounced in the MJO run with convection less prone to triggering (cf., Figure 3b), and that this delayed convection triggering bias is drastically reduced in a simulation at 3.5-km resolution (Figure A1 in Appendix A) or with parameterized shallow convection (Argüeso et al., 2020).

Another aspect of the tropical precipitation diurnal cycle is the offshore migration of rainfall systems in coastal areas (e.g., Houze et al., 1981; Ichikawa & Yasunari, 2006). As an example of this, we focus on the phenomenon observed around Sumatra Island, where the precipitation peak emerges near the western coast of the island in the early evening and then migrates away from the coast during nighttime and early morning (e.g., Mori et al., 2004; Yokoi et al., 2017). Figure 21 shows the composite time series of the observed and simulated diurnal precipitation variations along the orthogonal direction to the western coastline of Sumatra Island. The nighttime offshore migration of precipitation can be captured in all the simulations (Figures 21b–21e), whereas there is a common bias of the delayed onset of precipitation on the coastal land in comparison with the observation (Figure 21a). The degree of this late precipitation onset is different among the sensitivity experiments: the onset (with precipitation more than 10.5 mm day^{-1}) is most delayed in the MJO run (19:00 LT; Figure 21c), and closest to the observation in the MP-LEO2-L78 run (17:00 LT; Figure 21e). A tendency similar to that in the MJO run was also confirmed in Nasuno (2021), who examined the 7-km mesh simulation of diurnal convection in the Maritime Continent. The better performance in the MP-LEO2-L78 run is probably because more vertical layers in the PBL can improve the representation of convection triggering.

The amplitude of offshore migrating precipitation largely depends on the model settings. Comparison of the MP-LEO2-L78 run and the other three runs shows that its dependency is different from that of the diurnal cycle over open ocean (Figure 20a). This feature may be explained by some mechanisms of nighttime offshore

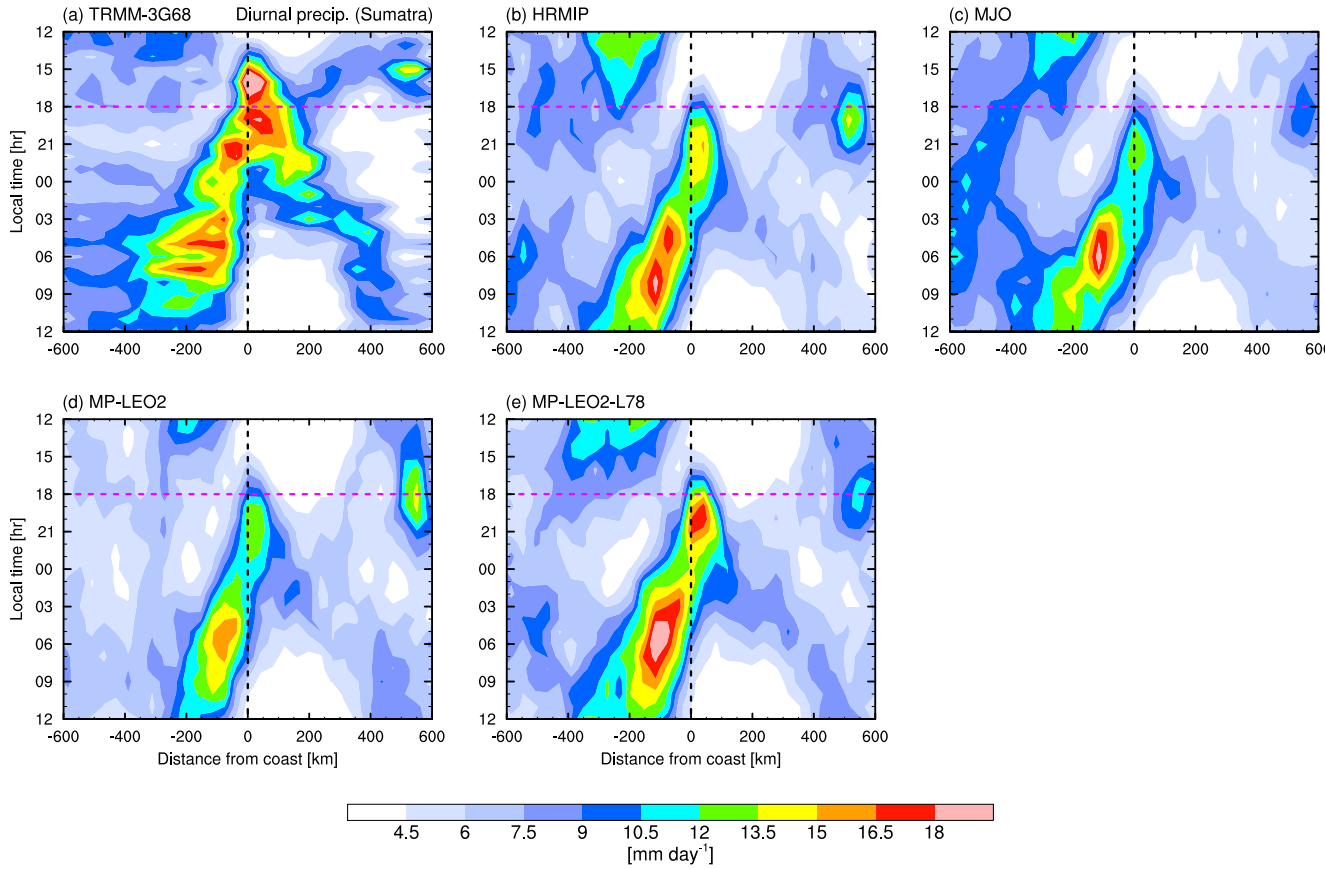

Figure 21. Composite time series of 1-hourly precipitation as a function of distance from the western coastline of Sumatra Island for the (a) TRMM-3G68 climatology, (b) HRMIP, (c) MJO, (d) MP-LEO2, and (e) MP-LEO2-L78 runs. Negative values of distance correspond to the offshore direction. Magenta dashed lines indicate the reference local time (18:00 LT) for comparisons.

migration, such as preconditioning by gravity waves (e.g., Love et al., 2011; Yokoi et al., 2017) and/or gravity currents associated with land breeze, cold pools, and environmental flows (e.g., Houze et al., 1981; Mori et al., 2004). In fact, it is expected that the vertical resolution enhancement can simulate gravity waves and low-level flow interactions better, consistent with the most significant offshore migration in the MP-LEO2-L78 run (Figure 21e). In future work, it would be worth further examining the detailed mechanisms of these processes.

One implication of these findings is that even if the representation of the diurnal cycle has several inherent systematic biases at 14-km resolution, these errors seem not to critically affect the fundamental simulation of synoptic-to-large-scale behaviors (cf., Segura et al., 2022), as inferred from all the analyses described in Section 5. A possible reason for this is that those scales are sufficiently distinct from the kilometer-/sub-daily scales responsible for the diurnal cycle. In that sense, we may say that there are some degrees of freedom for obtaining the skeleton of the synoptic-to-large-scale variabilities. Nevertheless, the seamless representation of sub-daily-to-climatological features is obviously necessary to describe higher-order variations embedded within a given scale. A better understanding of the scale separation and interaction would be helped by k-scale climate simulations.

6. Discussion

In this section, we discuss an interpretation of why our model updates can improve the representation of the ITCZ and MJO, which are remarkable examples of the climatological mean states and weather disturbances, respectively.

6.1. Relationship Between the ITCZ and Interhemispheric Energetics

Recent studies have pointed out that the ITCZ structure is determined by the cross-equatorial energy transport and atmospheric energy budget (e.g., Adam et al., 2016; Bischoff & Schneider, 2016; Hwang & Frierson, 2013). Following this idea, we present a possible reason for the mitigation of the double ITCZ bias in NICAM. A starting point is the zonal mean column-integrated moist static energy (MSE) balance:

$$\begin{aligned}\frac{\partial}{\partial y}\langle\overline{vh}\rangle &= \overline{\langle SW\rangle} + \overline{\langle LW\rangle} + \overline{SH} + \overline{LH} \\ &= \left(\overline{SW^{net\downarrow}} - \overline{LW^{net\uparrow}}\right)_{\mathrm{TOA}} + \underbrace{\left(\overline{SW^{net\uparrow}} + \overline{LW^{net\uparrow}}\right)_{\mathrm{SFC}} + \overline{SH} + \overline{LH}}_{SEI}\end{aligned} \tag{6}$$

where v is meridional wind; h is MSE; SW and LW are shortwave and longwave radiative flux, respectively; SH and LH are surface sensible and latent heat flux, respectively; angle brackets and overbars denote the mass-weighted column integration and zonal mean, respectively; and subscripts "$net\downarrow$" and "$net\uparrow$" denote net downward and upward flux, respectively. If Equation 6 is latitudinally integrated over each of the Southern and Northern Hemispheres, and we use the boundary condition that the meridional MSE flux must be zero at the poles, we obtain

$$\int_{\mathrm{SP}}^{\mathrm{EQ}} \frac{\partial}{\partial y}\langle\overline{vh}\rangle\, dy = \int_{\mathrm{SP}}^{\mathrm{EQ}} NEI\, dy = \langle\overline{vh}\rangle|_{\mathrm{EQ}}$$
$$\int_{\mathrm{EQ}}^{\mathrm{NP}} \frac{\partial}{\partial y}\langle\overline{vh}\rangle\, dy = \int_{\mathrm{EQ}}^{\mathrm{NP}} NEI\, dy = -\langle\overline{vh}\rangle|_{\mathrm{EQ}}$$

where EQ, SP, and NP denote the y-coordinate at the equator, South Pole, and North Pole, respectively; and NEI represents the atmospheric net energy input defined as the sum of terms on the right hand side of Equation 6. Thus, we can calculate the cross-equatorial energy transport as

$$\langle\overline{vh}\rangle|_{\mathrm{EQ}} = \frac{1}{2}\left(\int_{\mathrm{SP}}^{\mathrm{EQ}} NEI\, dy - \int_{\mathrm{EQ}}^{\mathrm{NP}} NEI\, dy\right) \tag{7}$$

This means that in the steady state, atmospheric energy imbalances between the Southern and Northern hemispheres must be balanced by the cross-equatorial MSE flux.

We expect that the ITCZ observed at 8°N is related to the cross-equatorial energy transport into the Southern Hemisphere, and that this southward energy transport is counteracted by the double ITCZ structure. First, to confirm whether this correspondence is valid in the NICAM simulations, we examine the relationship between the ITCZ and annual-mean meridional energy fluxes at the equator. As an index explaining the ITCZ structure, the tropical precipitation asymmetry index A_p (Hwang & Frierson, 2013), which quantifies how antisymmetric the tropical precipitation distributions are hemispherically, is introduced:

$$A_p = \frac{\overline{P}_{0°-30°\mathrm{N}} - \overline{P}_{30°\mathrm{S}-0°}}{\overline{P}_{30°\mathrm{S}-30°\mathrm{N}}} \tag{8}$$

where $\overline{P}_{\phi_1-\phi_2}$ denotes the zonal mean precipitation averaged over the latitudinal band between ϕ_1 and ϕ_2. Figure 22a shows a scatter plot of the meridional MSE flux at the equator and A_p among the sensitivity experiments. This plot shows a clear negative correlation between the two, indicating that more cross-equatorial southward energy transport corresponds to the more hemispherical asymmetry of tropical precipitation (i.e., the single ITCZ). This suggests that it is possible to explain the improvement in the NICAM simulation of the ITCZ precipitation in terms of interhemispheric energetics based on Equation 6.

To reveal what factor changes the cross-equatorial energy transport and in turn leads to the better ITCZ representation, we compare the distributions of the NEI among the HRMIP, MJO, and MP-LEO2 runs. Note that the

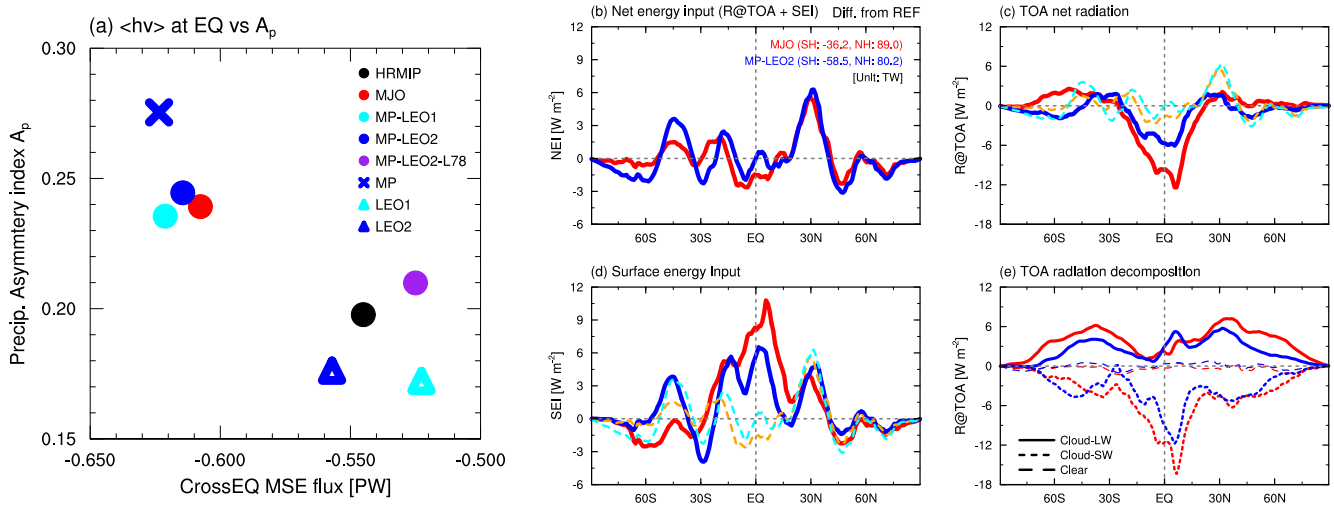

Figure 22. (a) Scatter diagram of the column-integrated cross-equatorial moist static energy fluxes at the equator versus the precipitation asymmetry index (A_p) for all the sensitivity experiments. (b–d) Meridional distributions of the differences of the annual-mean zonal mean (b) net energy input (NEI), (c) net radiative fluxes at the TOA, and (d) surface energy input for the MJO (red) and MP-LEO2 (blue) runs from the HRMIP run. Zonal mean values are weighted by cosine of the latitude. In (b), NEI values integrated over the Southern and Northern Hemisphere are denoted at the upper-right corner of the figure (unit: TW). Dashed lines in (c and d) represent NEI for the MJO (orange) and MP-LEO2 runs (cyan). Positive and negative values indicate the input into and output from the atmosphere, respectively. (e) As in (b–d), but for the decomposition of net radiative fluxes at the TOA; longwave and shortwave cloud radiative forcing (solid and short dashed, respectively), and clear-sky component (long dashed).

MP-LEO2-L78 run, which also mitigates the double ITCZ structure according to Figure 11e, is not examined here; as a first step, it is important to determine a reason for the more robust relationship between the energy transport and the mitigation of double ITCZ in the MP-LEO2 run. Figure 22b shows the difference in the annual-mean zonal mean (solid line) and hemispherically integrated NEI (denoted at the upper-right corner) between the HRMIP and MJO or MP-LEO2 runs. In both the MJO and MP-LEO2 runs, the NEI integrated over the Southern and Northern Hemisphere decreases and increases compared to the HRMIP run, respectively. The $\langle \overline{vh} \rangle$ difference from the HRMIP run, which is calculated from this interhemispheric NEI contrast (shown in Figure 22b) using Equation 7, is −0.0626 PW and −0.0694 PW for the MJO and MP-LEO2 runs, respectively, so cross-equatorial southward energy transport is slightly more pronounced in the MP-LEO2 run. This is consistent with the degree of mitigation of the double ITCZ structure (Figure 22a).

Detailed comparisons of NEI in Figure 22b indicate that, in the MJO (MP-LEO2) run, the lower and higher NEI integration over the Southern and Northern Hemisphere occur mainly in the tropics (the Southern Ocean) and around 30°N, respectively. To examine what contributes to this feature, we decompose the NEI into two components: the net radiative fluxes at the TOA and surface energy input (SEI in Equation 6), as shown in Figures 22c and 22d, respectively. This decomposition suggests that the increased NEI around 30°N is caused by the enhanced SEI in both runs. Considering that the TOA radiation decomposition (Figure 22e) reveals the strong cloud longwave and shortwave radiative forcing with opposite signs in that area, the greenhouse effect associated with more upper clouds can increase SEI through more warming at the slab ocean and land surface.

As for the lower NEI in the Southern Hemisphere, which results from the reduced NEI over the southern tropics (the Southern Ocean) in the MJO (MP-LEO2) runs, the reflection of more shortwave radiation by clouds is a dominant player (Figures 22c–22e). In particular, the enhanced shortwave reflection in the MP-LEO2 run is associated with larger low-cloud fraction via the retuning of the cloud microphysics parameters (not shown), which captures an observational aspect. The link between this tendency and the improved representation of the ITCZ is common to CMIP5 models (Hwang & Frierson, 2013). Meanwhile, there is a caveat to this improvement in the MP-LEO2 run: the formation of low clouds may not follow the observation in the MP-LEO2 run, because of poor representation of supercooled liquid water in the present microphysics scheme. Thus, it is worth testing a new microphysics scheme that has resolved this issue (e.g., Seiki & Roh, 2020), although it also has side effects at present, such as positive OLR bias (Noda et al., 2021).

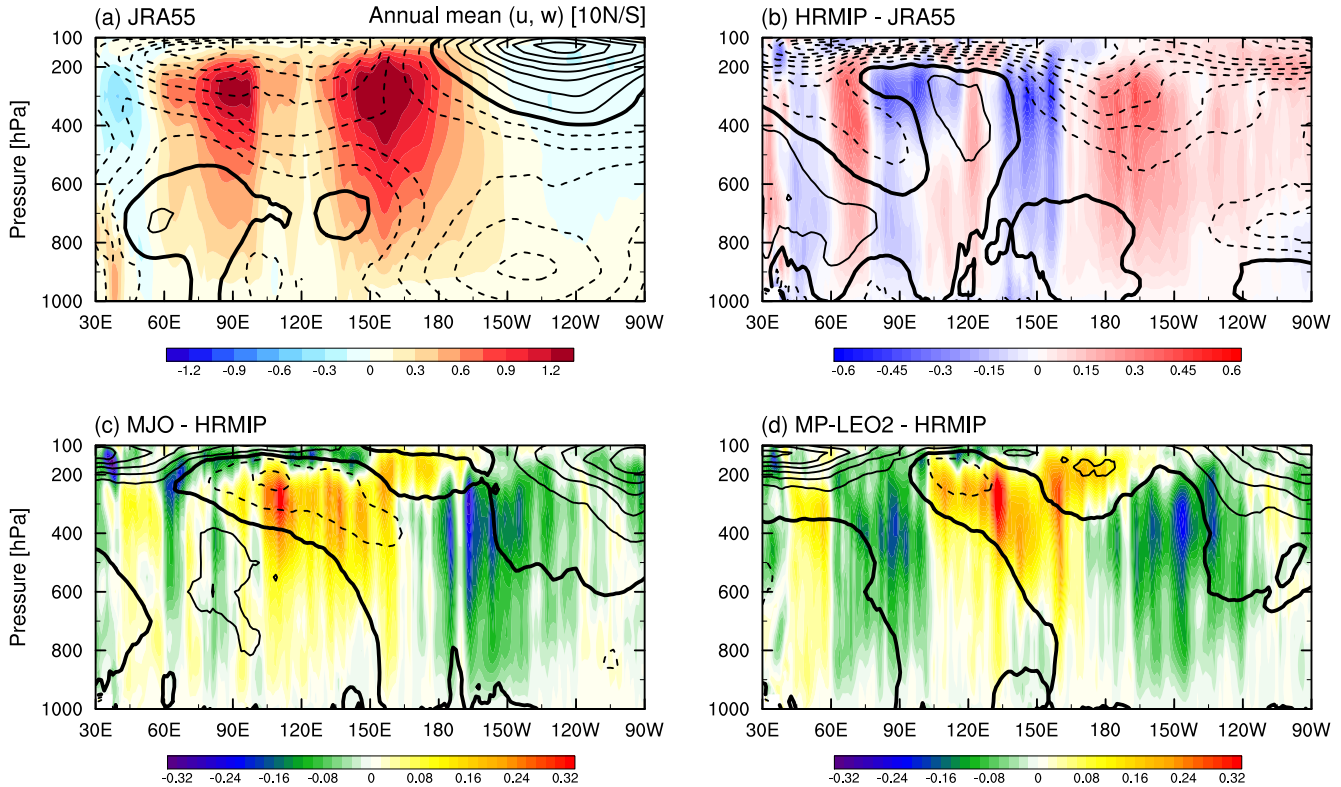

Figure 23. (a) Zonal-height section of the annual-mean equatorial (10°S–10°N) vertical winds (shading) and zonal winds (contours) for the JRA-55 reanalysis. Contour interval is 1.5 m s^{-1}, with negative (zero) contours dashed (thickened). (b) As in (a), but for their differences for the HRMIP run from JRA-55. Contour interval is 1 m s^{-1}, with negative (zero) contours dashed (thickened). (c, d) As in (b), but for their differences for the (c) MJO and (d) MP-LEO2 runs from the HRMIP run.

The above results suggest that the mitigation of the double ITCZ bias in GCRMs is related to the mean radiation distributions associated with the representation of both upper and low clouds (cf., Figures 6 and 12), depending on the difference and/or retuning in cloud microphysics schemes. However, this climatological energetic view can be incomplete, as implied by the MP-LEO2-L78 run. In this experiment, less energy is transported southward than in the MP-LEO2 run (Figure 22a) because of lower NEI in the Northern Hemisphere associated with increased OLR (Figures 12a and 12d); this situation corresponds not to a double ITCZ but simply to enhanced precipitation over the South Pacific (Figure 11e). Hence, beyond a focus on the north-south contrast, it is necessary to consider other aspects in order to better understand the ITCZ structure, which was also pointed out by Kawai et al. (2021). For example, several studies have claimed that local convection characteristics can modulate the extent of the double ITCZ (e.g., Bacmeister et al., 2006; Hirota et al., 2011), so the modified moisture–convection relationship (see Sections 3.1 and 4) is another possible explanation for the modified ITCZ characteristics.

6.2. Relationship Between the MJO and Mean Walker Circulation

Recently, Suematsu et al. (2022) showed that the spontaneous MJO realization in a 30-year climate simulation on NICAM tends to be disturbed by the stronger circulation of the western background Walker cell in 30°E−180°. This suggests an important relationship between the mean atmospheric circulation and MJO activities. Following this notion, we interpret the improvement of the MJO representation in the MP-LEO2 run in terms of a change in the annual-mean Walker circulation.

Figures 23a and 23b show the annual-mean zonal/vertical winds averaged in 10°S–10°N for the JRA-55 reanalysis and their differences from JRA-55 in the HRMIP run, respectively. Compared to the reanalysis, the upward branch simulated in the HRMIP run is elongated more eastward to the Pacific (180°–120°W), and is enhanced in

the western Indian Ocean (60°–75°E). Related to this, 200–100-hPa easterlies are strengthened in the whole region of the warm pool (30°E−180°) corresponding to the western Walker cell area. This background is unfavorable for MJO realization (cf., Figures 15b and 17b).

In Figures 23c and 23d, the differences in the annual-mean Walker circulation between the HRMIP and MJO or MP-LEO2 runs are presented. The bias of the eastward elongation of the upward branch in the HRMIP run is reduced in both the MJO and MP-LEO2 runs, as expected from the precipitation distributions (Figures 5c, 9d, and 9f). Meanwhile, vertical motions and upper-level zonal winds in 60°E−180° are modified differently between the MJO and MP-LEO2 runs. In the MP-LEO2 run, an area of mainly enhanced upward motions is narrower than in the MJO run (120°–165°E vs. 105°–165°E); a zonal peak of upward motions is displaced farther eastward; and upward motions in the Indian Ocean are suppressed more. As a result, the MP-LEO2 run can counteract the upper-level easterly bias over the warm pool found in the HRMIP run, except around the Maritime Continent, by producing more anomalous upper-level westerlies in 60°–90°E and 150°E−180° than in the MJO run. This result supports the findings of Suematsu et al. (2022), in that the overall suppressed western Walker cell induced by the MP-LEO2-run setting occurs in conjunction with the robust MJO reproduction away from initial value problems (cf., Figure 15d).

7. Summary and Concluding Remarks

Toward the achievement of a reliable k-scale climate simulation, our final goal is to obtain a model setting of k-scale NICAM that can attain the realistic seamless representation of equilibrium states and variabilities over a wide range of spatio-temporal scales. Considering that there are some systematic errors irrespective of horizontal resolutions of O(1–10)-km scale, we aim to mitigate the known biases of both the climatological mean states and weather disturbances in 14-km mesh simulations. For this purpose, using a series of 1-year sensitivity experiments, we have reconsidered the modeled moist processes (e.g., cloud microphysics, turbulent diffusion) and vertical resolutions, and comprehensively examined their impacts on the moisture–convection relationship and simulated fields. In improving the model, we refer to the two representative settings in the present NICAM: the HighResMIP-tuned (Kodama et al., 2021) and MJO-tuned settings (Suematsu et al., 2021), which prioritize the radiation balance in *climate* simulations and the realistic MJO reproduction in *S2S*-scale simulations, respectively.

The comparisons of the simulations with the HighResMIP-tuned (HRMIP run) and MJO-tuned settings (MJO run) suggest that the moisture–convection relationship largely differs between them; in the MJO run, deep convection is less prone to being triggered, and mid-tropospheric moistening after deep convection triggering is more efficient (Figure 3b). This modification is induced by the increased static stability around the PBL, melting layer, and 300 hPa due to the changes in heating profiles via tuning that slows the falling speeds of rain and snow (Figures 3c and 4b). Related to these differences, the HRMIP and MJO runs have both good points and severe biases in the annual-mean states and disturbances. Whereas the mean precipitation distributions are better in the MJO run in terms of the non-prominent double ITCZ bias (Figure 5), the bias of the mean radiation balance is greatly suppressed in the HRMIP run (Figure 6). As for the representation of tropical disturbances, the gravity-wave and rotational moisture-coupled modes are greatly preferred in the HRMIP and MJO runs, respectively (Figure 7).

To incorporate good performances of the HRMIP and MJO runs, we strive to revise the moisture–convection relationship to represent an intermediate between those two runs. In this strategy, we have updated the model in three ways: (a) retuning the cloud microphysics parameters; (b) implementing turbulent diffusion by Leonard and cross terms; and (c) enhancing the vertical resolution. For the first point, we set the falling speeds of rain and snow to be intermediate between those in the HRMIP and MJO runs (Figure 8a), and we newly introduce the effect of cloud ice falling. This revision attains a moisture–convection relationship that is similar to that in the MJO run and is reasonably tuned in amplitude (Figure 8e), while restraining OLR from being too low. The second update can diffuse water vapor, cloud water, and cloud ice effectively in the vicinity of deep convective cores (Figure 9a), which promotes mid-tropospheric moisture detrainment and suppresses excessively strong precipitation (Figures 9b–9f). Lastly, the increased vertical resolutions slightly weaken the PBL-to-mid-level moistening that is reinforced by the first and second updates, and they slightly improve the timing of convection triggering, probably because of higher resolution in the layers near the surface (cf., Figure 21). These three

revisions alter convective organization characteristics in a manner consistent with the modification of the moisture–convection relationship; they succeed in representing organized rainfall systems that are larger in scale than those in the HRMIP run (Figure 10).

The model updates have succeeded in reducing various kinds of biases recognized in the NICAM HighResMIP climate simulation. The double ITCZ structure almost disappears, and the seasonal migration of precipitation over the tropical Pacific is also represented more realistically (Figure 11). Although the model updates without the vertical resolution enhancement lead to a bias of the annual-mean radiation fields that is intermediate between the HRMIP and MJO runs (Figures 12a–12c and 12f–12h), they can reduce the high temperature bias in the tropical upper troposphere and the poleward shift and/or stronger amplitude of the mid-latitude tropospheric westerly jets (Figure 13). In addition, an increase in the number of vertical layers drastically improves the representation of the annual-mean OLR fields and zonal mean temperature and circulations (Figures 12d, 13g, and 13h), mainly because of the better simulation of upper clouds (Seiki et al., 2015). Hence, both the physics updates and higher vertical resolution enable us to obtain the best performance in representing the overall climatological statistics.

This new model configuration also achieves the more realistic simulation of weather disturbances. Both the gravity-wave and rotational moisture-coupled modes are simulated in a good balance (Figure 14), and the quasi-periodic MJO propagation is spontaneously reproduced in boreal winter (Figure 15). The penetration of the Asian summer monsoon into the western Pacific is better represented (Figure 16), and the northward propagation of BSISO events is realistically simulated (Figure 17). The improvement of these boreal-summer phenomena reasonably reduces the bias of few TCs that are generated and pass over the western Pacific (Figure 18). Furthermore, despite a few impacts of the model updates on the TC intensity, the pressure–wind relationship becomes slightly closer to the observation, and more intense TCs with maximum 10-m wind speeds exceeding 45 m s^{-1} can be generated (Figure 19). Meanwhile, the representation of the diurnal cycle of tropical precipitation does not depend significantly on the model settings, although the revised moist physics and vertical resolution enhancement slightly improve convection triggering over land (Figures 20 and 21).

This study is based on the premise of simulations at 14-km resolution, which is too coarse to appropriately represent low clouds, the inner core structure of TCs, and sub-daily-scale destabilization. Thus, it is inevitable that there remain large biases irrespective of model physics, especially in the climatological mean OSR fields, TC intensity, and precipitation diurnal cycle. Considering the spatial scales of these phenomena, the latter two can be represented much more realistically at k-scale resolutions without additional extensive tuning (e.g., see Appendix A, Sato et al. (2009), and Love et al. (2011) for precipitation diurnal cycle). Also, the ratio of precipitation over ocean versus land becomes more realistic in k-scale simulations; a bias of overestimation (underestimation) of precipitation over ocean (land) at 14-km resolution is reduced at 3.5-km resolution (Table A1 in Appendix A). Nevertheless, higher resolutions alone probably do not resolve all the biases, and fundamentally, it is still not feasible to perform global climate simulations that can resolve turbulent mixing. To address this issue, we must consider how the interaction between the PBL and free troposphere and free-tropospheric subgrid-scale turbulent diffusion is modeled in k-scale simulations.

In addition, while the model setting appropriate for 14-km resolution would also maintain good performance in k-scale simulations in terms of the moisture–convection relationship (as inferred from resolution-independent features shown in Figure 1), there is the possibility of another resolution dependency with globally uniform impacts such as the dependency on the upper-cloud representation (e.g., Miyakawa & Miura, 2019). In fact, to optimize climatological mean OLR fields in our ongoing 3.5-km mesh NICAM climate simulation, we have made very minor changes to the model setting established in this study while maintaining desirable points of convection characteristics shown in Section 4 (Takasuka et al., 2023). In that sense, how we should systematically deal with the resolution dependency in GCRMs remains a challenging question in future model improvement.

Finally, we discuss some expectations in a k-scale climate simulation with an ocean-coupled version of NICAM (NICOCO; Miyakawa et al., 2017) as a necessary last step to complete our work. The reproducibility of weather such as monsoons, MJO, and TCs, which is already guaranteed to some extent in this work, can be further improved by ocean–atmosphere coupling (e.g., DeMott et al., 2019; Li & Sriver, 2018; Song & Zhou, 2014).

Meanwhile, as for the climatological statistics, the underestimation of OSR fields at the TOA is expected to cause an unrealistic SST warming trend due to more incoming solar energy. Although this trend appears not to be serious for a 14-km-grid atmosphere/0.25°-grid ocean NICOCO simulation that adopts the model setting established in this work (Takano et al., 2022), we need to work on reducing this error related to low-cloud representation.

Appendix A: Precipitation Diurnal Cycle and Land-Ocean Contrast of Precipitation in a K-Scale Simulation

As an example of a drastically good impact of k-scale simulations, we focus on the resolution dependency on the precipitation diurnal cycle and land-ocean contrast of precipitation. We conducted a 1-year simulation at 3.5-km resolution, following the same protocol as in this study. The model setting used for the 3.5-km mesh simulation is slightly different from the model physics for the MP-LEO2-L78 run; the value of K_f is set to 1.0, and the autoconversion rate from cloud ice to snow is increased. The latter is required for achieving the better radiation balance at 3.5-km resolution.

Figure A1 compares the composite diurnal cycle of the offshore migration of precipitation systems around the western coastal region of Sumatra Island between 14-km (MP-LEO2-L78 run; Figure A1a) and 3.5-km simulations (Figure A1b). In the 3.5-km mesh run, the delayed convection triggering bias over coastal land is drastically mitigated, and more organization of precipitation during its offshore migration are simulated well. In addition, inland-propagating precipitation systems in 15:00–24:00 LT are simulated robustly. These characteristics are very close to the observed behavior (Figure 21a), which suggests that the realistic representation of the precipitation diurnal cycle certainly requires k-scale atmospheric modeling.

Consistent with this improvement for the diurnal cycle over both ocean and land, the land-ocean contrast of the amount of precipitation is simulated more realistically at 3.5-km resolution. Table A1 compares the mean amount of precipitation over ocean and land between the 14-km and 3.5-km mesh simulations and observation. When increasing resolution, the overestimation and underestimation of precipitation over ocean and land is mitigated, respectively, although the ratio of land-to-oceanic precipitation is still much lower than the observation.

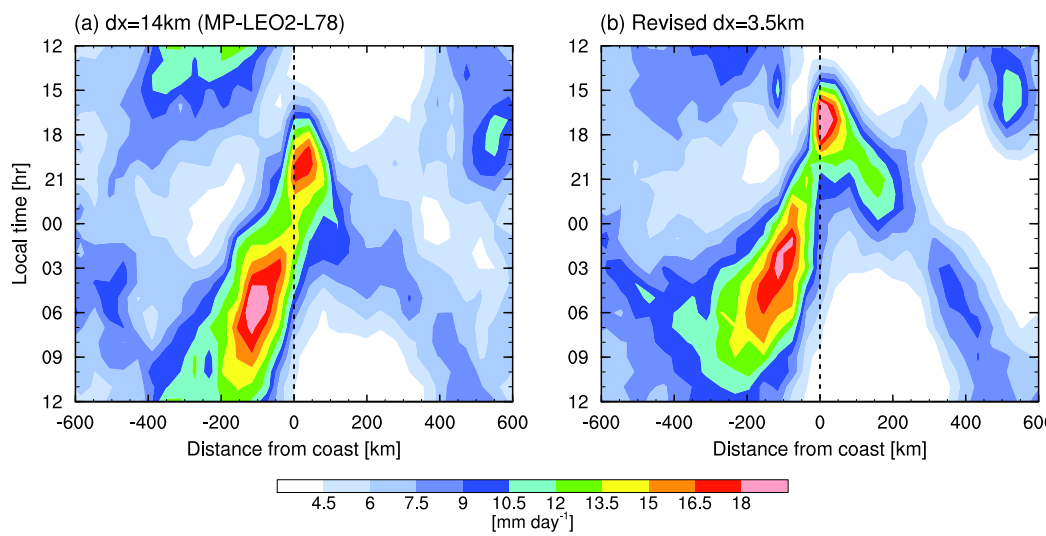

Figure A1. (a) The same as Figure 21e. (b) The same as (a), but for the 3.5-km mesh simulation under the new setting based on this study.

Table A1
Mean Amount of Precipitation Over Ocean and Land and Its Ratio (Land to Ocean) for 1-Year NICAM Simulations at 14- and 3.5-km Resolutions and Observation (TRMM-3G68 Climatology)

Resolution	Ocean	Land	Ratio (Land/Ocean)
14 km	4.84	2.99	0.619
3.5 km	4.70	3.10	0.660
TRMM-3G68	3.59	3.70	1.03

Data Availability Statement

The JRA-55 (Japanese 55-year Reanalysis Project) data are available at https://jra.kishou.go.jp/JRA-55/index_en.html#usage. The CERES-EBAF can be downloaded from https://ceres.larc.nasa.gov/data/. The GPCP product can be obtained from https://rda.ucar.edu/datasets/ds728.7/ if registered. The TRMM-3B42 data are provided by https://disc2.gesdisc.eosdis.nasa.gov/data/TRMM_L3/TRMM_3B42.7/. The hourly climatology of the TRMM-3G68 product is available at https://www.sci.hokudai.ac.jp/~minobe/data_by_minobe/TRMM3G68_diurnal_clim/. The IBTrACS data can be obtained from https://www.ncei.noaa.gov/products/international-best-track-archive. The NICAM simulation data used in this work are available at https://figshare.com/articles/dataset/Data_for_Takasuka_etal_2023_JAMES/22214608. All figures are created by NCAR Command Language version 6.6.2, which can be installed via https://www.ncl.ucar.edu/current_release.shtml.

Acknowledgments
The authors are grateful to Dr. Tobias Becker and two anonymous reviewers for their constructive and helpful comments, which greatly improved the original version of the manuscript. The analysis for Figure 10 is based on the input from Dr. Becker. D. Takasuka, C. Kodama, Y. Yamada, and M. Nakano were supported by JSPS KAKENHI Grants 20H05728. T. Suematsu was supported by JSPS KAKENHI Grants 21K13991 and 20H05730. H. Miura was supported by JSPS KAKENHI Grants 20B202 and 20H05729. D. Takasuka, C. Kodama, Y. Yamada, M. Nakano, T. Miyakawa, and R. Masunaga were supported by the Ministry of Education, Culture, Sports, Science and Technology (MEXT) as "Program for promoting researches on the supercomputer Fugaku" JPMXP1020200305, Large Ensemble Atmospheric and Environmental Prediction for Disaster Prevention and Mitigation. Most of the sensitivity experiments in this study were performed on the supercomputer Fugaku (proposal numbers hp210085, hp210166, hp220132), and some preliminary experiments were performed on the Earth Simulator at the Japan Agency for Marine-Earth Science and Technology (JAMSTEC), which was supported by MEXT program for the advanced studies of climate change projection (SENTAN) Grant JPMXD0722680395.

References

Adam, O., Schneider, T., Brient, F., & Bischoff, T. (2016). Relation of the double-ITCZ bias to the atmospheric energy budget in climate models. *Geophysical Research Letters*, *43*(14), 7670–7677. https://doi.org/10.1002/2016gl069465

Adames, Á. F., Kim, D., Clark, S. K., Ming, Y., & Inoue, K. (2019). Scale analysis of moist thermodynamics in a simple model and the relationship between moisture modes and gravity waves. *Journal of the Atmospheric Sciences*, *76*(12), 3863–3881. https://doi.org/10.1175/jas-d-19-0121.1

Adler, R. F., Huffman, G. J., Chang, A., Ferraro, R., Xie, P.-P., Janowiak, J., et al. (2003). The version-2 global precipitation climatology project (GPCP) monthly precipitation analysis (1979–present). *Journal of Hydrometeorology*, *4*(6), 1147–1167. https://doi.org/10.1175/1525-7541(2003)004<1147:tvgpcp>2.0.co;2

Argüeso, D., Romero, R., & Homar, V. (2020). Precipitation features of the maritime continent in parameterized and explicit convection models. *Journal of Climate*, *33*(6), 2449–2466. https://doi.org/10.1175/jcli-d-19-0416.1

Bacmeister, J. T., Suarez, M. J., & Robertson, F. R. (2006). Rain reevaporation, boundary layer–convection interactions, and pacific rainfall patterns in an AGCM. *Journal of the Atmospheric Sciences*, *63*(12), 3383–3403. https://doi.org/10.1175/jas3791.1

Bischoff, T., & Schneider, T. (2016). The equatorial energy balance, ITCZ position, and double-ITCZ bifurcations. *Journal of Climate*, *29*(8), 2997–3013. https://doi.org/10.1175/jcli-d-15-0328.1

Bony, S., Stevens, B., Frierson, D. M. W., Jakob, C., Kageyama, M., Pincus, R., et al. (2015). Clouds, circulation and climate sensitivity. *Nature Geoscience*, *8*(4), 261–268. https://doi.org/10.1038/ngeo2398

Chen, Y.-W., Satoh, M., Kodama, C., Noda, A. T., & Yamada, Y. (2022). Projection of high clouds and the link to ice hydrometeors: An approach using long-term global cloud system–resolving simulations. *Journal of Climate*, *35*(11), 3495–3514. https://doi.org/10.1175/jcli-d-21-0150.1

DeMott, C. A., Klingaman, N. P., Tseng, W.-L., Burt, M. A., Gao, Y., & Randall, D. A. (2019). The convection connection: How ocean feedbacks affect tropical mean moisture and MJO propagation. *Journal of Geophysical Research: Atmospheres*, *124*(22), 11910–11931. https://doi.org/10.1029/2019jd031015

Fairall, C. W., Bradley, E. F., Hare, J., Grachev, A. A., & Edson, J. B. (2003). Bulk parameterization of air–sea fluxes: Updates and verification for the COARE algorithm. *Journal of Climate*, *16*(4), 571–591. https://doi.org/10.1175/1520-0442(2003)016<0571:bpoasf>2.0.co;2

Germano, M. (1986). A proposal for a redefinition of the turbulent stresses in the filtered Navier–Stokes equations. *The Physics of Fluids*, *29*(7), 2323–2324. https://doi.org/10.1063/1.865568

Gunn, R., & Kinzer, G. D. (1949). The terminal velocity of fall for water droplets in stagnant air. *Journal of the Atmospheric Sciences*, *6*(4), 243–248. https://doi.org/10.1175/1520-0469(1949)006<0243:ttvoff>2.0.co;2

Hannah, W. M., & Maloney, E. D. (2011). The role of moisture-convection feedbacks in simulating the Madden-Julian oscillation. *Journal of Climate*, *24*(11), 2754–2770. https://doi.org/10.1175/2011JCLI3803.1

Hannah, W. M., & Maloney, E. D. (2014). The moist static energy budget in NCAR CAM5 hindcasts during DYNAMO. *Journal of Advances in Modeling Earth Systems*, *6*(2), 420–440. https://doi.org/10.1002/2013MS000272

Hirons, L., Inness, P., Vitart, F., & Bechtold, P. (2013). Understanding advances in the simulation of intraseasonal variability in the ECMWF model. Part II: The application of process-based diagnostics. *Quarterly Journal of the Royal Meteorological Society*, *139*(675), 1427–1444. https://doi.org/10.1002/qj.2059

Hirota, N., Takayabu, Y. N., Watanabe, M., & Kimoto, M. (2011). Precipitation reproducibility over tropical oceans and its relationship to the double ITCZ problem in CMIP3 and MIROC5 climate models. *Journal of Climate*, *24*(18), 4859–4873. https://doi.org/10.1175/2011jcli4156.1

Hohenegger, C., Kornblueh, L., Klocke, D., Becker, T., Cioni, G., Engels, J. F., et al. (2020). Climate statistics in global simulations of the atmosphere, from 80 to 2.5 km grid spacing. *Journal of the Meteorological Society of Japan. Ser. II*, *98*(1), 73–91. https://doi.org/10.2151/jmsj.2020-005

Holloway, C. E., Woolnough, S. J., & Lister, G. M. S. (2013). The effects of explicit versus parameterized convection on the MJO in a large-domain high-resolution tropical case study. Part I: Characterization of large-scale organization and propagation. *Journal of the Atmospheric Sciences*, *70*(5), 1342–1369. https://doi.org/10.1175/JAS-D-12-0227.1

Houze, J. R. A. (1993). *Cloud dynamics* (1st ed.). Academic Press.

Houze, J. R. A., Geotis, S. G., Marks, F. D., Jr., & West, A. K. (1981). Winter monsoon convection in the vicinity of north Borneo. Part I: Structure and time variation of the clouds and precipitation. *Monthly Weather Review*, *109*(8), 1595–1614. https://doi.org/10.1175/1520-0493(1981)109<1595:wmcitv>2.0.co;2

Huang, H., & Chen, F. (2019). Precipitation microphysics of tropical cyclones over the western North Pacific based on GPM DPR observations: A preliminary analysis. *Journal of Geophysical Research: Atmospheres*, *124*(6), 3124–3142. https://doi.org/10.1029/2018jd029454

Huffman, G. J., Adler, R. F., Morrissey, M. M., Bolvin, D. T., Curtis, S., Joyce, R., et al. (2001). Global precipitation at one-degree daily resolution from multisatellite observations. *Journal of Hydrometeorology*, *2*(1), 36–50. https://doi.org/10.1175/1525-7541(2001)002<0036:gpaodd>2.0.co;2

Huffman, G. J., Bolvin, D. T., Nelkin, E. J., Wolff, D. B., Adler, R. F., Gu, G., et al. (2007). The TRMM multisatellite precipitation analysis (TMPA): Quasi-global, multiyear, combined-sensor precipitation estimates at fine scales. *Journal of Hydrometeorology*, *8*(1), 38–55. https://doi.org/10.1175/JHM560.1

Huffman, G. J., Stocker, E., Bolvin, D., Nelkin, E., & Adler, R. (2012). *TRMM version 7 3B42 and 3B43 data sets* (Technical Report). National Aeronautics and Space Administration, Goddard Space Flight Center.

Hwang, Y.-T., & Frierson, D. M. (2013). Link between the double-Intertropical Convergence Zone problem and cloud biases over the Southern Ocean. *Proceedings of the National Academy of Sciences*, *110*(13), 4935–4940. https://doi.org/10.1073/pnas.1213302110

Ichikawa, H., & Yasunari, T. (2006). Time–space characteristics of diurnal rainfall over Borneo and surrounding oceans as observed by TRMM-PR. *Journal of Climate*, *19*(7), 1238–1260. https://doi.org/10.1175/jcli3714.1

Kato, S., Rose, F. G., Rutan, D. A., Thorsen, T. J., Loeb, N. G., Doelling, D. R., et al. (2018). Surface irradiances of edition 4.0 clouds and the earth's radiant energy system (CERES) energy balanced and filled (EBAF) data product. *Journal of Climate*, *31*(11), 4501–4527. https://doi.org/10.1175/jcli-d-17-0523.1

Kawai, H., Koshiro, T., & Yukimoto, S. (2021). Relationship between shortwave radiation bias over the Southern Ocean and the double-intertropical convergence zone problem in MRI-ESM2. *Atmospheric Science Letters*, *22*(12), e1064. https://doi.org/10.1002/asl.1064

Kennedy, J., Titchner, H., Rayner, N., & Roberts, M. (2017). *input4MIPs. MOHC. SSTsAndSeaice. HighResMIP. MOHC-HadISST-2-2-0-0-0, Version 20170201*. Earth System Grid Federation. https://doi.org/10.22033/ESGF/input4MIPs.1221

Kikuchi, K. (2021). The boreal summer intraseasonal oscillation (BSISO): A review. *Journal of the Meteorological Society of Japan. Ser. II*, *99*(4), 933–972. https://doi.org/10.2151/jmsj.2021-045

Kikuchi, K., Kodama, C., Nasuno, T., Nakano, M., Miura, H., Satoh, M., et al. (2017). Tropical intraseasonal oscillation simulated in an AMIP-type experiment by NICAM. *Climate Dynamics*, *48*(7–8), 2507–2528. https://doi.org/10.1007/s00382-016-3219-z

Kikuchi, K., & Wang, B. (2008). Diurnal precipitation regimes in the global tropics. *Journal of Climate*, *21*(11), 2680–2696. https://doi.org/10.1175/2007jcli2051.1

Kiladis, G. N., Wheeler, M. C., Haertel, P. T., Straub, K. H., & Roundy, P. E. (2009). Convectively coupled equatorial waves. *Reviews of Geophysics*, *47*(2), RG2003. https://doi.org/10.1029/2008RG000266

Kim, D., Sobel, A. H., Maloney, E. D., Frierson, D. M., & Kang, I.-S. (2011). A systematic relationship between intraseasonal variability and mean state bias in AGCM simulations. *Journal of Climate*, *24*(21), 5506–5520. https://doi.org/10.1175/2011jcli4177.1

Kim, D., Sperber, K., Stern, W., Waliser, D., Kang, I.-S., Maloney, E., et al. (2009). Application of MJO simulation diagnostics to climate models. *Journal of Climate*, *22*(23), 6413–6436. https://doi.org/10.1175/2009jcli3063.1

Kinter, J., III, Cash, B., Achuthavarier, D., Adams, J., Altshuler, E., Dirmeyer, P., et al. (2013). Revolutionizing climate modeling with Project Athena: A multi-institutional, international collaboration. *Bulletin of the American Meteorological Society*, *94*(2), 231–245. https://doi.org/10.1175/bams-d-11-00043.1

Klingaman, N., & Woolnough, S. (2014). Using a case-study approach to improve the Madden–Julian oscillation in the Hadley Centre model. *Quarterly Journal of the Royal Meteorological Society*, *140*(685), 2491–2505. https://doi.org/10.1002/qj.2314

Knapp, K. R., Ansari, S., Bain, C. L., Bourassa, M. A., Dickinson, M. J., Funk, C., et al. (2011). Globally gridded satellite observations for climate studies. *Bulletin of the American Meteorological Society*, *92*(7), 893–907. https://doi.org/10.1175/2011BAMS3039.1

Kobayashi, S., Ota, Y., Harada, Y., Ebita, A., Moriya, M., Onoda, H., et al. (2015). The JRA-55 reanalysis: General specifications and basic characteristics. *Journal of the Meteorological Society of Japan. Ser. II*, *93*(1), 5–48. https://doi.org/10.2151/jmsj.2015-001

Kodama, C., Noda, A., & Satoh, M. (2012). An assessment of the cloud signals simulated by NICAM using ISCCP, CALIPSO, and CloudSat satellite simulators. *Journal of Geophysical Research*, *117*(D12), D12210. https://doi.org/10.1029/2011jd017317

Kodama, C., Ohno, T., Seiki, T., Yashiro, H., Noda, A. T., Nakano, M., et al. (2021). The nonhydrostatic icosahedral atmospheric model for CMIP6 HighResMIP simulations (NICAM16-s): Experimental design, model description, and impacts of model updates. *Geoscientific Model Development*, *14*(2), 795–820. https://doi.org/10.5194/gmd-14-795-2021

Kodama, C., Yamada, Y., Noda, A. T., Kikuchi, K., Kajikawa, Y., Nasuno, T., et al. (2015). A 20-year climatology of a NICAM AMIP-type simulation. *Journal of the Meteorological Society of Japan. Ser. II*, *93*(4), 393–424. https://doi.org/10.2151/jmsj.2015-024

Leonard, A. (1975). Energy cascade in large-eddy simulations of turbulent fluid flows. In *Advances in geophysics* (Vol. 18, pp. 237–248). Elsevier.

Li, H., & Sriver, R. L. (2018). Tropical cyclone activity in the high-resolution community earth system model and the impact of ocean coupling. *Journal of Advances in Modeling Earth Systems*, *10*(1), 165–186. https://doi.org/10.1002/2017ms001199

Liebmann, B., Hendon, H. H., & Glick, J. D. (1994). The relationship between tropical cyclones of the western Pacific and Indian Oceans and the Madden-Julian oscillation. *Journal of the Meteorological Society of Japan. Ser. II*, *72*(3), 401–412. https://doi.org/10.2151/jmsj1965.72.3_401

Liebmann, B., & Smith, C. (1996). Description of a complete (interpolated) outgoing longwave radiation dataset. *Bulletin of the American Meteorological Society*, *77*, 1275–1277.

Ling, J., Zhang, C., Wang, S., & Li, C. (2017). A new interpretation of the ability of global models to simulate the MJO. *Geophysical Research Letters*, *44*(11), 5798–5806. https://doi.org/10.1002/2017GL073891

Ling, J., Zhao, Y., & Chen, G. (2019). Barrier effect on MJO propagation by the Maritime Continent in the MJO Task Force/GeWEX atmospheric system study models. *Journal of Climate*, *32*(17), 5529–5547. https://doi.org/10.1175/JCLI-D-18-0870.1

Loeb, N. G., Doelling, D. R., Wang, H., Su, W., Nguyen, C., Corbett, J. G., et al. (2018). Clouds and the earth's radiant energy system (CERES) energy balanced and filled (EBAF) top-of-atmosphere (TOA) edition-4.0 data product. *Journal of Climate*, *31*(2), 895–918. https://doi.org/10.1175/jcli-d-17-0208.1

Louis, J.-F. (1979). A parametric model of vertical eddy fluxes in the atmosphere. *Boundary-Layer Meteorology*, *17*(2), 187–202. https://doi.org/10.1007/BF00117978

Love, B. S., Matthews, A. J., & Lister, G. M. (2011). The diurnal cycle of precipitation over the Maritime Continent in a high-resolution atmospheric model. *Quarterly Journal of the Royal Meteorological Society*, *137*(657), 934–947. https://doi.org/10.1002/qj.809

Madden, R. A., & Julian, P. R. (1971). Detection of a 40–50 day oscillation in the zonal wind in the tropical Pacific. *Journal of the Atmospheric Sciences*, *28*(5), 702–708. https://doi.org/10.1175/1520-0469(1971)028⟨0702:DOADOI⟩2.0.CO;2

Masunaga, H., L'Ecuyer, T. S., & Kummerow, C. D. (2006). The Madden–Julian oscillation recorded in early observations from the tropical rainfall Measuring Mission (TRMM). *Journal of the Atmospheric Sciences*, *63*(11), 2777–2794. https://doi.org/10.1175/JAS3783.1

McFarlane, N. (1987). The effect of orographically excited gravity wave drag on the general circulation of the lower stratosphere and troposphere. *Journal of the Atmospheric Sciences*, *44*(14), 1775–1800. https://doi.org/10.1175/1520-0469(1987)044<1775:teooeg>2.0.co;2

Minobe, S., Park, J. H., & Virts, K. S. (2020). Diurnal cycles of precipitation and lightning in the tropics observed by TRMM3G68, GSMAP, LIS, and WWLLN. *Journal of Climate*, *33*(10), 4293–4313. https://doi.org/10.1175/jcli-d-19-0389.1

Miura, H. (2019). Difficulties in the subgrid-scale redistribution of moisture of a global cloud-resolving model. In *Current trends in the representation of physical processes in weather and climate models* (pp. 207–217). Springer.

Miura, H., Satoh, M., Nasuno, T., Noda, A. T., & Oouchi, K. (2007). A Madden-Julian oscillation event realistically simulated by a global cloud-resolving model. *Science*, *318*(5857), 1763–1765. https://doi.org/10.1126/science.1148443

Miura, H., Satoh, M., Tomita, H., Noda, A. T., Nasuno, T., & Iga, S.-I. (2007). A short-duration global cloud-resolving simulation with a realistic land and sea distribution. *Geophysical Research Letters*, *34*(2), L02804. https://doi.org/10.1029/2006GL027448

Miura, H., Suematsu, T., & Nasuno, T. (2015). An ensemble hindcast of the Madden-Julian Oscillation during the CINDY2011/DYNAMO field campaign and influence of seasonal variation of sea surface temperature. *Journal of the Meteorological Society of Japan. Ser. II*, *93A*(0), 115–137. https://doi.org/10.2151/jmsj.2015-055

Miyakawa, T., & Miura, H. (2019). Resolution dependencies of tropical convection in a global cloud/cloud-system resolving model. *Journal of the Meteorological Society of Japan. Ser. II*, *97*(3), 745–756. https://doi.org/10.2151/jmsj.2019-034

Miyakawa, T., Satoh, M., Miura, H., Tomita, H., Yashiro, H., Noda, A. T., et al. (2014). Madden–Julian Oscillation prediction skill of a new-generation global model demonstrated using a supercomputer. *Nature Communications*, *5*(5), 1–6. https://doi.org/10.1038/ncomms4769

Miyakawa, T., Yashiro, H., Suzuki, T., Tatebe, H., & Satoh, M. (2017). A Madden-Julian Oscillation event remotely accelerates ocean upwelling to abruptly terminate the 1997/1998 super El Niño. *Geophysical Research Letters*, *44*(18), 9489–9495. https://doi.org/10.1002/2017GL074683

Miyamoto, Y., Kajikawa, Y., Yoshida, R., Yamaura, T., Yashiro, H., & Tomita, H. (2013). Deep moist atmospheric convection in a subkilometer global simulation. *Geophysical Research Letters*, *40*(18), 4922–4926. https://doi.org/10.1002/grl.50944

Moeng, C.-H., Sullivan, P., Khairoutdinov, M., & Randall, D. (2010). A mixed scheme for subgrid-scale fluxes in cloud-resolving models. *Journal of the Atmospheric Sciences*, *67*(11), 3692–3705. https://doi.org/10.1175/2010jas3565.1

Moon, I.-J., Ginis, I., Hara, T., & Thomas, B. (2007). A physics-based parameterization of air–sea momentum flux at high wind speeds and its impact on hurricane intensity predictions. *Monthly Weather Review*, *135*(8), 2869–2878. https://doi.org/10.1175/mwr3432.1

Mori, S., Jun-Ichi, H., Tauhid, Y. I., Yamanaka, M. D., Okamoto, N., Murata, F., et al. (2004). Diurnal land–sea rainfall peak migration over Sumatera Island, Indonesian Maritime Continent, observed by TRMM satellite and intensive rawinsonde soundings. *Monthly Weather Review*, *132*(8), 2021–2039. https://doi.org/10.1175/1520-0493(2004)132<2021:dlrpmo>2.0.co;2

Nakanishi, M., & Niino, H. (2006). An improved Mellor–Yamada level-3 model: Its numerical stability and application to a regional prediction of advection fog. *Boundary-Layer Meteorology*, *119*(2), 397–407. https://doi.org/10.1007/s10546-005-9030-8

Nakano, M., & Kikuchi, K. (2019). Seasonality of intraseasonal variability in global climate models. *Geophysical Research Letters*, *46*(8), 4441–4449. https://doi.org/10.1029/2019gl082443

Nakano, M., Sawada, M., Nasuno, T., & Satoh, M. (2015). Intraseasonal variability and tropical cyclogenesis in the western North Pacific simulated by a global nonhydrostatic atmospheric model. *Geophysical Research Letters*, *42*(2), 565–571. https://doi.org/10.1002/2014gl062479

Nakazawa, T. (1986). Intraseasonal variations of OLR in the tropics during the FGGE year. *Journal of the Meteorological Society of Japan. Ser. II*, *64*(1), 17–34. https://doi.org/10.2151/jmsj1965.64.1_17

Nasuno, T. (2021). Impacts of cloud microphysics modifications on diurnal convection and the ISO over the maritime continent: A case study of YMC-Sumatra 2017. *SOLA*, *17*, 16–23. https://doi.org/10.2151/sola.2021-003

Nasuno, T., Yamada, H., Nakano, M., Kubota, H., Sawada, M., & Yoshida, R. (2016). Global cloud-permitting simulations of Typhoon Fengshen (2008). *Geoscience Letters*, *3*(1), 1–13. https://doi.org/10.1186/s40562-016-0064-1

Noda, A., Oouchi, K., Satoh, M., & Tomita, H. (2012). Quantitative assessment of diurnal variation of tropical convection simulated by a global nonhydrostatic model without cumulus parameterization. *Journal of Climate*, *25*(14), 5119–5134. https://doi.org/10.1175/jcli-d-11-00295.1

Noda, A., Oouchi, K., Satoh, M., Tomita, H., Iga, S.-i., & Tsushima, Y. (2010). Importance of the subgrid-scale turbulent moist process: Cloud distribution in global cloud-resolving simulations. *Atmospheric Research*, *96*(2–3), 208–217. https://doi.org/10.1016/j.atmosres.2009.05.007

Noda, A., Seiki, T., Roh, W., Satoh, M., & Ohno, T. (2021). Improved representation of low-level mixed-phase clouds in a global cloud-system-resolving simulation. *Journal of Geophysical Research: Atmospheres*, *126*(17), e2021JD035223. https://doi.org/10.1029/2021jd035223

Noda, A., Seiki, T., Satoh, M., & Yamada, Y. (2016). High cloud size dependency in the applicability of the fixed anvil temperature hypothesis using global nonhydrostatic simulations. *Geophysical Research Letters*, *43*(5), 2307–2314. https://doi.org/10.1002/2016gl067742

Ohno, T., Noda, A. T., & Satoh, M. (2020). Impacts of sub-grid ice cloud physics in a turbulence scheme on high clouds and their response to global warming. *Journal of the Meteorological Society of Japan. Ser. II*, *98*(5), 1069–1081. https://doi.org/10.2151/jmsj.2020-054

Ohno, T., & Satoh, M. (2015). On the warm core of a tropical cyclone formed near the tropopause. *Journal of the Atmospheric Sciences*, *72*(2), 551–571. https://doi.org/10.1175/jas-d-14-0078.1

Ohno, T., & Satoh, M. (2018). Roles of cloud microphysics on cloud responses to sea surface temperatures in radiative-convective equilibrium experiments using a high-resolution global nonhydrostatic model. *Journal of Advances in Modeling Earth Systems*, *10*(8), 1970–1989. https://doi.org/10.1029/2018ms001386

Ohno, T., Satoh, M., & Noda, A. T. (2019). Fine vertical resolution radiative-convective equilibrium experiments: Roles of turbulent mixing on the high-cloud response to sea surface temperatures. *Journal of Advances in Modeling Earth Systems*, *11*(6), 1637–1654. https://doi.org/10.1029/2019ms001704

Poli, P., Hersbach, H., Dee, D. P., Berrisford, P., Simmons, A. J., Vitart, F., et al. (2016). ERA-20C: An atmospheric reanalysis of the twentieth century. *Journal of Climate*, *29*(11), 4083–4097. https://doi.org/10.1175/jcli-d-15-0556.1

Ritchie, E. A., & Holland, G. J. (1997). Scale interactions during the formation of Typhoon Irving. *Monthly Weather Review*, *125*(7), 1377–1396. https://doi.org/10.1175/1520-0493(1997)125<1377:sidtfo>2.0.co;2

Rogers, R., Baumgardner, D., Ethier, S., Carter, D., & Ecklund, W. (1993). Comparison of raindrop size distributions measured by radar wind profiler and by airplane. *Journal of Applied Meteorology and Climatology*, *32*(4), 694–699. https://doi.org/10.1175/1520-0450(1993)032<0694:corsdm>2.0.co;2

Roh, W., & Satoh, M. (2014). Evaluation of precipitating hydrometeor parameterizations in a single-moment bulk microphysics scheme for deep convective systems over the tropical central Pacific. *Journal of the Atmospheric Sciences*, *71*(7), 2654–2673. https://doi.org/10.1175/jas-d-13-0252.1

Roh, W., Satoh, M., & Nasuno, T. (2017). Improvement of a cloud microphysics scheme for a global nonhydrostatic model using TRMM and a satellite simulator. *Journal of the Atmospheric Sciences*, *74*(1), 167–184. https://doi.org/10.1175/jas-d-16-0027.1

Sato, T., Miura, H., Satoh, M., Takayabu, Y. N., & Wang, Y. (2009). Diurnal cycle of precipitation in the tropics simulated in a global cloud-resolving model. *Journal of Climate*, *22*(18), 4809–4826. https://doi.org/10.1175/2009jcli2890.1

Satoh, M. (2002). Conservative scheme for the compressible nonhydrostatic models with the horizontally explicit and vertically implicit time integration scheme. *Monthly Weather Review*, *130*(5), 1227–1245. https://doi.org/10.1175/1520-0493(2002)130<1227:csftcn>2.0.co;2

Satoh, M. (2003). Conservative scheme for a compressible nonhydrostatic model with moist processes. *Monthly Weather Review*, *131*(6), 1033–1050. https://doi.org/10.1175/1520-0493(2003)131<1033:csfacn>2.0.co;2

Satoh, M., Matsuno, T., Tomita, H., Miura, H., Nasuno, T., & Iga, S. (2008). Nonhydrostatic icosahedral atmospheric model (NICAM) for global cloud resolving simulations. *Journal of Computational Physics*, *227*(7), 3486–3514. https://doi.org/10.1016/j.jcp.2007.02.006

Satoh, M., Stevens, B., Judt, F., Khairoutdinov, M., Lin, S.-J., Putman, W. M., & Düben, P. (2019). Global cloud-resolving models. *Current Climate Change Reports*, *5*(3), 172–184. https://doi.org/10.1007/s40641-019-00131-0

Segura, H., Hohenegger, C., Wengel, C., & Stevens, B. (2022). Learning by doing: Seasonal and diurnal features of tropical precipitation in a global-coupled storm-resolving model. *Geophysical Research Letters*, *49*(24), e2022GL101796. https://doi.org/10.1029/2022gl101796

Seiki, T., Kodama, C., Satoh, M., Hashino, T., Hagihara, Y., & Okamoto, H. (2015). Vertical grid spacing necessary for simulating tropical cirrus clouds with a high-resolution atmospheric general circulation model. *Geophysical Research Letters*, *42*(10), 4150–4157. https://doi.org/10.1002/2015gl064282

Seiki, T., & Ohno, T. (2023). Improvements of the double-moment bulk cloud microphysics scheme in the Nonhydrostatic ICosahedral Atmospheric Model (NICAM). *Journal of the Atmospheric Sciences*, *80*(1), 111–127. https://doi.org/10.1175/jas-d-22-0049.1

Seiki, T., & Roh, W. (2020). Improvements in supercooled liquid water simulations of low-level mixed-phase clouds over the Southern Ocean using a single-column model. *Journal of the Atmospheric Sciences*, *77*(11), 3803–3819. https://doi.org/10.1175/jas-d-19-0266.1

Seiki, T., Satoh, M., Tomita, H., & Nakajima, T. (2014). Simultaneous evaluation of ice cloud microphysics and nonsphericity of the cloud optical properties using hydrometeor video sonde and radiometer sonde in situ observations. *Journal of Geophysical Research: Atmospheres*, *119*(11), 6681–6701. https://doi.org/10.1002/2013jd021086

Sekiguchi, M., & Nakajima, T. (2008). A *k*-distribution-based radiation code and its computational optimization for an atmospheric general circulation model. *Journal of Quantitative Spectroscopy and Radiative Transfer*, *109*(17–18), 2779–2793. https://doi.org/10.1016/j.jqsrt.2008.07.013

Shepherd, T. G., Polichtchouk, I., Hogan, R. J., & Simmons, A. J. (2018). *Report on Stratosphere Task Force* (Technical Report). European Centre for Medium Range Weather Forecasts.

Shibuya, R., Nakano, M., Kodama, C., Nasuno, T., Kikuchi, K., Satoh, M., et al. (2021). Prediction skill of the boreal summer intra-seasonal oscillation in global non-hydrostatic atmospheric model simulations with explicit cloud microphysics. *Journal of the Meteorological Society of Japan. Ser. II*, *99*(4), 973–992. https://doi.org/10.2151/jmsj.2021-046

Slingo, J., Bates, P., Bauer, P., Belcher, S., Palmer, T., Stephens, G., et al. (2022). Ambitious partnership needed for reliable climate prediction. *Nature Climate Change*, *12*(6), 499–503. https://doi.org/10.1038/s41558-022-01384-8

Song, F., & Zhou, T. (2014). The climatology and interannual variability of East Asian summer monsoon in CMIP5 coupled models: Does air–sea coupling improve the simulations? *Journal of Climate*, *27*(23), 8761–8777. https://doi.org/10.1175/jcli-d-14-00396.1

Stevens, B., Satoh, M., Auger, L., Biercamp, J., Bretherton, C. S., Chen, X., et al. (2019). DYAMOND: The DYnamics of the Atmospheric general circulation Modeled On Non-hydrostatic Domains. *Progress in Earth and Planetary Science*, *6*(1), 1–17. https://doi.org/10.1186/s40645-019-0304-z

Straub, K. H., & Kiladis, G. N. (2003). Interactions between the boreal summer intraseasonal oscillation and higher-frequency tropical wave activity. *Monthly Weather Review*, *131*(5), 945–960. https://doi.org/10.1175/1520-0493(2003)131⟨0945:IBTBSI⟩2.0.co;2

Suematsu, T., Kodama, C., Yamada, Y., Miura, H., Takasuka, D., & Miyakawa, T. (2021). Microphysics dependency in 3.5 km NICAM DYAMOND phase 2 experiments. In *AGU Fall Meeting Abstracts* (Vol. 2021, p. A45K–2001).

Suematsu, T., Miura, H., Kodama, C., & Takasuka, D. (2022). Deceleration of Madden–Julian oscillation speed in NICAM AMIP-type simulation associated with biases in the walker circulation strength. *Geophysical Research Letters*, *49*(11), e2022GL098628. https://doi.org/10.1029/2022gl098628

Takano, Y., Kodama, C., Nakano, M., & Miura, H. (2022). ENSO reproducibility in the high-resolution atmosphere-ocean coupled model: NICOCO (in Japanese). In *The 2022 Autumn Meeting of Meteorological Society of Japan* (Vol. 2022, p. A452).

Takasuka, D., Kodama, C., Suematsu, T., Ohno, T., Yamada, Y., Takano, Y., et al. (2023). Tackling errors toward realistic seamless representation in kilometer-scale climate simulations with NICAM. In *The 28th IUGG General Assembly Abstracts* (Vol. 2023, p. IUGG23-3863).

Takasuka, D., & Satoh, M. (2020). Dynamical roles of mixed Rossby–Gravity waves in driving convective initiation and propagation of the Madden–Julian oscillation: General views. *Journal of the Atmospheric Sciences*, *77*(12), 4211–4231. https://doi.org/10.1175/JAS-D-20-0050.1

Takasuka, D., Satoh, M., Miyakawa, T., & Miura, H. (2018). Initiation processes of the tropical intraseasonal variability simulated in an aqua-planet experiment: What is the intrinsic mechanism for MJO onset? *Journal of Advances in Modeling Earth Systems*, *10*(4), 1047–1073. https://doi.org/10.1002/2017MS001243

Takata, K., Emori, S., & Watanabe, T. (2003). Development of the minimal advanced treatments of surface interaction and runoff. *Global and Planetary Change*, *38*(1–2), 209–222. https://doi.org/10.1016/S0921-8181(03)00030-4

Takayabu, Y. N. (1994). Large-scale cloud disturbances features associated of the with cloud equatorial disturbances waves. Part I: Spectral features of the cloud disturbances. *Journal of the Meteorological Society of Japan*, *72*(3), 433–449. https://doi.org/10.2151/jmsj1965.72.3_433

Tomita, H. (2008). New microphysical schemes with five and six categories by diagnostic generation of cloud ice. *Journal of the Meteorological Society of Japan*, *86A*, 121–142. https://doi.org/10.2151/jmsj.86A.121

Tomita, H., Miura, H., Iga, S.-I., Nasuno, T., & Satoh, M. (2005). A global cloud-resolving simulation: Preliminary results from an aqua planet experiment. *Geophysical Research Letters*, *32*(8), L08805. https://doi.org/10.1029/2005gl022459

Tomita, H., & Satoh, M. (2004). A new dynamical framework of nonhydrostatic global model using the icosahedral grid. *Fluid Dynamics Research*, *34*(6), 357–400. https://doi.org/10.1016/j.fluiddyn.2004.03.003

Tomita, H., Satoh, M., & Goto, K. (2002). An optimization of the icosahedral grid modified by spring dynamics. *Journal of Computational Physics*, *183*(1), 307–331. https://doi.org/10.1006/jcph.2002.7193

Wedi, N. P., Polichtchouk, I., Dueben, P., Anantharaj, V. G., Bauer, P., Boussetta, S., et al. (2020). A baseline for global weather and climate simulations at 1 km resolution. *Journal of Advances in Modeling Earth Systems*, *12*(11), e2020MS002192. https://doi.org/10.1029/2020ms002192

Wheeler, M., & Kiladis, G. N. (1999). Convectively coupled equatorial waves: Analysis of clouds and temperature in the wavenumber–frequency domain. *Journal of the Atmospheric Sciences*, *56*(3), 374–399. https://doi.org/10.1175/1520-0469(1999)056⟨0374:CCEWAO⟩2.0.CO;2

Williams, K. D., Bodas-Salcedo, A., Déqué, M., Fermepin, S., Medeiros, B., Watanabe, M., et al. (2013). The Transpose-AMIP II experiment and its application to the understanding of Southern Ocean cloud biases in climate models. *Journal of Climate*, *26*(10), 3258–3274. https://doi.org/10.1175/jcli-d-12-00429.1

Yamada, Y., Kodama, C., Satoh, M., Nakano, M., Nasuno, T., & Sugi, M. (2019). High-resolution ensemble simulations of intense tropical cyclones and their internal variability during the El Niños of 1997 and 2015. *Geophysical Research Letters*, *46*(13), 7592–7601. https://doi.org/10.1029/2019gl082086

Yamada, Y., Satoh, M., Sugi, M., Kodama, C., Noda, A. T., Nakano, M., & Nasuno, T. (2017). Response of tropical cyclone activity and structure to global warming in a high-resolution global nonhydrostatic model. *Journal of Climate*, *30*(23), 9703–9724. https://doi.org/10.1175/jcli-d-17-0068.1

Yasunaga, K., & Mapes, B. (2012). Differences between more divergent and more rotational types of convectively coupled equatorial waves. Part II: Composite analysis based on space–time filtering. *Journal of the Atmospheric Sciences*, *69*(1), 17–34. https://doi.org/10.1175/JAS-D-11-034.1

Yasunari, T. (1979). Cloudiness fluctuations associated with the Northern Hemisphere summer monsoon. *Journal of the Meteorological Society of Japan. Ser. II*, *57*(3), 227–242. https://doi.org/10.2151/jmsj1965.57.3_227

Yokoi, S., Mori, S., Katsumata, M., Geng, B., Yasunaga, K., Syamsudin, F., et al. (2017). Diurnal cycle of precipitation observed in the western coastal area of Sumatra Island: Offshore preconditioning by gravity waves. *Monthly Weather Review*, *145*(9), 3745–3761. https://doi.org/10.1175/MWR-D-16-0468.1

Yoshida, R., & Ishikawa, H. (2013). Environmental factors contributing to tropical cyclone genesis over the western North Pacific. *Monthly Weather Review*, *141*(2), 451–467. https://doi.org/10.1175/MWR-D-11-00309.1

Yoshida, R., Kajikawa, Y., & Ishikawa, H. (2014). Impact of boreal summer intraseasonal oscillation on environment of tropical cyclone genesis over the western North Pacific. *Sola*, *10*(0), 15–18. https://doi.org/10.2151/sola.2014-004

Zhang, C., & Dong, M. (2004). Seasonality in the Madden-Julian oscillation. *Journal of Climate*, *17*(16), 3169–3180. https://doi.org/10.1175/1520-0442(2004)017⟨3169:SITMO⟩2.0.CO;2